

Wrocław University of Technology
Centre of Advanced Materials and Nanotechnology

Materials Science **Poland**

Vol. 22

No.3

2004



Oficyna Wydawnicza Politechniki Wrocławskiej

Materials Science is an interdisciplinary journal devoted to experimental and theoretical research into the synthesis, structure, properties and applications of materials.

Among the materials of interest are:

- glasses and ceramics
- sol-gel materials
- photoactive materials (including materials for nonlinear optics)
- laser materials
- photonic crystals
- semiconductor micro- and nanostructures
- piezo-, pyro- and ferroelectric materials
- high- T_c superconductors
- magnetic materials
- molecular materials (including polymers) for use in electronics and photonics
- novel solid phases
- other novel and unconventional materials

The broad spectrum of the areas of interest reflects the interdisciplinary nature of materials research. Papers covering the modelling of materials, their synthesis and characterisation, physicochemical aspects of their fabrication, properties and applications are welcome. In addition to regular papers, the journal features issues containing conference papers, as well as special issues on key topics in materials science.

Materials Science is published under the auspices of the Centre of Advanced Materials and Nanotechnology of the Wrocław University of Technology, in collaboration with the Institute of Low Temperatures and Structural Research of the Polish Academy of Sciences and the Wrocław University of Economics.

All accepted papers are placed on the Web page of the journal and are available at the address:
<http://MaterialsScience.pwr.wroc.pl>

Editor-in-Chief

Juliusz Sworakowski

Institute of Physical and Theoretical Chemistry
Wrocław University of Technology
Wybrzeże Wyspiańskiego 27
50-370 Wrocław, Poland
sworakowski@pwr.wroc.pl

Associate Editors

Wiesław Stręk

Institute of Low Temperature
and Structure Research
Polish Academy of Sciences
P.O. Box 1410
50-950 Wrocław 2, Poland
strek@int.pan.wroc.pl

Jerzy Hanuza

Department of Bioorganic Chemistry
Faculty of Industry and Economics
Wrocław University of Economics
Komandorska 118/120
53-345 Wrocław, Poland
hanuza@credit.ae.wroc.pl

Scientific Secretary

Krzysztof Maruszewski

Institute of Materials Science and Applied Mechanics
Wrocław University of Technology
Wybrzeże Wyspiańskiego 27
50-370 Wrocław, Poland
maruszewski@pwr.wroc.pl

Advisory Editorial Board

Michel A. Aegerter, Saarbrücken, Germany
Ludwig J. Balk, Wuppertal, Germany
Victor E. Borisenko, Minsk, Belarus
Mikheylo S. Brodyn, Kyiv, Ukraine
Maciej Bugajski, Warszawa, Poland
Alexander Bulinski, Ottawa, Canada
Roberto M. Faria, São Carlos, Brazil
Reimund Gerhard-Multhaupt, Potsdam, Germany
Paweł Hawrylak, Ottawa, Canada
Jorma Hölsä, Turku, Finland
Alexander A. Kaminskii, Moscow, Russia
Wacław Kasprzak, Wrocław, Poland
Andrzej Kłonkowski, Gdańsk, Poland
Seiji Kojima, Tsukuba, Japan
Shin-ya Koshihara, Tokyo, Japan
Marian Kryszewski, Łódź, Poland
Krzysztof J. Kurzydłowski, Warsaw, Poland
Jerzy M. Langer, Warsaw, Poland
Janina Legendziewicz, Wrocław, Poland
Benedykt Licznarski, Wrocław, Poland

Tadeusz Luty, Wrocław, Poland
Joop H. van der Maas, Utrecht, The Netherlands
Bolesław Mazurek, Wrocław, Poland
Gerd Meyer, Cologne, Germany
Jan Misiewicz, Wrocław, Poland
Jerzy Mroziński, Wrocław, Poland
Robert W. Munn, Manchester, U.K.
Krzysztof Nauka, Palo Alto, CA, U.S.A.
Stanislav Nešpůrek, Prague, Czech Republic
Romek Nowak, Santa Clara, CA, U.S.A.
Tetsuo Ogawa, Osaka, Japan
Renata Reisfeld, Jerusalem, Israel
Marek Samoć, Canberra, Australia
Jan Stankowski, Poznań, Poland
Leszek Stoch, Cracow, Poland
Jan van Turnhout, Delft, The Netherlands
Jacek Ulański, Łódź, Poland
Walter Wojciechowski, Wrocław, Poland
Vladislav Zolin, Moscow, Russia

The Journal is supported by the State Committee for Scientific Research

Editorial Office
Karol Langner
Łukasz Maciejewski

Printed in Poland

© Copyright by Oficyna Wydawnicza Politechniki Wrocławskiej, Wrocław 2004

Drukarnia Oficyny Wydawniczej Politechniki Wrocławskiej
Zam. nr 693/2004.

Contents

J. Stankowski, M. Krupski, R. Micnas, Remarks on the phase diagram of high-temperature superconductors: pressure dependence.....	175
A. Klukowska, U. Posset, G. Schottner, A. Jankowska-Frydel, V. Malatesta, Photochromic sol-gel derived hybrid polymer coatings: the influence of matrix properties on kinetics and photodegradation.....	187
R. Kaur, A.V. Singh, R.M. Mehra, Development of highly transparent and conducting yttrium-doped ZnO films: the role of sol-gel stabilizers.....	201
A. Bednarkiewicz, Analysis of optical transitions of Nd ³⁺ in YAG nanocrystallites.....	211
R. Pązik, D. Hreniak, W. Stręk, Synthesis and luminescence properties of nanocrystalline BaTiO ₃ :Nd ³⁺ obtained by sol-gel methods.....	219
A. Hreniak, M. Nyk, D. Hreniak, W. Stręk, L. Kepiński, J. Misiewicz, K. Maruszewski, Optical properties of Eu(III) doped nanocrystalline films of TiO ₂	227
M. Nyk, W. Stręk, J.M. Jabłoński, J. Misiewicz, Morphology, structural and absorption studies on gallium nitride powder.....	235
I. V. Korionov, A. N. Trefilova, A. N. Babushkin, W. Łojkowski, A. Opalińska, Relaxation processes in ZrO ₂ at high pressures.....	241
R. da Costa Lima, M. Silveira Pinho, M. L. Gregori, R. C. Reis Nunes, T. Ogasawara, Effect of double substituted <i>m</i> -barium hexaferrites on microwave absorption properties.....	245
A. Tomkiewicz, J. Kłak, J. Mroziński, Bimetallic complexes with macrocyclic ligands. Variation of magnetic exchange interactions in some heteronuclear thiocyanato-bridged compounds.....	253
W. Skoneczny, J. Jurusik, A. Burian, investigations of the surface morphology of Al ₂ O ₃ layers by atomic force microscopy.....	265

Remarks on the phase diagram of high-temperature superconductors: pressure dependence

JAN STANKOWSKI^{1*}, MARCIN KRUPSKI¹, ROMAN MICNAS²

¹Institute of Molecular Physics, Polish Academy of Sciences,
M. Smoluchowskiego 17, 60-179 Poznań, Poland

²Institute of Physics, Adam Mickiewicz University, Umultowska 85, 61-614 Poznań, Poland

The $T_c(x)$ dependence of high-temperature superconductors shows that superconductivity occurs above a critical concentration x_1 . For concentrations exceeding x_1 , T_c increases until an optimal concentration x_{opt} is reached and drops with further increase of x . Above x_{opt} , i.e., in the overdoped region, there exists a single T_c which can be taken as the temperature of the Cooper pair formation and, simultaneously, of their condensation (BEC) to the superconducting state. For carrier concentrations below the optimal value, $x < x_{\text{opt}}$, there are two characteristic temperatures, $T^* > T_c$. At T^* , phase incoherent local pairs (LP's) are formed and only at T_c the system undergoes the superconducting phase transition. The existence of these two characteristic temperatures, T^* and T_c , reflects various phenomena related to strong electron correlations. We review the pressure effects in the cuprate family YBCO and propose their explanation within the Hubbard model and crossover from BCS cooperative pairing to Bose–Einstein of preformed pairs. The scaling of the pressure effects above and below x_{opt} is analyzed in terms of two parameters: the transfer integral t and on-site energy U . With increasing pressure, t increases and the density of states at the Fermi level decreases. Above x_{opt} , $T_c \sim 1/2zt$ and $dT_c/dp < 0$. Below x_{opt} , however, the derivative $dT_c/dp > 0$, since $T_c \sim t^2/U$.

Key words: *high T_c cuprates; pressure effect; Cooper pairs; local pairs; phase diagram*

1. Introduction

High-temperature superconductivity (HTSC) discovered by Bednorz and Miller [1] in layered structures of copper oxides is well seen for $\text{YBa}_2\text{Cu}_3\text{O}_{6+x}$. An increase in the oxygen concentration x causes a controlled change in concentration of carriers (holes). This unique feature of YBCO allows spin and charge correlations to be monitored in the antiferromagnetic (AF) insulator state for $x < 0.5$ and in the superconduct-

*Corresponding author, e-mail: janstank@ifmpan.poznan.pl

ing (SC) state when x varies from 0.5 to 1. A general phase diagram of the cuprates [2] (Fig.1) exhibits two characteristic concentrations: x_1 , at which the superconducting phase occurs and x_{\max} , where this phase disappears. For very low concentrations of carriers (holes/electrons), the material exhibits antiferromagnetism, and spin and charge are localized. With increasing carrier concentration, pair correlations develop and almost free bosonic-like local pairs occur. The origin of a pseudogap temperature T^* is still discussed. In particular, NMR data on T_1 anomaly ascribe this temperature to a spin gap [3].

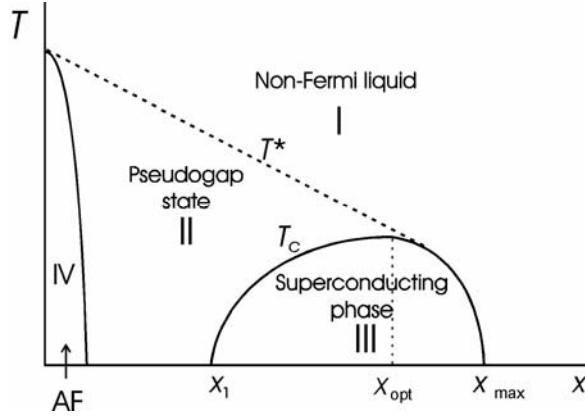


Fig. 1. Phase diagram of a high-temperature superconductor (after Ref. [2])

In this paper, we review the pressure effects in HTSC and propose their explanation within the concept of preformed pairs and BCS-BEC crossover scenario.

2. Pressure effect theory and experimental results

The pressure effect in HTSC has been analyzed in detail by Griessen [4]. The data collected for YBCO showed that the pressure coefficient dT_c/dp is large and positive for materials with T_c close to 25 K, and its absolute value tends to zero when the critical temperature attains its highest value: $T_c = 90$ K (Fig. 2). Theoretical explanation of the pressure effect explored various models, among them 3D and 2D BCS models [5, 6], the Resonating Valence Bond (RVB) approach [7] and multipolaronic models [8].

The starting point for the first two models is the equation for T_c well known in BCS theory. Under the assumption of two-dimensional transport in $\text{La}_{2-x}\text{Sr}_x\text{CuO}_{4-y}$ and YBCO, the equation has the form given by Labbé and Bok [6]:

$$k_B T_c = 1.13D \exp(-1/\lambda^{1/2}) \quad (1)$$

where k_B is the Boltzmann constant, $\lambda = N(E_F)U_{el-ph}$ is the effective parameter of the electron-phonon coupling, and D is the width of the van Hove singularity $D^2 = \gamma^2/(E_d$

$-E_p)^2 + 16\gamma^2]^{1/2}$. The parameter γ is the overlap integral of $3d_{x^2-y^2}$ and $2p_x$ orbitals. E_d and E_p are the electron site energies of $3d$ copper and $2p$ oxygen orbitals, respectively.

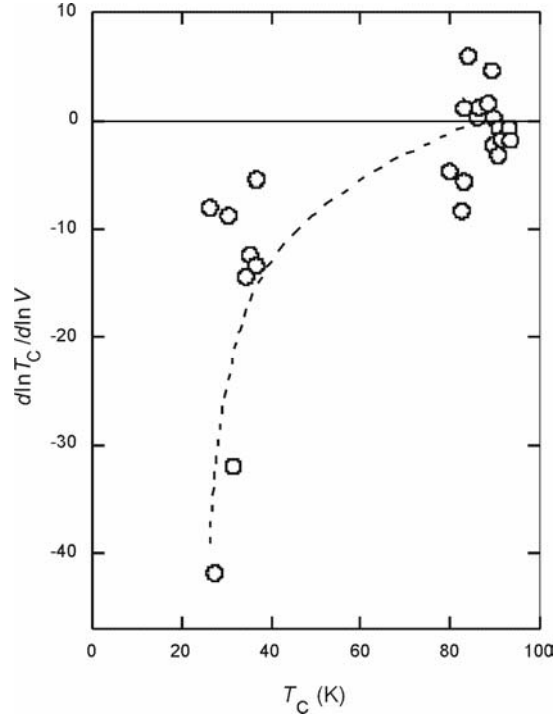


Fig. 2. $d \ln T_c / d \ln V$ versus critical temperature (after Ref. [4])

By differentiating Eq. (1), one obtains the volume dependence of T_c :

$$\frac{d \ln T_c}{d \ln V} = \frac{d \ln D}{d \ln V} + \frac{1}{2\lambda^{1/2}} \frac{d \ln \lambda}{d \ln V} \quad (2)$$

For $d \ln D / d \ln V = 4$, $d \ln \lambda / d \ln V = -3$ and $D = 0.3$ eV, Eqs. (1), (2) qualitatively describe the experimental data. The value of the parameter λ , determined from Eq. (1), strongly depends on volume, which means that electron-phonon interaction remarkably changes with increasing pressure.

In the RVB model [7], the $3d_{x^2-y^2}$ orbital of the copper ion Cu^{2+} is hybridized with the $2p_x$ oxygen orbital, forming the so-called Zhang–Rice singlet. The critical temperature has a BCS-like form:

$$k_B T_c = 1.13 \hbar \omega_0 \exp(-1/\bar{\lambda}) \quad (3)$$

where $\bar{\lambda} = (8/\pi)(t/U)\Phi(x)$. The transfer integral t and the on-site interaction U satisfy the relation $U \gg t$, and $\Phi(x)$ is some function depending exclusively on the

carrier concentration. In this model, the cutoff energy $\hbar\omega_0$ is defined by the transfer integral t . Taking $\hbar\omega_0 = 0.08$ eV and $\lambda = 0.4$ yields $T_c = 95$ K for a nearly half-filled band ($x = 1$). For heavy hole carriers, the expression for the critical temperature assumes the form:

$$T_c \approx t\delta \exp(-U\delta/t) \quad (4)$$

where $\delta = t/U$ is the admixture of the Cu^{3+} state in the main state of Cu^{2+} . The critical temperature scales as t^2/U [7]. The theory of bipolaronic superconductivity yields the largest value of the pressure coefficient dT_c/dp [8, 4].

In complex oxides, the pressure coefficient can not only take different values but it can also change the sign. Driessen et al. [9] have shown that the pressure coefficients at the onset temperature T_{co} and critical temperature T_{cf} , defined as the intersection of the tangent to linear part of the resistivity $R(T)$ curve with the T -axis, have opposite signs (Fig. 3). The pressure coefficient $dT_{co}/dp > 0$, and $dT_{cf}/dp < 0$, have opposite signs over the entire pressure range, from 0 to 170 kilobars. The change of sign in the pressure coefficient is associated with strong fluctuations above $T > T_c$. For a low concentration of the Cooper pairs, the pressure coefficient is positive, while it is negative at the critical point for high contents of the superconducting phase. This shows that the pressure expands the fluctuation region, $(T_{co} - T_{cf}) \propto p$.

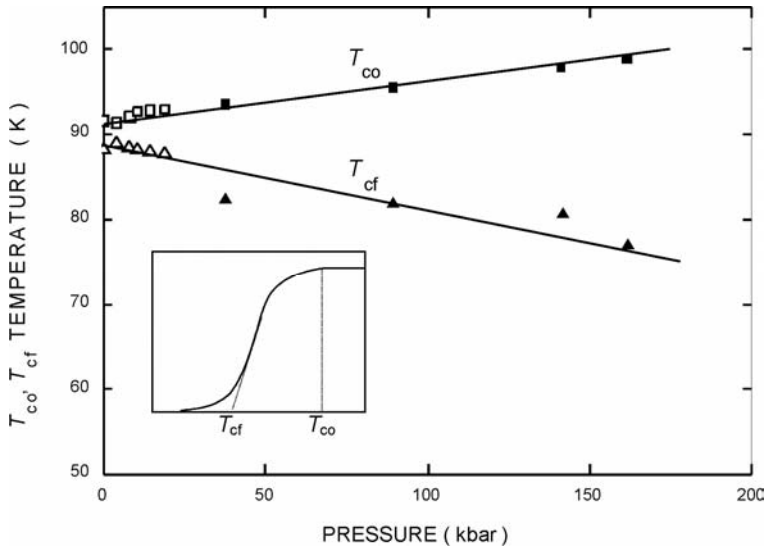


Fig. 3. Dependence of T_{co} and T_{cf} on pressure for YBCO [9].

Inset: T_{co} – critical onset temperature and zero-resistivity T_{cf} temperature

In cuprate HTSC, the empirical relation between T_c and hole concentration x (the number of holes per one Cu atom in the CuO_2 plane) is approximately described by a parabolic dependence [10, 11]. This dependence correctly describes $T_c(x)$ for such

compounds as: $\text{YBa}_2\text{Cu}_3\text{O}_{6+x}$, $\text{Y}_{1-x}\text{Ca}_x\text{Ba}_2\text{Cu}_3\text{O}_6$, $\text{La}_{2-x}\text{Sr}_x\text{CuO}_4$, $\text{La}_{2-x}\text{Sr}_x\text{CaCu}_2\text{O}_6$, as well as for $(\text{Ca}_x\text{La}_{1-x})(\text{Ba}_{1.75-x}\text{La}_{0.25+x})\text{Cu}_3\text{O}_y$ for various oxygen contents y .

Now we arrive at the fundamental question. Why and how do the phase diagram and $T_c(x)$ change when a pressure is applied? The answer was given in the paper by Sadewasser et al. [12], who present a complete description of recent investigations of the pressure dependence of T_c in $\text{YBa}_2\text{Cu}_3\text{O}_{6+x}$ in function of the concentration of oxygen defects in CuO_2 . From their data (Fig. 2 in [12]), the parabolic dependence $T_c(x)$ for various pressures may be obtained. The dependence is shown in Fig. 4 for atmospheric pressure and for $p = 8$ GPa.

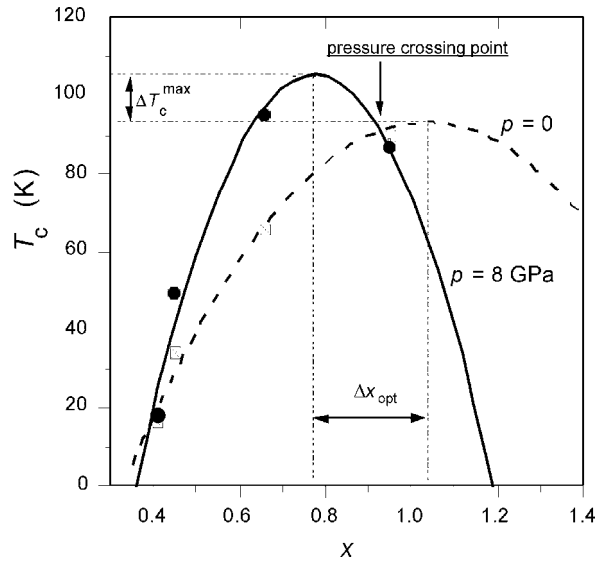


Fig. 4. T_c versus oxygen content in $\text{YBa}_2\text{Cu}_3\text{O}_{6+x}$ for $p = 0$ and under the pressure $p = 8$ GPa. The plots are a parabolic approximation to the experimental data taken from Ref. [12]

The critical temperature depends not only on carrier concentration, but also on the degree of buckling of the CuO_2 planes, on the occurrence of structural phase transformations, and on pressure induced relaxational phenomena. The latter highly interesting effect is related to the ordering of mobile oxygen defects in the lattice; an increase in pressure reduces the mobility of defects and simultaneously increases the degree of ordering of oxygen defects. This is particularly well observed in YBCO samples with reduced oxygen contents [12], where the increase of T_c with pressure, and hence the values of dT_c/dp , strongly depend on the temperature at which the pressure is varied. For example, the pressure coefficient of a sample with $x = 0.41$, subject to the effect of different pressures at low temperatures ($T < 200$ K), is $(dT_c/dp)_{LT} = +2.1$ K/GPa. However, a much larger value of dT_c/dp is obtained if the sample is subject to the same pressure at room temperature for a period sufficiently long to allow a full relaxation. A well oxygenated sample ($x = 0.95$) does not exhibit relaxation effects and its pressure coefficient $dT_c/dp = +0.24$ K/GPa.

Changes induced by hydrostatic pressure on oxygen-chain ordering were observed by Liarakapis et al. [13] in Raman spectra of $\text{YBa}_2\text{Cu}_3\text{O}_{6+x}$ single crystals ($x = 0.5$ and overdoped) in the temperature range 77–300 K. In the overdoped compounds ($x > 0.92$), pressure tends to decrease the transition temperature, reducing the disorder. This is probably connected with a structural phase transformation in the CuO_2 planes observed for $x \geq 0.95$ [14].

As was mentioned above, the dependence of T_c on carrier concentration approximately satisfies the following parabolic type relation [12]:

$$T_c = T_c^{\max} \left[1 - A(x - x_{\text{opt}})^2 \right] \quad (5)$$

where T_c^{\max} , A , x , and x_{opt} are functions of pressure. In YBCO, the carrier concentration x can be varied by changes in oxygen concentration, by cation replacements or by applying a pressure. In a simple “charge transfer model”, T_c can increase only by increasing x , with all other parameters constant. According to such a model, $dT_c/dp = 0$ at the optimal concentration $x = x_{\text{opt}}$. In reality however, the pressure coefficient is nonzero and positive, and varies from +1 to +2 K/GPa. In the modified charge transfer model [15], the total pressure derivative consists of two parts:

$$\left(\frac{dT_c}{dp} \right) = \left(\frac{\partial T_c}{\partial x} \right) \left(\frac{\partial x}{\partial p} \right) + \left(\frac{dT_c}{dp} \right)_{\text{noCT}} \quad (6)$$

The first term stands for normal charge transfer to the CuO_2 planes caused by increasing pressure, while the second term accumulates contributions from the pressure dependences of T_c^{\max} , A , and x_{opt} . However, this model is not capable of explaining all the changes observed experimentally. The experimental changes in T_c as a function of pressure and x can be explained only if one assumes that T_c^{\max} , A , and x_{opt} are quadratic functions of pressure, as demonstrated by Jover et al. [16] for the thallium compound. A very large anisotropy of the coefficient dT_c/dp as a function of axial pressure was observed in $\text{YBa}_2\text{Cu}_3\text{O}_7$. If the axial pressure was applied along the a axis, the coefficient was equal to -2.0 K/GPa. Along the b axis it was 1.9 K/GPa and along the c axis -0.3 K/GPa [17, 18]. Compression along the b axis yields a reduction in hole density, while compression along the a axis enhances this density.

3. Sign inversion of the pressure coefficient in composite PST-YBCO in the vicinity of the “pressure crossing point”

The parabolic dependencies $T_c(x, 0)$ and $T_c(x, p)$, plotted in Fig. 4, show that there is a crossing of the parabolas in the “overdoped” regime, with $p = 0$ and $p \neq 0$, suggesting a change in the sign of the pressure coefficient from positive to negative. This

result is also suggested by the theory, since for low concentrations of holes in HTSC there are strong fluctuations of the condensate, which coexist with the local pairs (LP's). When pressure is applied, the number of LP's in the Fermi sea increases, causing an increase in T_c . For large concentrations x , these fluctuations are less important and the BCS theory can be applied, predicting a negative pressure effect. The "crossing point", which gives rise to the sign change of the pressure coefficient, has been observed in samples of composite $\text{YBCO}_{1-x}\text{PST}_x$ ($\text{PST} = \text{Pb}(\text{Sc}_{0.5}\text{Ta}_{0.5})\text{O}_3$) [19]. For YBCO, a positive value of the pressure coefficient $dT_c/dp = 0.5 \text{ K/GPa}$ was obtained. The sign inversion of the pressure coefficient was also observed in composite PST-YBCO in the vicinity of "crossing" point (see Fig. 5).

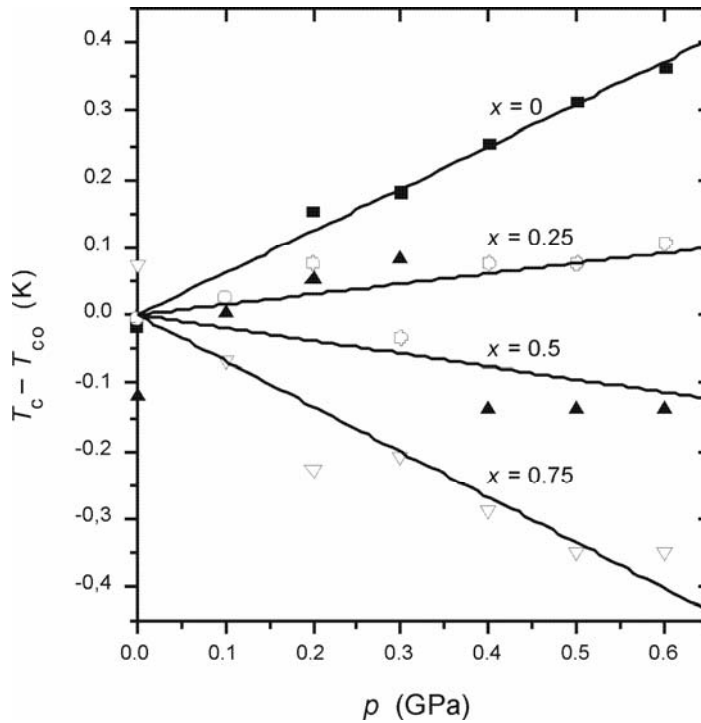


Fig. 5. Pressure dependence of the critical temperature shift, $T_c(p) - T_c(0)$, in composite $\text{YBCO}_{1-x}\text{PST}_x$ for different concentrations of PST [19]

For the dispersed superconducting phase with increasing concentrations of PST (which is a reservoir of holes), the pressure coefficient decreased and changed its sign to negative, $dT_c/dp < 0$, for high values of x . The quadratic dependence of T_{c0} on x was also confirmed. This suggests that the pressure effect depends on whether the underdoped or overdoped regime of the investigated material is considered.

The dispersion of superconducting YBCO in a PST composite leads to a change in the hole concentration of HTSC grains. Strontium in PST is a reservoir of holes in the PST-YBCO composite. When the fraction of PST increases, the hole concentration

inside the YBCO superconducting grain rises. Hence changes of the dispersion of the YBCO-PST composite make it possible to pass smoothly through the crossing point with the carrier concentration. The crossing point phenomena related to stable x_1 and x_{opt} shifted towards lower temperatures can be related to changes in the symmetry of pairing mechanisms [7, 20].

4. Modelling the effect of pressure on T_c in HTSC

The pressure effect has been recently discussed on the basis of the extended Hubbard model, in particular the influence of pressure on the parabolic character of the $T_c(x, p)$ dependence in HTSC [21]. It has been concluded that the pressure effect is related to a pressure induced charge transfer from the reservoir of holes to the CuO_2 planes. The data for the Hg-1201 material also suggest the existence of an intersection point that leads to the sign change of dT_c/dp . It has been found that the hopping integral depends on pressure and that T_c is proportional to the pressure applied in the underdoped regime [22].

According to the model of local pairing, two important lines can be drawn on the phase diagram of HTSC (Fig.6): a line of pair correlations (T^*), at which carriers form LP's, and a coherence line (T_c), below which the superconducting condensate is formed [23].

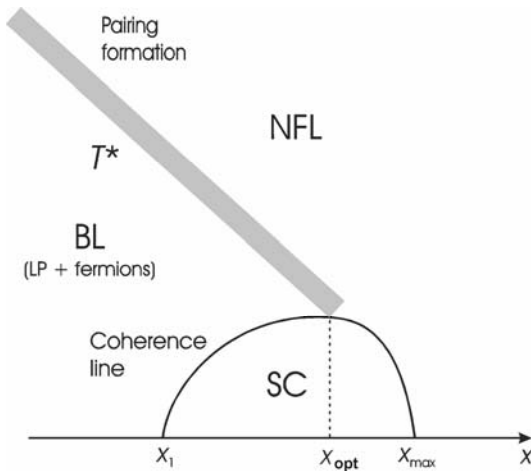


Fig. 6. A line pair correlation T_{LP} separating the Fermi liquid (FL) and Bose liquid (BL) regions (the latter is formed by nearly free LP) and the phase correlation line, T_c , enclosing the superconducting condensate (SC)

One should also add that Abrikosov [24], in his analysis of fluctuation effects, proposed the formation of superconducting filaments in one crystal direction only, i.e., of one-dimensional superconducting channels. Such channels that occur beyond the percolation threshold can induce the superconductivity of a sample. Nonuniform carrier distribution and strong fluctuations are essential phenomena in superconductors with low carrier concentration, for which there are two characteristic temperatures, T^* and T_c , as well as charge and spin pseudogaps.

For low carrier concentrations ($x_1 < x < x_{opt}$) at T^* , fermions start to bind into LP's (composite bosons), which condense at T_c . For large concentrations ($x_{opt} < x < x_{max}$), both characteristic lines eventually merge and $T^* = T_c$ which means that Cooper pair formation takes place at the same temperature at which the superconducting condensate emerges. A line of pair correlations can be considered as a formation line for bosons, attaining a macroscopic phase coherence only at T_c , at which the whole system is described by a single wave function.

Within the model of local pairing by Micnas and Robaszkiewicz [23], the pressure effects, measured by dT_c/dp , scale differently on both sides of the optimal carrier concentration x_{opt} . The transfer integral rises with increasing pressure. Therefore, the pressure coefficient is positive below x_{opt} , since T_c scales like $t^2/|U|$. However, T_c scales like $1/2zt$ above x_{opt} , which implies that the pressure coefficient is negative (like in the BCS model) (Fig.7).

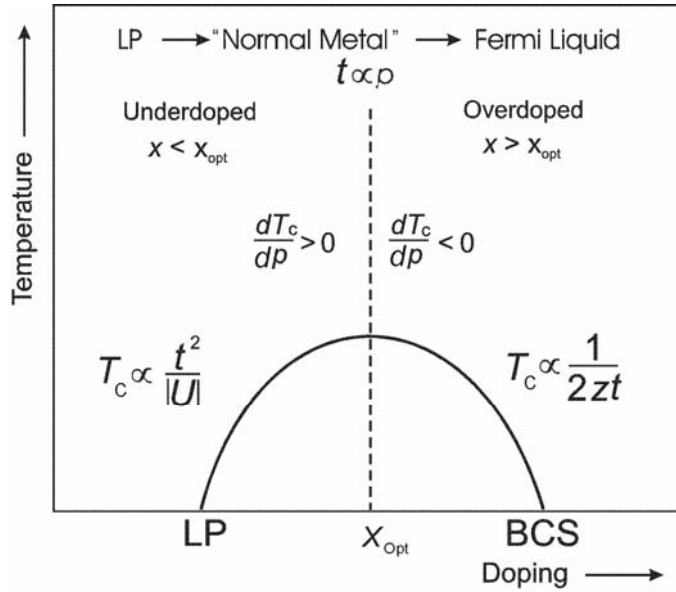


Fig. 7. Scaling of the pressure effect below ($x < x_{opt}$) and above ($x > x_{opt}$) the optimal carrier concentration

Close to T_c^{max} , the pressure coefficient is nearly zero. Hence, the pressure causes an enhancement of T_c in the concentration regime where two distinct characteristic temperatures, T^* and T_c , are present. If $T^* = T_c$, the pressure coefficient is negative and T_c is reduced by pressure like in "classical" superconductors'. Such a dependence was confirmed by experiment in the case of the composite YBCO-PST [19], for which positive and negative pressure coefficients of T_c were observed.

The different scaling of the pressure effect below and above x_{opt} can also have an explanation in a nonuniform and fluctuating charge distribution for small x , and

a homogeneous and relatively stable charge distribution for $x > x_{\text{opt}}$. For $x > x_{\text{opt}}$, $T^* \approx T_c$, because fluctuations are negligible. For $x < x_{\text{opt}}$, $T^* > T_c$ and pressure shifts the equilibrium from the s- to the d-state. This difference can be explained by a possible occurrence of a structural instability, leading to a phase separation and self-organized stripe array. The stripes are one dimensional metallic objects, “topological defects” in the antiferromagnetic insulator. The stripe structure slowly fluctuates, which can be taken as the effect of the phase separation. Emery et al. [20] introduced two T^* temperatures in their phase diagram. At T_1^* the stripe structure occurs. Charges are ordered along these stripes and charge correlations are 1D along the chain (there are no perpendicular correlations). At the temperature T_2^* a pairing takes place in metallic chains, giving rise to a spin gap. There is no coherence between neighbouring chains which suggests that one can observe “free Cooper pairs” in such a state. The phase coherence of these free pairs takes place at T_c and correlations between the pairs in neighbouring chains can result from Josephson coupling. The pressure effect is positive here, since the pressure increases the transfer integral t in the extended Hubbard model.

Recent calculations by Micnas and Tobijaszewska show that the expansion of the pseudogap region associated with mixing of s and d-wave components gives rise to an additional increase in T_c in the underdoped regime [25]. Above the concentration x_{opt} , the lines $T^*(x)$ merge with the line $T_c(x)$ and BEC takes place in the metallic region, where charge and phase fluctuations can be neglected like in the BCS model. Hence, the pressure effect is negative here. However, the experimentally discovered shift of x_{max} towards lower concentrations still remains unexplained.

Acknowledgements

This work was supported in part by the Polish State Committee for Scientific Research (KBN), Project No. 5 P03B 061 20. We would like to thank S. Robaszkiewicz for helpful discussions.

References

- [1] BEDNORZ J.G., MILLER K.A., *Z. Phys.*, B64 (1986), 189.
- [2] ANDERSON P.W., *Science*, 288 (2000), 480.
- [3] BRINKMANN D., MALI M., *NMR Basic Principles and Progress*, Springer-Verlag, Berlin, 1994, Vol. 31, p. 171.
- [4] GRIESSEN R., *Phys. Rev.*, B36 (1987), 5284.
- [5] ALLEN P.B., DYNES R.C., *Phys. Rev.*, B12 (1975), 905.
- [6] LABBÉ J., BOK J., *Europhys. Lett.*, 3 (1987), 1225.
- [7] ANDERSON P.W., *Science*, 235 (1987), 1196.
- [8] ALEXANDROV A. S., RANNINGER J., ROBASZKIEWICZ S., *Phys. Rev.*, B33 (1986), 4526.
- [9] DRIESSEN A., GRIESSEN R., KOEMAN N., SALOMONS E., BROUWER R., DE GROOT D.G., HEECK K., HEMMES H., RECTOR J., *Phys. Rev.*, B36 (1987), 5602.
- [10] TALLON J.L., BERHARD C., SHAKED H., HITTERMAN R. L., JORGENSEN J.D., *Phys. Rev.*, 51 (1995), 12911.
- [11] GOLDSCHMIDT D., KLEHE A.-K., SCHILLING J.S., ECKSTEIN Y., *Phys. Rev.*, 53 (1996), 14631.
- [12] SADEWASSER S., SCHILLING J.S., PAULIKAS A.P., VEAL B.W., *Phys. Rev.*, B61 (2000), 741.

- [13] LIAROKAPIS E., LAMPAKIS D., NISHIZAKI T., PANAGOPOULOS C., *High Pressure Res.*, 18 (2000), 109.
- [14] KALDIS E., RÖHLER J., LIAROKAPIS E., POULAKIS N., CONDER K., LOEFFEN P.W., *Phys. Rev. Letters*, 79 (1997), 4894.
- [15] NUEMEIER J. J., ZIMMERMANN H.A., *Phys. Rev.*, B47 (1993), 8385.
- [16] JOVER D.T., WILHELM H., WIINGAARDEN R.J., LIU R.S., *Phys. Rev.*, B55 (1997), 11832.
- [17] GUPTA R. P., GUPTA M., *Phys. Rev.*, B50 (1994), 9615.
- [18] PICKETT W.E., *Physica*, C289 (1997), 51.
- [19] KRUPSKI M., STANKOWSKI J., PRZYBYŁ S., ANDRZEJEWSKI B., KACZMAREK A., HILCZER B., MARFAING J., CARANONI C., *Physica C320* (1999), 120.
- [20] EMERY V.J., KIVELSON S.A., ZACHAR O., *Phys. Rev.*, B56 (1997), 6120.
- [21] DE MELLO E.V.L., ACHA C., *Phys. Rev.*, B56 (1997), 466.
- [22] CAIXEIRO E.S., DE MELLO E.V.L., *Physica*, C383 (2002), 89.
- [23] MICNAS R., ROBASZKIEWICZ S., [in]: *High- T_c Superconductivity 1996: Ten Years after the Discovery*, E. Kaldis, E. Liarokapis, K.A. Miller (Eds.), NATO ASI Series E, Kluwer Academic Publishers, The Netherlands, Vol. 343 (1997), p. 31.
- [24] ABRIKOSOV A.A., *Phys. Rev.*, B63 (2001), 134518; *ibidem* B64 (2001), 104521.
- [25] MICNAS R., TOBIASZEWSKA B., *Acta Phys. Polon. B*, 32 (2001), 3233.

Received 5 May 2004

Revised 27 July 2004

Photochromic sol-gel derived hybrid polymer coatings: the influence of matrix properties on kinetics and photodegradation

ANNA KLUKOWSKA¹, UWE POSSET^{1*}, GERHARD SCHOTTNER¹,
ANNA JANKOWSKA-FRYDEL², VINCENZO MALATESTA³

¹Fraunhofer-Institut Silicatforschung (ISC), Neunerplatz 2, D-97082 Würzburg, Germany

²Institute of Experimental Physics, Gdańsk University, Wita Stwosza 57, 80-952 Gdańsk, Poland

³Current address: Cytec Industries Inc., 1937 West Main Street, 06904 Stamford, Connecticut, USA

Photochromic dyes undergo a reversible change in their absorption characteristics upon UV light irradiation. By incorporating such photochromophores into sol-gel derived inorganic-organic hybrid polymers, versatile coatings with a fast photochromic response and high photochromic activity can be obtained. In the present study, the isomerization kinetics of spirooxazine dyes entrapped in hybrid polymer coatings were investigated in situ. The chemical properties of the matrices used were characterised in terms of their inorganic network connectivity (NMR measurements) and paramagnetic properties (EPR spectroscopy). Their photodegradation behaviour was studied by means of artificial weathering.

Key words: photochromic dyes; switching kinetics; sol-gel materials; hybrid polymer 1

1. Introduction

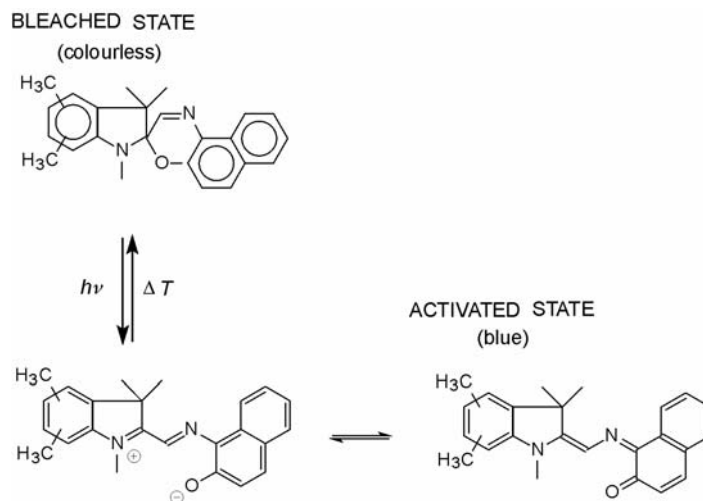
Sol-gel derived inorganic-organic (hybrid) molecular composites are used in a wide range of applications, such as laser optics, data storage, and antiscratch and antireflective coatings, e.g., on optical and ophthalmic components. This is due to the multiple advantages offered by their high transparency and low processing temperatures and the availability of suitable precursors [1]. Hybrid polymers (ORMOCER^{®s}**) combine, to a certain extent, advantages of inorganic glasses (hardness, transparency, chemical resistance) and organic polymeric materials (modification of

*Corresponding author, e-mail: posset@isc.fhg.de.

**Trademark of the Fraunhofer-Gesellschaft zur Förderung der angewandten Forschung e.V., Munich.

chemical environments, control of composite properties, low processing temperatures).

A photoinduced change in the absorption of a molecule by a reversible process is referred to as photochromism [2]. Usually an uncoloured form A undergoes isomerisation to a coloured form B, exhibiting a different absorbance behaviour. The spirooxazine dyes investigated in this work are characterised by a relatively weak $C_{\text{spiro}}-O$ bond, which, by a heterolytic cleavage caused by UV irradiation (“on-reaction”), forms a planar merocyanine-type structure (Scheme 1) [3].



Scheme 1. Photochromic reaction of Blue D

The half-life time of the thermally induced bleach back process (“off-reaction”) can range from seconds to minutes [4]. Organic photochromes can be chemically modified in such a way that covalent attachment to an inorganic network becomes possible (see the inset in Fig. 1) [5]. Sol-gel matrices provide a stable environment for the chromophores, preventing their self-aggregation and interaction with the degradation products. Optical transparency in both the UV and visible light region and low processing temperature makes these kinds of materials attractive for the incorporation of photochromic dyes [6–8]. By tuning the nature of the matrix and dye the optical response can be optimized. The photochromic properties can be strongly modified by the presence of polar groups (i.e. $Si-OH$), complexation, protonation, matrix rigidity and steric hindrance [9, 10]. Strong interactions between the dye and host matrix reduce dye mobility and thus the thermal decoloration rate. A very good example are matrices made from hydrophobic polydimethylsiloxane species cross-linked by hydrophilic zirconium oxopolymers, used as hosts for spirooxazine (SO) and spiropyran (SP) dyes. The amount of the coloured form after irradiation depends on the molar percentage of the zirconium oxopolymer domains. In the hydrophobic matrix, where the $Si-OH$ groups are fully hydrolysed, direct and very fast photochromism can be

observed [11]. Some advantages of this type of incorporation, such as an increase in photochromic activity and photochemical stability, have been reported earlier [6].

The matrix systems chosen in the present study have been proven to be suitable systems for the incorporation of organic photochromes. Epoxy-functional alkoxysilane hydrolysates were cross-linked with anhydrides and amines to produce matrices of different network density and polarity.

2. Experimental section

2.1. Chemicals

The photochromic dyes Variacrol[®] Blue D (1,3,3,5,6-pentamethylspiro-[indolino-naphthoxazine]), its silylated derivative (hereinafter called graftable Blue D, gr. Blue D; inset in Fig. 1, Table 2), a spiro-isoindolinooxazine analogous in structure to Blue D (Blue C, Table 2), a spiro-indolinooxazine with a 5'-morpholino-1,3,3-trimethyl substitution (PNO, Table 2), a red-switching chromene with proprietary structure (Red A, Table 2), and the chromene 3,3-diphenyl-3H-naphtho[2,1-b]pyran (Photo L, Table 2) were kindly supplied by Great Lakes Chemical Corporation, Italy.

Blue A (1,3-Dihydro-1,3,3-trimethylspiro[2H]-indole-2,3-[3H]naphth[2,1-b][1,4] oxazine), CAS-No. 27333-47-7) was purchased from Aldrich.

3-Glycidoxypopyl trimethoxysilane (GPTMS), 3-aminopropyl triethoxysilane (APTES), and methyl diethoxysilane (DH) were ABCR products. 3-triethoxysilylpropyl succinic anhydride (TESSA), cis-hexahydrophthalic anhydride (HHPA), and phenyl trimethoxysilane (PhTMO) were purchased from Wacker Chemie, Fluka, and Aldrich, respectively. All chemicals were used without further purification. THF and *n*-Propanol were purchased from Promochem and used as received.

2.2. Preparation of materials

Preparation of the GG matrix: H₂O and an amine catalyst were added to GPTMS placed in a round bottom flask in the molar ratio GPTMS : H₂O : cat. = 1 : 1.5 : 0.05, and the mixture was stirred. After hydrolysis was complete (as determined by Raman spectroscopy [12]), *n*-PrOH (100 g per mole of GPTMS) and TESSA (molar ratio GPTMS : TESSA = 1 : 0.5) were added. After stirring for 1 h the mixture was in a ready-to-apply condition.

Preparation of the GB matrix: GPTMS and PhTMO in the molar ratio 0.75 : 0.25 were placed in a round bottom flask and stirred. Subsequently, H₂O and an amine catalyst in the molar ratio GPTMS : H₂O : cat. = 0.75 : 1.5 : 0.0375 were added and the mixture was stirred until hydrolysis was complete. Finally, *n*-PrOH (100 g per mole of GPTMS) and HHPA (molar ratio GPTMS : HHPA = 0.75 : 0.375) were added. After stirring for 1 h the sol was in a ready-to-apply condition.

Preparation of the GA10 matrix: H₂O and an amine catalyst were added to GPTMS placed in a round bottom flask in the molar ratio GPTMS : H₂O : cat. = 1 : 1.5 : 0.05, and the mixture was stirred. After hydrolysis was complete, *n*-PrOH (100 g per mole of GPTMS) and APTES (molar ratio GPTMS : APTES = 0.9 : 0.1) were added. After stirring for 1 h the mixture was in a ready-to-apply condition.

Preparation of the GAD matrix: H₂O and an amine catalyst were added to GPTMS placed in a round bottom flask in the molar ratio GPTMS : H₂O : cat. = 1 : 1.5 : 0.05, and the mixture was stirred. After hydrolysis was complete, *n*-PrOH (100 g per mole of GPTMS) and APTES (molar ratio GPTMS : APTES = 0.9 : 0.1) were added. After APTES was fully hydrolysed, DH (GPTMS : DH = 0.9 : 0.25) was subsequently added. After 30 minutes of stirring the mixture was in a ready-to-apply condition.

The dyes were dissolved in mixtures of THF and *n*-PrOH (wt. ratio 2:1), so that the total amount of additional solvent in the coating sol did not exceed 30 wt. %. In order to ensure that materials with identical chromophore concentrations were investigated, the mass of the side chain was taken into account in the mass calculation of the silylated dye. Variacrol[®] Blue D was added to the prepared sols as an additive. Graftable Blue D was added at an earlier stage, in order to allow its co-condensation with the polysiloxane oligomers that formed during the sol-gel process. For the hydrolysis of the dye, an additional amount of water was added in the molar ratio graftable Blue D : H₂O = 1 : 1.5.

The chromophore concentration was 3 wt.% with respect to the solids of the sols.

The freshly prepared systems were spin-coated on glass slides and CR 39[®] lenses, and cured thermally at 125 °C for 20 min. The glass slides and lenses were cleaned prior to coating as follows: after immersion in NaOH for 5 minutes (50°C), the substrates were washed with deionized water, placed in a ultrasonic water bath for 3 min, washed again with deionized water and dried with compressed air.

For NMR and EPR measurements, powdered samples were prepared from dyed and undoped gels and dried in aluminum vessels at 125 °C for 20 min.

2.3. Test devices and measurements

The hydrolytic reactions of alkoxy silanes were followed by means of a FT-Raman spectrometer (Bruker, model RFS 100). Spin-coating was performed by means of a KSM Karl Süss spin coater, model RC8. Thermal curing was done by means of Heraeus drying ovens. For the activation of the photochromic coatings, a commercially available UV-A source (Philips face tanner, model HB170) equipped with Philips CLEO 15 W UV-A lamps was used. The integrated power density on the sample was 44 W/(cm²·min) between 250–410 nm. The lamp–sample distance was adjusted to 12 cm. The transmittance spectra were measured and ΔY values (photochromic activity) calculated by means of a colorimeter BYK-Gardner, model the Color Sphere. Prior to each measurement, the samples were activated, manually transferred into the measurement chamber of the spectrometer, and the spectra recorded with a delay of

2 s. Kinetic investigations were performed “in situ” by means of a custom-made set-up comprising a HBO 200 W Hg lamp, a water filter for heat absorption, a colorimeter, and a sample holder placed in the spectrometer. The sample holder allowed the sample to be fixed in the optical path with a tilt angle of 45°.

The photochemical degradation of the photochromic coatings was studied by means of an air cooled Suntest chamber (ATLAS Material Testing Technology BV, model Suntest CPS+), which was equipped with a 1100 W Xenon lamp (according to DIN ISI 9000ff specification). The average irradiance was 750 W/m². After each irradiation interval, all samples were exposed to a bleach-back procedure comprising a heat treatment at 75 °C for 20 min and irradiation with visible light (standard fluorescence bulbs) for 1 h, followed by dark storage for at least 2 h at ambient temperature.

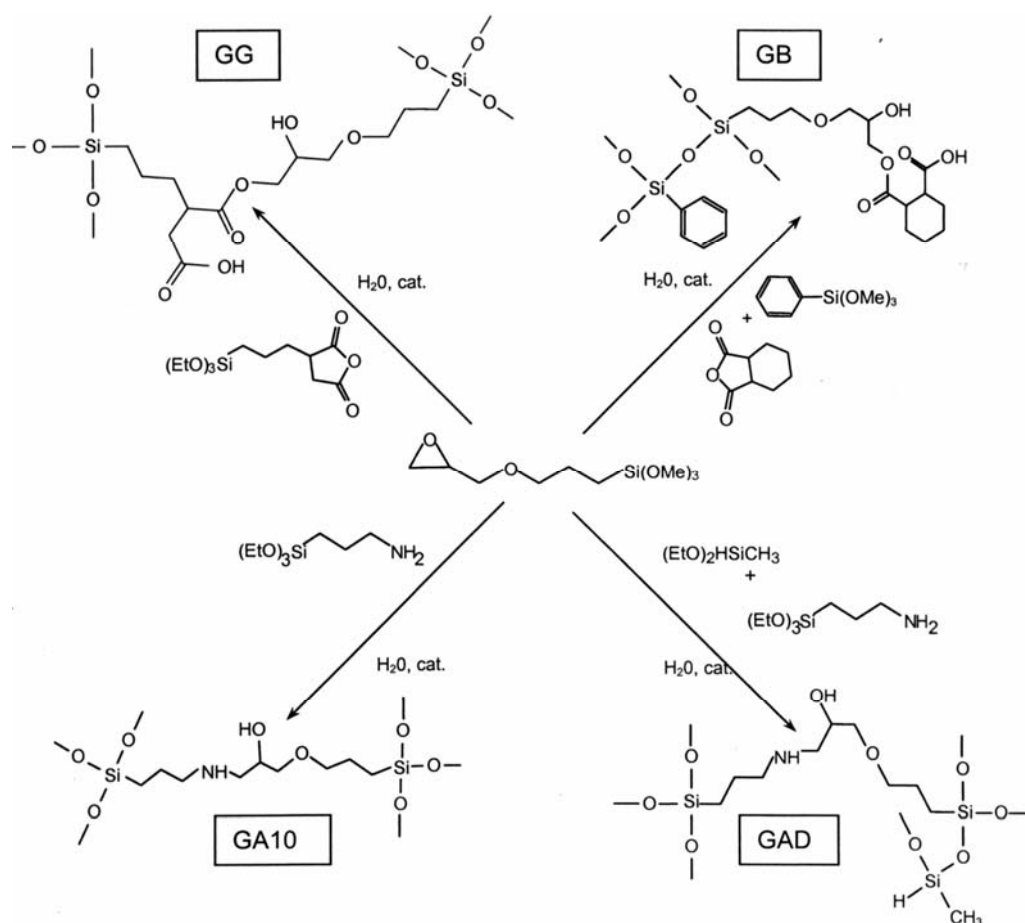
Solid state quantitative MAS-NMR measurements were performed on a Bruker DSX 400 spectrometer. The paramagnetic properties were investigated by means of a standard SE/X spectrometer (Radiopan, Poznań), the sample holders were sealed quartz capillaries (1 mm in diameter). The magnetic field was calibrated using diphenylpicrylhydrazyl (DPPH) free radicals and modulated at 100 kHz. The EPR spectra were obtained at 9.4 GHz (X-band) and displayed as the first derivative of the respective absorption curves. For the photochemical degradation of EPR samples, a HBO 200 W mercury lamp was used. The powders were irradiated for 4 h at a lamp-sample distance of 0.5 m.

3. Results and discussion

3.1 . Types of matrices used

Four matrix types were chosen as hosts for the photochromic dyes. The advantages and disadvantages of each of the hosts are demonstrated below. The main crosslinking reactions postulated to occur during thermal curing are shown in Scheme 2.

The GG system is a hybrid polymer with inorganic polysiloxane backbones and polyether/polyester-like crosslinks, which arise from the thermally induced polyaddition reaction of epoxide and anhydride groups. The hydrolysis and polycondensation of the alkoxy silane groups can be carried out at mild conditions and ambient temperature. Organic polyaddition starts at temperatures above approximately 100 °C. As was assessed by microhardness measurements, the GG matrix showed a relatively high rigidity. The universal microhardness was determined to be 110 N/mm² for this system. Contrary to that, the GB matrix, which exhibits a lower network density and higher amount of organics, showed the microhardness of only 60 N/mm². It is known that both GG and the GB coating solutions have very low contents of residual water (less than 1 wt.%) due to its immediate consumption by anhydride groups, which results in the formation of carboxylic acid species. Thus, GG and GB are both weakly acidic, and were expected to have a relatively low concentration in silanol groups and to differ in their cross-linking density.



Scheme 2. Main precursors and postulated structures of the hybrid polymer host materials GG, GB, GA10 and GAD

The GA10 matrix, whose characteristic structural feature is the β -aminoalcohol cross-link, is a basic system with no Brønsted acid components. The water content of GA10 coating solutions was in the range of approximately 5 wt. %. The GAD system, whose development was based on the GA10 system, has an even lower polarity in the cured state as a result of a linear silicone-type backbone and the incorporation of methyl groups. Therefore, GA10 and GAD are both basic in nature, but should differ in their polarities.

3.2. Network connectivity according to NMR spectra

The photochromic behaviour of the incorporated chromophores strongly depends on the network characteristics of the sol-gel matrix (the cage effect) [13]. When the rigidity of the host is high, organic molecules within it will be completely immobi-

lised and separated from each other (and their degradation products). This may positively affect the photochemical activity and result in significant stabilisation [6]. Kinetics are determined by factors such as dye structure and rigidity, matrix micropolarity, the type of incorporation, and temperature. In a less polar environment, the closed, uncoloured, less polar forms of spirooxazines would be favoured, while a more polar environment would stabilise the more polar merocyanine (or even zwitterionic) form [3, 14].

In the present study, solid state ^{29}Si -MAS-NMR and Raman spectroscopy were used to characterise the microenvironments supposed to surround the chromophores. The inorganic network density was measured for powdered bulk samples. Solid state ^{29}Si -MAS-NMR spectroscopy yielded valuable insight into the level of inorganic connectivity and allowed the concentration of relevant silicon structural units to be determined (Table 1).

Table 1. ^{29}Si solid state NMR chemical shifts and inorganic network connectivity

GG		GB		GA10		GAD	
δ [ppm]	Assignment	δ [ppm]	Assignment	δ [ppm]	Assignment	δ [ppm]	Assignment
66,5	T ³ (~74%)	80,9	Si-Ph (~21%)	67,5	T ³ (~77%)	67,8	T ³ (~78%)
60,1	T ² (~22%)	67,3	T ³ (~79%)	59,9	T ² (~23%)	60,1	T ² (~22%)
52,8	T ¹ (~4%)						

A signal with a chemical shift δ around 67 ppm in the ^{29}Si -MAS-NMR spectrum can be assigned to the completely hydrolysed and polycondensed species T³, which forms a three-dimensional polysiloxane network. In GG, GB and GAD matrices T³ species were detected to a maximum of 79%. Partly condensed T² and T¹ species, bearing residual alkoxy or OH groups [1, 15], were found to be present to about 20 %. Only matrix GB behaves somewhat differently, in that solely T³ moieties could be found. The resonance at $\delta = 80.9$ ppm can be attributed to T³ groups with the substituents on the silicon atoms being phenyl groups originating from the PhTMO component of the GB system [16]. Thus, unlike GG, GA10, and GAD, which contain residual hydroxyl or even alkoxy groups, the GB matrix is supposed to consist of a fully hydrolysed and completely condensed polysiloxane network. The pore size and distribution of the materials have not been investigated in this study. It can be, however, assumed that the free volume is higher in the GB than the GG matrix, which is due to the lacking contribution of the (purely organic) anhydride cross-linker to the polysiloxane network.

3.3. Photochemical stability

The photodegradation behaviour of Blue D and graftable Blue D under artificial weathering has been reported elsewhere [6]. For the sake of clarity, the transmittance

spectra of the activated state of a graftable Blue D doped coating after continuous irradiation for 28 h and 60 h are presented in Figure 1. The degradation mechanism of spirooxazines is known to involve radicals [17]. Therefore, in this study it was attempted to take their presence, i.e., the concentration of paramagnetic species as an indication of dye photostability.

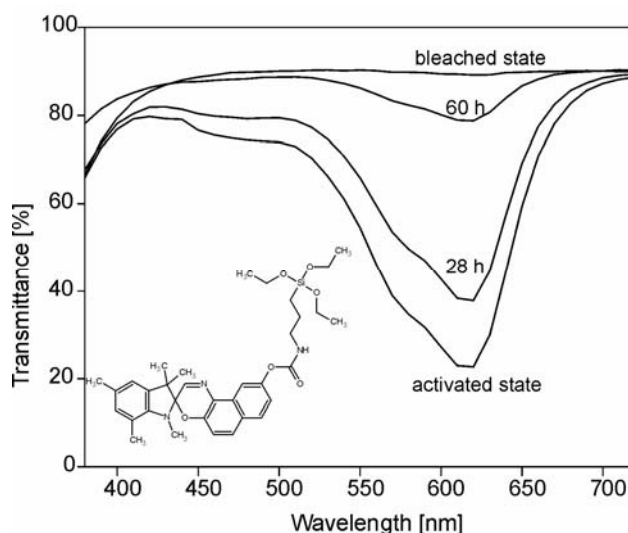


Fig. 1. Transmittance spectra of graftable Blue D (inset) entrapped in the GG host, prior to and after artificial weathering for 28 h and 60 h (Suntest®)

By means of EPR spectroscopy on powdered bulk samples of the pure matrices as well as on two series of doped samples (with Blue D and gr. Blue D), radicals could be detected in a few cases even though the samples were non-irradiated. The results are displayed in Figure 2a. Substantial amounts of radicals were found for undoped and doped GAD samples as well as for undoped GG and GA10 samples. The highest radical concentration was observed for the sample with gr. Blue D covalently bonded in the GAD matrix.

Figure 2b demonstrates the effect of continuous UV irradiation for 4 h. The EPR spectra were recorded immediately after the irradiated samples were transferred to the measurement chamber of the EPR spectrometer. As expected, the EPR signal intensity rose upon irradiation. This was particularly marked for Blue D doped samples, where the intensity signal increased by a factor of 10. Interestingly, the radical concentration of the graftable Blue D/GAD system was not affected by UV irradiation. Among all other samples, however, the GAD matrix was found to be the worst in terms of photoinitiated radical production.

The sharp single EPR signals showed a g factor between 2.003 and 2.0045, with neither splitting nor fine structure. This indicates an anisotropic location or migration of the detected radical species. Moreover, due to the absence of any Si–C or Si–O

splitting, the radicals are supposedly not associated with the photolysis of polysiloxane chains [18, 19].

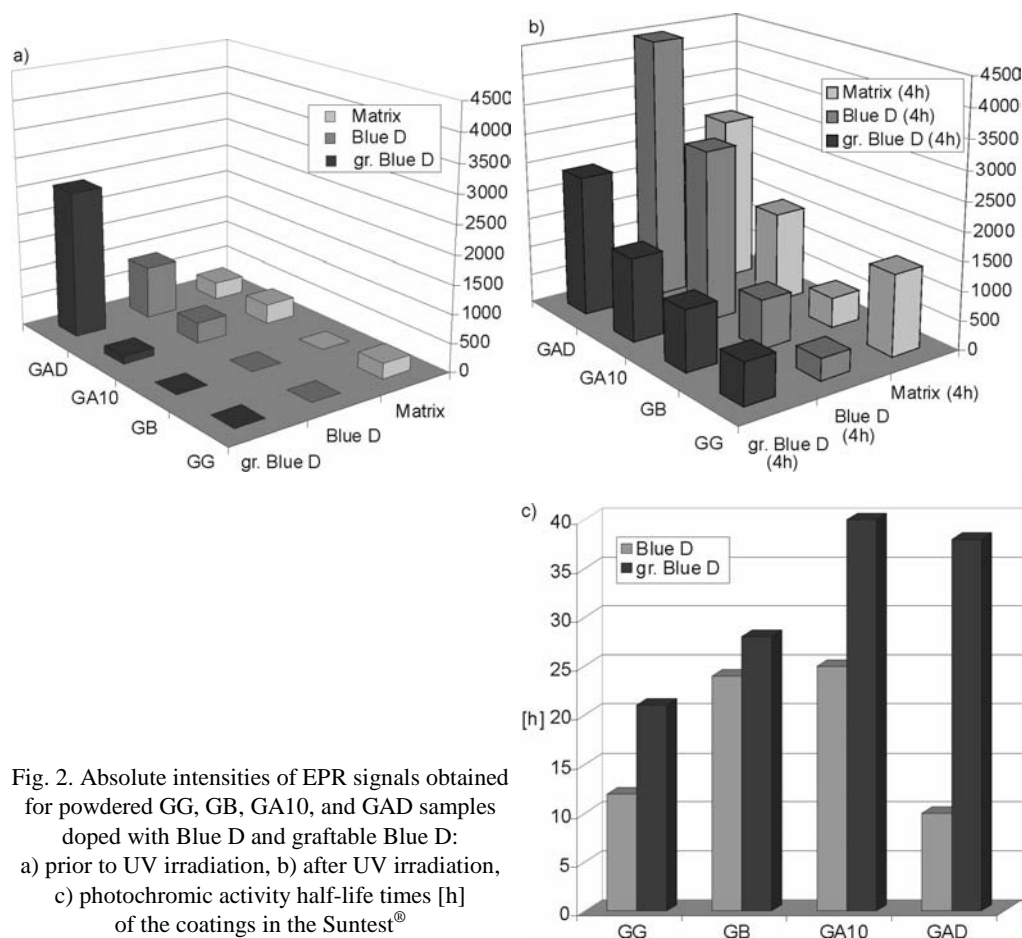


Fig. 2. Absolute intensities of EPR signals obtained for powdered GG, GB, GA10, and GAD samples doped with Blue D and graftable Blue D: a) prior to UV irradiation, b) after UV irradiation, c) photochromic activity half-life times [h] of the coatings in the Suntest®

Radical centres that are present before UV irradiation could originate from an accidental irradiation with visible light during sample preparation, the energy of which (~ 2.5 eV) is sufficient to create some magnetic centres. In the cases where no radical activity is observed after visible light irradiation only, the energy gap to the excited state may have been too high. After irradiation with UV light (energy ~ 5 – 10 eV) the number of the active centres rises. The form and g -factors of the EPR signals are not changed, which means that the characteristics of the magnetic species are the same. All EPR signals of the measured samples have a g -factor similar to that of a free electron ($g = 2.0023$), thus the magnetic centres are of the 1-electron “free radical” type. In most cases, the radicals have isotropic environments. In a few cases, when the asymmetric EPR signals are present, the isotropy is slightly distorted.

Upon storage for 24 h in the dark, the EPR signal intensities of previously irradiated samples decreased to the initial level, probably due to diffusion-controlled recombination processes. When irradiated again, the EPR signal intensities increased as before.

In order to correlate the EPR results with the actual photodegradation behaviour, coated glass samples were irradiated in a Suntest weathering device and the transmittance of the samples was measured after 4 h intervals of exposure. The non-silylated dye showed higher half-life times in soft and polar matrices (GB and GA10) (Fig. 2c). This finding did not correlate with the large difference in the amount of radicals detected after UV light irradiation in the respective powdered samples (Fig. 2a, b). The GG and GAD matrices, rigid polar and soft non-polar systems, respectively, turned out to be less suitable for the physically embedded spirooxazine. This again was in disagreement with the concentration of radicals after irradiation (low for GAD, high for GG). For samples doped with graftable Blue D, an increase in the radical concentration identical to the pure matrix was found. This in general correlates with the previously obtained result that graftable dyes have higher photochemical stability than the corresponding physically entrapped dyes.

3.4. Switching kinetics

For the investigation of switching kinetics, coated glass samples were irradiated in situ in the measurement chamber by means of a UV lamp (HBO 200 W Hg lamp). The change in optical density was determined in intervals of 2 s during activation as well as during bleaching.

Dyes entrapped in hybrid polymers generally showed slower kinetics than the corresponding solutions in organic solvents (see Table 2) [4, 20]. This was particularly evident for the fading processes. Nonetheless, the differences were small and indicated a high degree of mobility for the incorporated chromophores.

Table 2. The kinetics of several photochromic dyes;
 t_a – activation time for 50 % of the maximum transmittance, t_f – fading time, both in seconds

Dye	GG		GB		GA10		Methanol		Hexane	
	t_a	t_f	t_a	t_f	t_a	t_f	t_a	t_f	t_a	t_f
Blue A ^a	4.7	5.8	1.4	6.2	3.4	3.2	2	1	3	4
Blue C ^b	20.5	93.6	10.3	63	14.7	28.6	–	–	–	–
Blue D	6.2	9	5.3	9.6	5.5	8.9	6	12	4	4
PNO ^c	3.9	2.8	3.7	5.2	4.1	1.8	2	1	2	>24
Red A ^d	7.5	129.1	4.8	57	5.8	26.6	–	–	–	–
Photo L ^e	7.4	9.1	5.5	10	3.9	13.6	6	11	5	12

It is apparent that covalent attachment noticeably slowed down the “off-reaction“, which is probably due to steric hindrances and restricted chromophore mobility (i.e.,

restricted ability to re-orientate within the free volume of the matrix). The determined bleaching kinetic curves could be fitted by means of a second order exponential decay (Fig. 3).

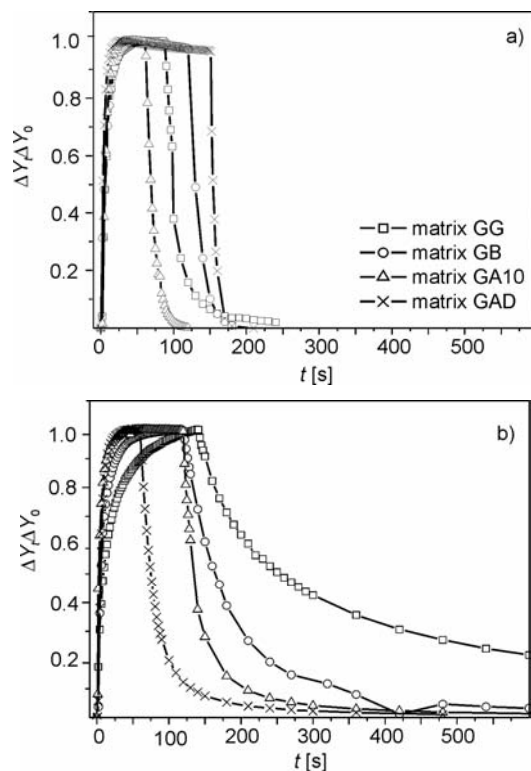


Fig. 3. On/off kinetics of spirooxazines entrapped in the four hybrid polymer matrices, GG, GB, GA10, and GAD: a) Blue D, b) Graftable Blue D. ΔY_t – change of luminous transmittance after irradiation for a given time t , ΔY_0 – change of luminous transmittance at maximum colouration (photochromic activity)

It can be seen that both matrix rigidity and polarity have an influence on the switching kinetics. The large difference between the covalently bonded and physically entrapped dyes is clearly evident, for example, in the off-reaction of graftable Blue D in the GG system, which proceeds slower than for Blue D by about a factor of 10 (squares in Figs. 3a, b). For the other matrices the effect is observable as well, but less pronounced. It is conceivable that on the one hand the polar carbonyl and silanol sites of the GG host material are particularly effective in stabilising the opened merocyanine form, thus causing slower bleaching, and on the other hand the back reaction is sterically hindered as a result of the covalent attachment to a matrix that is considered to be the most rigid one (GG). In agreement with this hypothesis, fast on- and off-kinetics were observed when the dyes were physically entrapped in the more soft and unpolar host materials.

It is apparent (squares and circles in Fig. 3b) that the bleaching kinetics differ for GG and GB matrices. This may be attributed to both the differences in network densities (i.e., free volume) and polarities. As pointed out before, GB, derived from an organic anhydride cross-linker should have a higher free volume and lower rigidity than the GG material, whereas GG is clearly more polar than GB. All these factors may have contributed to the observed differences in kinetic behaviour.

The amine cross-linked systems GA10 and GAD behaved very similar in terms of colouration, but showed higher bleaching rates as compared to the anhydride cross-linked systems GG and GB.

4. Conclusions

The switching kinetics and photochemical stability of photochromophores were found to depend strongly on the chemical properties of the matrix they are entrapped in, and on the type of entrapment. Significant differences were observed for physically entrapped and covalently bonded chromophores. The results allow the most suitable molecular environment to be chosen for a given dye in terms of photostability, kinetics and activity – this is considered to be relevant for potential applications in the ophthalmic sector. In order to create optimised microenvironments, further investigations on the micropolarity and chemical character of the radical species present in the irradiated samples are necessary. Low temperature EPR is considered to reveal valuable information in this respect.

Acknowledgements

A. J-F. thanks the Gdańsk University for the supporting grant No. BW/5200-5-0316-3. A. K. thanks the Bayerische Forschungsstiftung for a scholarship.

This work has been funded in part by the European Commission (Brite-Euram BE 3380), which is gratefully acknowledged.

References

- [1] BRINKER C.J., SCHERER G.W., *Sol-Gel Science: The Physics and Chemistry of Sol-Gel Processing*, Academic Press Inc., San Diego, 1990.
- [2] BROWN G.H. (Ed.), *Photochromism*, Wiley-Interscience, New York, 1971.
- [3] FISCHER E., HIRSHBERG Y., *J. Chem. Soc.*, 1952, 4522.
- [4] MALATESTA V., *Photodegradation of Organic Photochromes*, [in:] J.C. Crano and R. Guglielmetti (Eds.), *Organic Photochromic and Thermochromic Compounds*, Kluwer, New York, 1999, p. 65.
- [5] SCHOTTNER G., *Chem. Mater.*, 13 (2001), 3422.
- [6] KLUKOWSKA A., POSSET U., SCHOTTNER G., WIS M.L., SALEMI-DELVAUX C., MALATESTA V., *Mat. Sci.* 20 (2002), 95.
- [7] CRANO J.C., KWAK W.S., WELCH C.N., *Spirooxazines and their use in photochromic lenses*, [in:] C.B. McArdle (Ed.), *Applied Photochromic Polymer Systems*, Blackie & Son Ltd., New York 1992, p. 31.
- [8] KWAK W.S., CRANO J.C., *PPG Technology Journal*, 2, (1996), 45.

- [9] LEVY D., EINHORN S., AVNIR D., J. Non-Cryst. Solids, 113 (1989), 137.
- [10] LEVY D., AVNIR D., J. Phys. Chem., 92 (1988), 4734.
- [11] SANCHEZ C., RIBOT F., LEBEAU B., J. Mater. Chem., 9 (1999), 35.
- [12] POSSET U., LANKERS M., KIEFER W., STEINS H., SCHOTTNER G., Appl. Spectr., 47 (1993), 1600.
- [13] AVNIR D., LEVY D., REISFELD R., J. Non-Cryst. Solids, 74 (1985), 359.
- [14] GUGLIEMETTI R., *4n+2 systems: Spiropyrans*, [in:] H. Dürr and H. Bouas-Laurent (Eds.), *Photochromism; Molecules and Systems*, Elsevier, Amsterdam, 2003, p. 314.
- [15] MARSMANN H.C., [in:] P. Diehl, E. Fluck and R. Kosfeld (Eds.), *NMR 17: Oxygen-17 and Silicon-29*, Springer-Verlag, Berlin, 1981, p. 66.
- [16] TAYLOR R.B., PARBHOO B., FILLMORE D.M., *Nuclear Magnetic Resonance Spectroscopy*, [in:] *The Analytical Chemistry of Silicones*, A. Lee Smith (Ed.), Wiley, New York, 1991, p. 347.
- [17] MALATESTA V., NERI C., WIS M.L., MONTANARI L., MILINI R., J. Am. Chem. Soc., 119 (1997), 3451.
- [18] ALBERTI A., CAMPREDO M., GIUSTI G., LUCCIONI-HOUZE' B., MACIANTELLI D., Magn. Reson. Chem., 38 (2000), 775.
- [19] MATSUI K., MOTEGI M., ITO K., Nucl. Instr. Methods Phys. Res. Sect. B, 116 (1996), 253.
- [20] *Photochromes GLCI Variacrols*, Great Lakes Chemical S.r.l., Milan, Italy, 1994, p. 1.

Received 19 April 2004

Revised 22 June 2004

Development of highly transparent and conducting yttrium-doped ZnO films: the role of sol-gel stabilizers

R. KAUR*, A.V. SINGH, R. M. MEHRA

Department of Electronic Science, University of Delhi South Campus, New Delhi 110021, India

Yttrium-doped zinc oxide (YZO) thin films were deposited with the dip coating technique. The effect of different sol-gel stabilizers (lactic acid with hydrolysis, without hydrolysis, and diethanolamine (DEA)) on structural, electrical and optical properties of the produced films were investigated. The stability of solutions prepared with DEA was much higher than that of other stabilizers. Films deposited using this solution also exhibited good adherence to the substrate, preferential orientation, and the lowest full width at half maximum of (002) X-ray diffraction peak. Average transmittance in the visible region increased by 14.6% and resistivity decreased by two orders of magnitude as the stabilizer was changed from lactic acid to DEA. The lowest resistivity, $3.5 \times 10^{-2} \Omega\text{-cm}$, and an average transmittance of 85% are obtained for 200 nm thick films annealed at 450 °C in air using DEA as a stabilizer.

Key words: *ZnO:Y; transparent conducting oxide; sol-gel; stabilizers*

1. Introduction

Transparent conducting oxide (TCO) films of tin, indium and zinc oxides (doped and undoped) have been extensively studied due to their high optical transmittance and electrical conductivity. These films are useful in photovoltaic and photothermal applications [1–3]. Unlike the more commonly used indium tin oxide, zinc oxide is a non-toxic, inexpensive and abundant material. It is chemically and thermally stable in hydrogen plasma processes which are commonly used for the production of solar cells [2, 4]. Non-stoichiometric pure ZnO is an n-type semiconductor, but its optical and electrical properties are not very stable at high temperatures [5]. However, doped films can be made which have very stable electrical and optical properties [6]. Therefore, doped ZnO films are preferred for practical purposes [7]. The doping effect of In, Al, and Ga on ZnO has been reported frequently by many research groups [4–7] but the use of a rare-earth impurity as a dopant, particularly Sc, Y has been scarcely

*Corresponding author, e-mail: rammehra@netscape.net.

reported, although their ionic radii are close to that of zinc, which makes them compatible for doping. Recently, Minami et al. reported that conductivity of RF sputtered ZnO films can be increased by Y-doping [8].

Several deposition techniques are used to grow ZnO thin films, including chemical vapour deposition (CVD) [4, 9], magnetron sputtering [10, 11], spray pyrolysis [12], pulsed laser deposition (PLD) [13, 14], and sol-gel method [7]. In comparison with other techniques, the sol-gel technique has the advantage of being low cost and allowing non-vacuum, low substrate temperature deposition. Since zinc belongs to the group of elements which easily form polymeric hydroxides (a fundamental requirement for the sol-gel chemistry), this technique can be easily used to deposit thin films of zinc oxide.

The usual starting materials for sol-gel processes are metal alkoxides. They are hydrolyzed to form sols, but they are expensive and their reactants are explosive. Therefore, many thin films have been prepared using metal salts [15,16]. A problem in the sol-gel process is the stability of the sol. Sometimes precipitation or gelation occur during its storage and application, affecting the quality of the films produced. Some kinds of acids are often used to accelerate or control the sol-gel process and are known as sol-gel stabilizers. Owing to these reasons, we have made an attempt in this study to investigate the effect of adding different sol-gel stabilizers, like (a) lactic acid with water, (b) lactic acid without water, and (c) diethanolamine (DEA) in ethanol as a solvent on the structural (*c*-axis orientation and surface morphology), electrical (resistivity, carrier concentration and Hall mobility) and optical (transmittance, band gap energy) properties of YZO films prepared by the dip coating technique. The effects of annealing temperature in air on these properties have also been investigated in the temperature range of 300–500 °C.

2. Experimental

A precursor solution of ZnO, about 0.2 M in concentration, was prepared from zinc acetate ($\text{Zn}(\text{CH}_3\text{CO}_2)_2 \cdot 2\text{H}_2\text{O}$, purity 99.5%) and dissolved in anhydrous ethanol. It was observed that the solutions prepared with concentrations greater than 0.2 M did not remain stable for a long time. Yttrium nitrate hexahydrate ($\text{Y}_2\text{NO}_3 \cdot 6\text{H}_2\text{O}$, purity 99.9%) was used as a dopant (3 wt. %) in the present study. The mixture obtained in such a manner was stirred in a magnetic stirrer for about 4 h at room temperature. It was observed that the solubility of zinc acetate was smaller in ethanol. Due to this, the associated acetate forms colloids and a milky solution is obtained. The sol-gel stabilizers were added to the respective solutions to eliminate/minimize the turbidity and precipitates. Various sol-gel stabilizers were added: lactic acid with hydrolysis (solution A), without hydrolysis (solution B), and DEA (solution C). Solution A was hydrolyzed with 2 moles of water per 1 mole of metal acetate by adding water dissolved in ethanol at 10 wt. % drop-wise, along with roughly 5 wt. % lactic acid in order to remove turbidity. Solution B was prepared using only lactic acid. It may be mentioned

that solution B had to be filtered in order to obtain a clear solution. An equimolar amount of DEA was added to solution C drop-wise to eliminate the obtained turbidity and precipitates completely. Clear, transparent, and homogenous solutions thus obtained were left to age for 48 hrs.

The corning glass (7059) substrates, after being cleaned with acetone and methanol in an ultrasonic bath for 20 minutes each, were rinsed with deionised water for 5 min and then dried in a nitrogen atmosphere. The glass substrates were dipped in the respective solutions (approximately 15 ml) at room temperature. The area of the dipped surface was $15 \times 20 \text{ mm}^2$. The substrate was withdrawn with a speed of 8 cm/min. Films were dried at 250 °C for 20 min. This cycle was repeated 10–15 times until the desired thickness was obtained. The thickness of the films was in the range of 200–250 nm. The deposited films were annealed in air in the temperature range of 300–500 °C for 1 h.

The structural properties of the films were investigated with a Phillips Holland X-ray diffractometer (Model PW 1830/00). The surface morphology of the films was analyzed with Scanning Electron Microscopy (JEOL JSM 6300). The thickness of the film was measured with a DEKTECK^{3-ST} surface profilometer. The electrical resistivity and Hall coefficient of the films were measured at room temperature with the van der Pauw technique. Optical transmittance measurements were carried out in the wavelength range of 200–800 nm using a double beam spectrophotometer (SHIMADZU 330). The proportion of yttrium to zinc of YZO films was found to be nearly equal to that in the solution, as determined by an Elemental Dispersion Analysis of X-ray (EDAX) measurements.

3. Results and discussion

Some of the parameters which control the quality of the films prepared with the sol-gel technique are: (i) ageing of the solution, (ii) wettability, and (iii) the stabilizer itself. Solutions A, B and C were observed with a magnifying glass in order to watch the changes in the sol with time. 72 h after the preparation of solution, it was observed that solution A showed turbidity/suspensions; its complete gelation took place in approximately a week. Solution B remained clear for 2 weeks. However, solution C remained transparent and stable even for 2 months.

The wettability of the solution with different stabilizers was examined simply by keeping the coated solution at room temperature for a longer time. If the solution is not repelled by the substrates even after 10 minutes, it exhibits good wettability. It was observed that solution C had the best wettability, and that the coated film remained uniform and smooth as compared to the films obtained from solution A. The films produced using solution A were non-uniform and had small dots (holes) at the edges and a relatively rough surface with a yellowish-white colour. This may be due to poor wettability and residual precipitates that may have developed during aging. Films made from solution B did not contain dots, and their surfaces seemed to be moderately uniform.

3.1. Structural properties

Structural properties of the films deposited under different conditions were examined by X-ray diffraction (XRD). As grown YZO films prepared from solutions A, B and C exhibited an amorphous nature, whereas films annealed at 350 °C showed evidence of a conversion from an amorphous to polycrystalline structure with (100), (002) and (101) peaks. However, no preferred orientation was observed. As the annealing temperature was increased from 350 to 450 °C, the (002) reflection peak became intense and sharper as compared to the others, indicating a tendency of preferential growth in the films. With a further increase in temperature, i.e. beyond 450 °C, there was a decrease in the intensity of all the peaks, which suggests a degradation of the quality of the films at higher temperatures [17]. This effect was common in films derived from all three solutions.

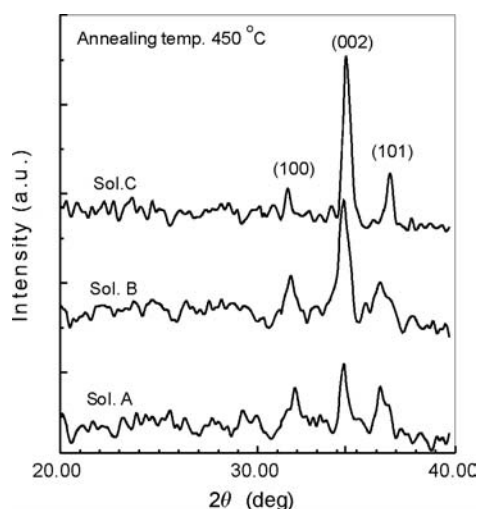


Fig. 1. XRD diffraction patterns of YZO films derived from different solutions annealed at 450 °C in air

Figure 1 shows the X-ray diffractograms for YZO films annealed at 450 °C and prepared from solution A, B and C. The highest (002) peak intensity was observed in films prepared using solution C. A shift in the (002) peak position to a higher 2θ value was also observed for these films with an increase of the annealing temperature. This shift approached the powder value of 34.44° at the temperature of 450 °C. This indicates a reduction in the tensile stress with annealing [16]. This reduction could be due to a large linear expansion coefficient of YZO films in comparison with the glass substrate, to a reduction of defects, or to the desorption of oxygen.

The effects of annealing temperature on full width at half maximum (FWHM) of the films obtained from different solutions are shown in Figure 2. It was observed that FWHM decreases with increasing annealing temperature until 450 °C for all of the

films. The value of FWHM is inversely proportional to the grain size, implying that grain size improves with increasing annealing temperature [18]. A further increase in the annealing temperature resulted, however, in an increase in FWHM. This may be due to a degradation of the structure or contamination with alkali ions from the glass substrate [19]. The lowest FWHM, 0.39° , was obtained for films made from solution C, being 11.4% lower than that obtained from films made from solution A.

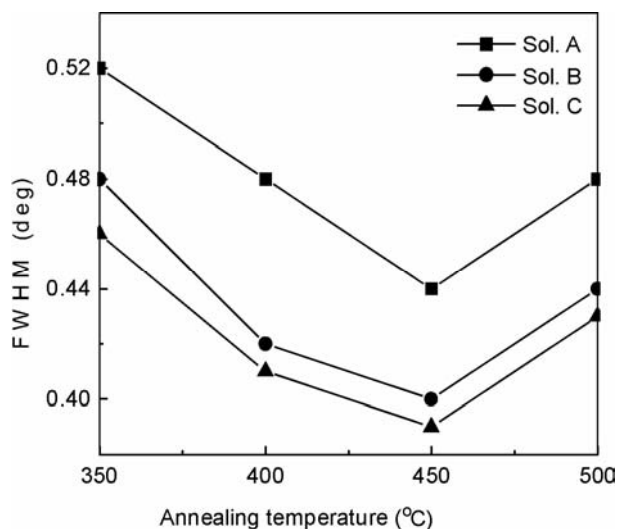


Fig. 2. The effect of annealing temperature on the FWHM of YZO films obtained from solutions A, B and C

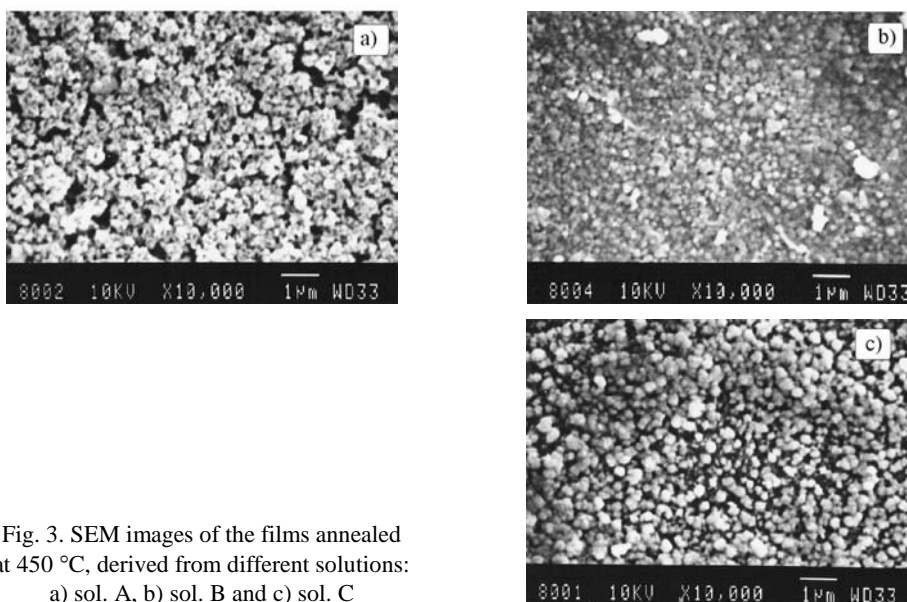


Fig. 3. SEM images of the films annealed at 450 °C, derived from different solutions: a) sol. A, b) sol. B and c) sol. C

The experiment reveals that the use of DEA enhances the *c*-axis orientation of YZO films. The solution with DEA as a stabilizer was the most stable and produced YZO films with the highest quality.

Figures 3a–c show SEM images of films annealed at 450 °C, derived from three different solutions. It can be clearly seen that the use of DEA enhances grain growth (supported by XRD analysis, Fig. 2) and improves surface morphology.

3.2. Electrical properties

The Hall coefficient data showed that the YZO films are of the n-type. Electrical properties of YZO films prepared from all three solutions were investigated as a function of annealing temperature. There was an increase in mobility with increasing annealing temperature until 450 °C, which is mainly due to the improvement of crystalline structure in films as supported by our XRD analysis (Fig. 2). This increase in mobility is also accompanied with an increase in the carrier concentration, due to interstitial zinc atoms and/or a contribution from Y³⁺ ions substituting Zn²⁺ ions. This results in a decrease in resistivity. Moreover, the desorption of oxygen from the surface, pores and grain boundaries with increasing annealing temperature may also be responsible for decreased resistivity. A slight increase in the resistivity of the films at temperatures above 450 °C may be due to a structural degradation as observed in the XRD analysis.

Table 1. FWHM, resistivity (ρ), carrier concentration (n) Hall mobility (μ_H) and average transmittance for YZO films grown at an optimized annealing temperature (450 °C) using different sol-gel stabilizers

Sol-gel stabilizers	FWHM (deg)	ρ ($\Omega\cdot\text{cm}$)	n (cm^{-3})	μ_H (cm^2/Vs)	Average transmittance (%)
Solution A	0.44	4.016	1.15×10^{17}	14.0	75
Solution B	0.40	0.246	1.39×10^{18}	18.2	79
Solution C	0.39	0.035	9.1×10^{18}	19.8	86

The resistivity (ρ), carrier concentration (n) and Hall mobility (μ_H) for the YZO films grown under optimized annealing temperature (450 °C) using different sol-gel stabilizers are given in Table 1. It is seen from the table that μ_H in a sample obtained from the solution C is nearly 1.4 times higher than that in a sample obtained from solution A, while there is an increase by two orders of magnitude in the value of n for films prepared from solution C as compared to those obtained from solution A. This gives rise to the lowest resistivity, $3.5 \times 10^{-2} \Omega\cdot\text{cm}$, for films obtained using DEA as a stabilizer.

3.3. Optical properties

Figure 4 shows optical transmittance curves for YZO films annealed at 450 °C, prepared from different solutions. The average transmittance in the visible region

measured for films obtained from all the three solutions was higher than 75%, but it was the highest for films produced from the solution C. The optical band gap energy was calculated using Tauc's plot, as shown in Fig. 5. The maximum values for transmittance and the band gap energy were obtained for films produced from solution C, amounting to 86% and 3.331 eV, respectively.

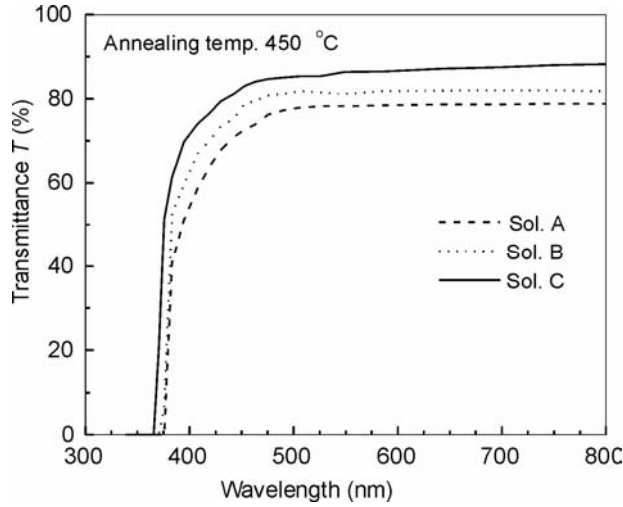


Fig. 4. The dependence of transmittance (T , %) in the wavelength range of 200–800 nm on sol-gel stabilizers for YZO films annealed at 450 °C

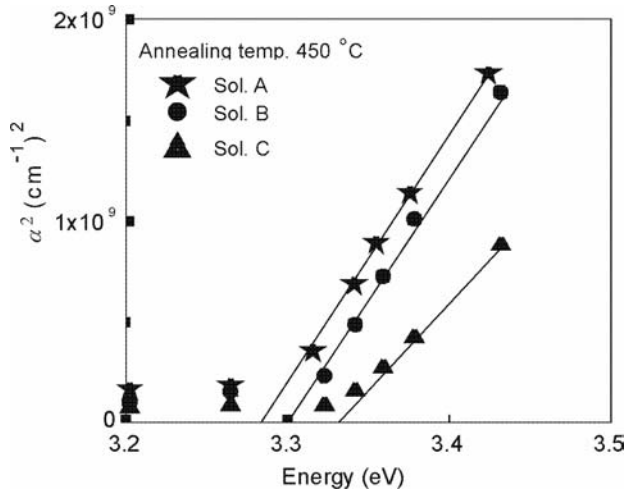


Fig. 5. Effect of sol-gel stabilizers on the band gap energy (E_g) for YZO films, shown in Tauc's plot

The effect of annealing temperature on the band gap energy of YZO films prepared from different solutions is shown in Fig. 6. It is seen from the figure that the

band gap energy is higher for films obtained from the solution C as compared to those obtained from the solutions A and B. The effect of annealing is also enhanced for films obtained from solutions using DEA as a stabilizer. The average transmittance was also found to increase with an increase in annealing temperature up to 450 °C for all three films. The variation of transmittance with annealing temperature for films deposited from the solution C is also shown in Figure 6. This increase in transmittance can be attributed to an improvement in the crystallinity and microstructure with increasing annealing temperature.

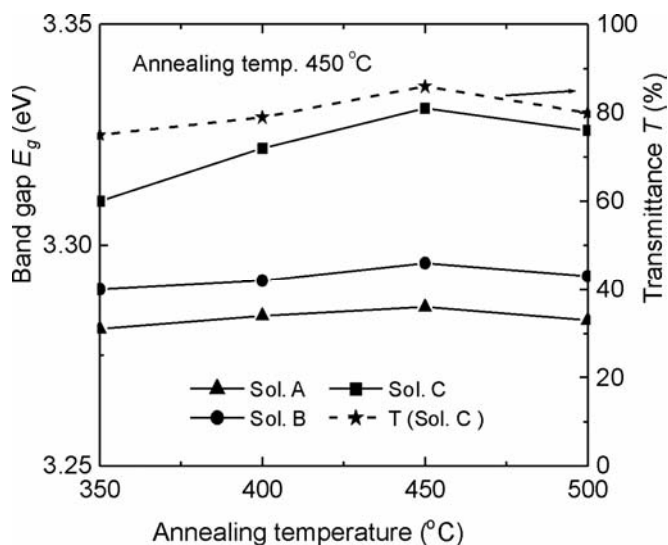


Fig. 6. Variation of band gap energy (E_g) and transmittance (T , %) as a function of annealing temperature

4. Conclusion

Sol-gel derived yttrium-doped ZnO thin films were obtained. They all exhibited polycrystallinity at an annealing temperature of 350 °C. It was observed that solutions with DEA as the stabilizer were the most stable and produced high-quality films. The crystalline quality of the films improved with increasing annealing temperature up to 450 °C. Films prepared from the solution C showed preferential *c*-axis orientation. Minimum resistivity and the maximum transmittance were obtained for films deposited from the solution C. These films also showed an enhanced optical band-gap energy.

It may be mentioned that the key to obtain high-quality films using the sol-gel technique is to prepare a clear, transparent and homogeneous solution without any chemical species. Further, in the sol-gel process of ZnO thin films starting from zinc acetate (the precursor material), one cannot use a hydrolysis reaction (as in alkoxides) in order to form Zn–O–Zn bonds in the precursor. The formation of such bonds al-

ways leads to a homogenous and/or heterogeneous nucleation of ZnO or other related compounds in the solution. When this happens, the solutions are not homogenous anymore. However, DEA acts as a bidentate ligand to the zinc ions in the solution, making it stable against any precipitates. This stability of the solution is responsible for the successful incorporation of Y into the ZnO lattice, in turn leading to reduced resistivity.

Acknowledgements

The authors wish to acknowledge the financial support of DRDO, Govt. of India, India.

References

- [1] PARAGUAY F., MIKI-YOSHIDA M., SOLIS J., ESTRADA W., *Thin Solid Films*, 373 (2000), 137.
- [2] HARTNAGEL H.L., DAWER A. L., JAIN A. K., JAGADISH C., *Semiconducting Transparent Thin Films*, Institute of Physics, Bristol, 1995.
- [3] COUTTS T.J., YOUNG D.L., LI X., *MRS Bull.*, 25 (2000), 56.
- [4] HU J., GORDON R. G., *J. Appl. Phys.*, 71 (1992), 880.
- [5] CHANG J.F., LIN W.C., HON M.H., *Appl. Surface Sci.*, 183 (2001), 18.
- [6] MINAMI T., SATO H., NANTO H., TAKATA S., *Jpn. J. Appl. Phys.*, 24 (1985) L 781.
- [7] TANG W., CAMERON D.C., *Thin Solid Films*, 238 (1994), 83.
- [8] MINAMI T., YAMAMOTO T., MIYATA T., *Thin Solid Films*, 366 (2000), 63.
- [9] MINAMI T., SATO H., TAKATA S., OGAWA N., MOURI T., *Jpn. J. Appl. Phys.*, 31 (1992), L 1106.
- [10] NAKADA T., OHKUBO Y., KUNIOKA A., *Jpn. J. Appl. Phys.*, 30 (1991), 3344.
- [11] GROENEN R., LOFFLER J., SOMMELING P. M., LINDEN J. L., HAMERS E.A.G., SCHROPP R.E.I, VAN DE SANDEN M.C.M., *Thin Solid Films*, 392 (2001), 226.
- [12] GOYAL D., SOLANKI P., MARANTHA B., TAKWALE M., BHIDE V., *Jpn. J. Appl. Phys.*, 31 (1992), 361.
- [13] HIRAMATSU M., IMAEDA K., HORIO N., NAWATA N., *J. Vac. Sci. Techn.*, A16 (1998) 669.
- [14] SINGH A. V., MEHRA R. M., YOSHIDA A., WAKAHARA A., *J. Appl. Phys.*, 90 (2001) 5661.
- [15] TSUCHIYA T., EMOTO T., SEI T., *J. Non-Cryst. Solids*, 178 (1994), 327.
- [16] ZNAIDI L., SOLER ILLIA G.J.A.A., BENYAHIA S., SANCHEZ C, KANAIEV A.V., *Thin Solid Films*, 428 (2003), 257.
- [17] TAKADA S., *J. Appl. Sci.*, 73 (1993), 4739.
- [18] AZAROFF L.V., *Elements of X-Ray Crystallography*, McGraw Hill, New York, 1968, p. 552.
- [19] VAN HEERDEN J.L., SWANPOEL R., *Thin Solid Films*, 299 (1997), 72.

Received 26 April 2004

Revised 25 June 2004

Analysis of optical transitions of Nd³⁺ in YAG nanocrystallites

ARTUR BEDNARKIEWICZ*

Institute of Low Temperature and Structure Research, Polish Academy of Sciences,
P.O. Box 1410, 50-950 Wrocław 2, Poland

A novel approach to the analysis of optical transitions in Nd³⁺-doped nanocrystallites is put forward, based on the Judd–Ofelt analysis of luminescence transitions associated with the ${}^4F_{3/2} \rightarrow {}^4I_{11/2}$ and ${}^4F_{3/2} \rightarrow {}^4I_{9/2}$ bands. The procedure, requiring neither information on Nd³⁺ concentration nor transparent samples, greatly simplifies calculation of branching ratios of neodymium ${}^4F_{3/2} \rightarrow {}^4I_J$. The technique seems to be very useful in the spectroscopic assessment of Nd³⁺-doped materials for laser and optoelectronic purposes. The effect of grain size in nanometric ceramics on the branching ratio is considered.

Key words: *nanometric ceramics, neodymium, spectroscopic parameter, Judd–Ofelt theory*

1. Introduction

Recently there has been a great interest in studying optical properties of rare-earth (RE) doped nanocrystals. These materials exhibit a number of novel interesting properties useful in designing new optoelectronic devices. Optical properties of RE doped nanocrystals depend on preparation conditions as well as on structural and morphological properties of individual particles. In particular, the processes of electronic relaxations are closely related to the size effect for very small nanoparticles (in the 1–30 nm range). This effect is associated with the electron-phonon confinement effect [1, 2] and may lead to inhomogeneous broadening of electronic transition linewidths, increased lifetimes and reduction of multiphonon relaxation and phonon-assisted energy transfer processes.

In the present paper, an analysis is performed of f-f transitions for Nd³⁺ doped YAG nanocrystals deduced from the luminescence spectra. The effect of nanocrystal grain sizes on optical properties of Nd:YAG was investigated.

*E-mail: Abednar@int.pan.wroc.pl.

The Judd–Ofelt model [3,4] allows quantitative analysis of the intensities of f-f radiative transition in RE doped crystals. The Judd–Ofelt theory was first developed for liquids and gases and then successfully used for glasses and crystals with numerous local site symmetries of active ions. Based on absorption spectra measurements, this method allows determining empirical parameters Ω_λ which in turn allow predicting the radiative rate constants for any f-f transitions. A direct application of Judd–Ofelt method in the analysis of the spectra of RE doped nanocrystalline powders is difficult because of lack of high quality absorption spectra due to scattering effects. There are, however, several approaches using luminescence spectra to enhance the accuracy of Ω_λ parameters determination for Pr^{3+} [5] or calculate spectroscopic quality parameters for Nd^{3+} or Er^{3+} .

In the case of Nd^{3+} ion, one of the most important for laser applications, two techniques have been described in the literature [7, 8]. Both are based on the assumption that the probability of spontaneous emission for various transitions ${}^4F_{3/2} \rightarrow {}^4I_J$ ($J = 15/2, 13/2, 11/2$ and $9/2$) is determined by the intensity parameters Ω_4 and Ω_6 only, whereas the Ω_2 parameter for which the matrix element $\langle U^{(2)} \rangle^2$ is close to 0, can be neglected. This allows to calculate the branching ratios $\beta_{JJ'}$ between ${}^4F_{3/2}$ and respective 4I_J ($J = 9/2, \dots, 15/2$) states of Nd^{3+} ion from the analytical expression

$$\beta_{JJ'}(X_{\text{Nd}}) = \frac{(a_{J'} X_{\text{Nd}} + b_{J'}) \lambda_{JJ'}^{-3}}{\sum_{J'} (a_{J'} X_{\text{Nd}} + b_{J'}) \lambda_{JJ'}^{-3}} \quad (1)$$

where $a_{J'} = \langle {}^4F_{3/2} \| U^{(4)} \| {}^4I_{J'} \rangle^2$ and $b_{J'} = \langle {}^4F_{3/2} \| U^{(6)} \| {}^4I_{J'} \rangle^2$ are matrix elements of the irreducible tensor operators of ranks 4 and 6, respectively. The spectroscopic quality parameter X_{Nd} is defined as

$$X_{\text{Nd}} = \frac{\Omega_4}{\Omega_6} \quad (2)$$

These dependencies are universal in their character and can be used to analyze Nd^{3+} doped glasses or other amorphous materials like ceramics, or even nontransparent media during the optimization process of its performance. Since only the Ω_4/Ω_6 ratio is necessary for calculations, relative band intensities are sufficient for determination of X_{Nd} . Moreover, there is no need to measure the concentrations of Nd^{3+} ions, which greatly simplifies the calculation procedure. The first method is applied for absorption bands, namely the relations between the ${}^4I_{9/2} \rightarrow {}^2P_{1/2}$ and ${}^4I_{9/2} \rightarrow {}^4I_{15/2}$ or ${}^4I_{9/2} \rightarrow {}^4I_{9/2}$ transitions are required [7]. This procedure may be used only for transparent or at least semitransparent media. For nontransparent media or for the samples not suitable for absorption measurements, scattering or fluorescence spectra may be used. The relation between the ${}^4F_{3/2} \rightarrow {}^4I_{11/2}$ and ${}^4F_{3/2} \rightarrow {}^4I_{13/2}$ luminescence bands is also used

to estimate X_{Nd} value [9]. Due to the fact that the ${}^4\text{F}_{3/2} \rightarrow {}^4\text{I}_{11/2}$ transition is located around 1.06 μm and the ${}^4\text{F}_{3/2} \rightarrow {}^4\text{I}_{13/2}$ is located around 1.35 μm , obtaining real values of the relative band intensities may prove difficult as most photodetectors does not cover both regions simultaneously. The method put forward in the present paper allows calculating spectroscopic parameters of Nd³⁺ ion by comparing luminescence intensities of two other bands.

2. Experimental

In the course of the experiments one single crystal and a series of nanometric Y₃Al₅O₁₂ (YAG) powders were measured. They were 1 at. % Nd:Y₃Al₅O₁₂ single crystal and 5.4 at. % Nd:YAG nanocrystals heated at 800, 100 and 1200 °C (the same material as in [6]), respectively.

All the spectra were recorded in the same conditions with a JobinYvon THR1000 1 meter spectrophotometer. A Hamamatsu photomultiplier with R406 characteristics was used together with a 1200 holographic grating. All spectra were corrected for spectral responsivity of the system, by dividing acquired data by a calibrating curve. The calibrating curve was obtained from black-body emissivity taking into account Planck law for a specific black-body temperature and acquisition equipment parameters.

3. Results and discussion

Due to a relatively high intensity and ease of measurement in near the IR range, it is proposed that the relation between two bands: ${}^4\text{F}_{3/2} \rightarrow {}^4\text{I}_{11/2}$ at 9447 cm⁻¹ (hereafter referred to as γ_1) and ${}^4\text{F}_{3/2} \rightarrow {}^4\text{I}_{9/2}$ around 11500cm⁻¹ (γ_2) may be used to calculate the spectroscopic parameter of neodymium ion. As a matter of fact, $U^{(2)}$ matrix element may be taken equal to zero for all transitions under consideration.

The intensity of luminescence may be expressed as $I = AN_2hc\tilde{\nu}$ where A is a spontaneous emission coefficient, N_2 is a population of emitting level and $hc\tilde{\nu}$ is the energy of a transition. Dividing I_{γ_1} by I_{γ_2} allows employing the above relation and relation (2) to construct an analytical expression

$$\frac{I_{\gamma_1}}{I_{\gamma_2}} = \frac{\bar{\nu}_{\gamma_1}}{\bar{\nu}_{\gamma_2}} \cdot \frac{A_{\gamma_1}}{A_{\gamma_2}} = \frac{\bar{\nu}_{\gamma_1}}{\bar{\nu}_{\gamma_2}} \cdot \left(\frac{\bar{\nu}_{\gamma_1}}{\bar{\nu}_{\gamma_2}} \right)^3 \cdot \frac{\chi_{\gamma_1}}{\chi_{\gamma_2}} \cdot \frac{\langle \|U_{\gamma_1}^{(4)}\| \rangle^2 X_{\text{Nd}} + \langle \|U_{\gamma_1}^{(6)}\| \rangle^2}{\langle \|U_{\gamma_2}^{(4)}\| \rangle^2 X_{\text{Nd}} + \langle \|U_{\gamma_2}^{(6)}\| \rangle^2} \quad (3)$$

Here I_{γ_1} and I_{γ_2} are intensities of the γ_1 and γ_2 bands respectively, $\bar{\nu}_{\gamma_1}$ and $\bar{\nu}_{\gamma_2}$ are wave numbers of the γ_1 and γ_2 transitions, respectively, χ_{γ_1} and χ_{γ_2} are local field cor-

rection factors for electric-dipole transitions of luminescence spectra where χ_i is defined as

$$\chi_i = \frac{n_i (n_i^2 + 2)^2}{9} \quad (4)$$

n_i describing the index of refraction for a given transition.

Table 1. Matrix elements for ${}^4F_{3/2} \rightarrow {}^4I_{11/2}$ and ${}^4F_{3/2} \rightarrow {}^4I_{9/2}$ transitions [10]

γ	Transition	$\Delta \bar{\nu}$ [cm ⁻¹]	$\langle \ U^{(2)}\ \rangle^2$	$\langle \ U^{(4)}\ \rangle^2$	$\langle \ U^{(6)}\ \rangle^2$
γ_1	${}^4F_{3/2} \rightarrow {}^4I_{11/2}^1$	9500	0.0000	0.1136	0.4104
γ_2	${}^4F_{3/2} \rightarrow {}^4I_{9/2}^2$	11350	0.0000	0.2293	0.0548

¹Despite ${}^4F_{3/2} \rightarrow {}^4I_{11/2}$ also ${}^2K_{15/2} \rightarrow {}^4F_{3/2}$ could influence the transition around 9550 nm but the 514.5 nm excitation line does not excite the ${}^2K_{15/2}$ level.

² $U^{(2)}$ parameter was rejected. Transitions not excited by 514.5 nm line where not considered.

Denoting

$$I_r = \frac{I_{\gamma_1}}{I_{\gamma_2}} \left(\frac{\bar{\nu}_{\gamma_2}}{\bar{\nu}_{\gamma_1}} \right)^4 \frac{\chi_{\gamma_2}}{\chi_{\gamma_1}} \quad (5)$$

and recasting Eq. (3), one gets

$$X_{Nd} = \frac{\langle \|U_{\gamma_1}^{(6)}\| \rangle^2 - I_r \langle \|U_{\gamma_2}^{(6)}\| \rangle^2}{I_r \langle \|U_{\gamma_2}^{(4)}\| \rangle^2 - \langle \|U_{\gamma_1}^{(4)}\| \rangle^2} \quad (6)$$

According to Table 1, $\langle \|U_{\gamma_1}^{(4)}\| \rangle^2 = 0.1136$, $\langle \|U_{\gamma_1}^{(6)}\| \rangle^2 = 0.4104$. For the γ_2 transition $\langle \|U_{\gamma_2}^{(4)}\| \rangle^2 = 0.2293$ and $\langle \|U_{\gamma_2}^{(6)}\| \rangle^2 = 0.0548$.

Preliminary calculations have shown that the value of the X_{Nd} parameter obtained with Eq. (6) is larger than that obtained from the Ω_λ parameters calculated from absorption spectra, e.g. $X_{Nd} = 2.00$ versus 0.54 for Nd:YAG single crystal. It is expected that a quantitative X_{Nd} calculation would need a correction factor, specific for a given experimental setup. Once defined, it could be used to correct X_{Nd} for any other material. The correction factor was derived as a ratio of absorption-based to emission-based values of the spectroscopic parameters, e.g. $0.54/2.004 = 0.2695$ hence $X'_{Nd} = 0.2695X_{Nd}$. It is obvious that the correction factor is sensitive to any kind of changes done to the setup. Nevertheless, qualitative conclusions about X_{Nd} obtained from luminescence spectra can be drawn.

Assuming $\bar{\nu}_{\gamma_1} = 9450 \text{ cm}^{-1}$ and $\bar{\nu}_{\gamma_2} = 11500 \text{ cm}^{-1}$ from the dispersion characteristics of YAG one obtains $n_{\gamma_1} = 1.818$ and $n_{\gamma_2} = 1.822$. In fact, the barycenter of the band in calculations (Eq. (5)) was evaluated by means of the expression

$$\bar{\lambda} = \frac{\int \lambda \varepsilon(\lambda)}{\int \varepsilon(\lambda)} \quad (7)$$

and then recalculated to wavenumbers. $\varepsilon(\lambda)$ represents the emission spectrum.

According to Eq. (3), a spontaneous emission is required, what implies the use of low pumping power, far from stimulated emission condition or any thermalization effects. These effects, which may change proportions between respective emission bands, are undesired.

Table 2. Calculated Nd³⁺ spectroscopic parameters and branching ratios β_j of respective ${}^4F_{3/2} \rightarrow {}^4I_j$ transitions for different materials¹

Material	Ω_2	Ω_4	Ω_6	X_{Nd}	X'_{Nd}	$\beta_{15/2}$	$\beta_{13/2}$	$\beta_{11/2}$	$\beta_{9/2}$	Ref.
	[10 ⁻²⁰ cm ²]									
YAG single crystal	0.20	2.70	5.00	0.540		0.6	11.6	53.4	34.4	[11]
	0.37	2.29	5.97	0.384		0.7	12.7	56.4	30.2	[12]
	1.00	2.90	9.30	0.312		0.7	13.3	58.0	28.0	[13]
	0.00	3.20	4.60	0.696		0.5	10.7	50.8	38.0	[14]
	0.34	2.11	5.48	0.385		0.7	12.7	56.3	30.3	[15]
	0.35	2.36	13.02	0.181		0.8	14.6	61.3	23.4	[16]
	–	–	–	2.004	0.461	0.6	12.1	54.8	32.4	²
(nc)YAG 800 °C	–	–	–	2.352	0.541	0.6	11.6	53.3	34.5	[6] ²
(nc)YAG 1000 °C	–	–	–	2.081	0.479	0.6	12.0	54.5	32.9	
(nc)YAG 1400 °C	–	–	–	1.649	0.379	0.7	12.8	56.5	30.1	

¹(X_{Nd} from Ω parameters if given in the Table or from luminescence spectra, X'_{Nd} with correction factor from luminescence spectra).

² X_{Nd} calculated from luminescence spectra in present work, other X_{Nd} parameters were obtained from Eq. (2) basing on literature data.

It is interesting to note that literature data of X_{Nd} are very divergent varying from 0.2 up to 0.7. It comes from Eq. (1) that for $X_{\text{Nd}} > 2$ even large changes in X_{Nd} result in small changes in branching ratios. The error can be here estimated by the total differential equation for every parameter of Eqs. (4)–(6). The equation

$$\Delta X_{\text{Nd}} = \sum_{P=I_{\gamma_1}, I_{\gamma_2}, \nu_{\gamma_1}, \nu_{\gamma_2}, n_{\gamma_1}, n_{\gamma_2}} \frac{\delta X_{\text{Nd}}}{\delta P} \Delta P \quad (8)$$

was used to calculate absolute error with I , ν and n of both γ_1 and γ_2 bands as parameters. Here ΔP is the measurement error of, e.g., ΔI_{γ_i} , $\Delta \nu_{\gamma_i}$ and Δn_{γ_i} equal to 5, 10 and 0.01, respectively. The total relative error $(\Delta X_{\text{Nd}}/X_{\text{Nd}}) \times 100\%$ was calculated to be

20.2, 29.3 and 35.3% for samples heated at 800, 1000 and 1400 °C, and for X_{Nd} given in Table 2. The increase in the total relative error may be due to the decrease of X_{Nd} value. It is important to notice, however, that for $X_{\text{Nd}} > 2$, even large X_{Nd} changes do not introduce large changes of β_J values. For the samples examined in this work, for higher annealing temperatures, the spectroscopic parameter X_{Nd} systematically decreases due to increasing sizes of YAG grains [6]. The average grain sizes for YAG nanocrystals were 25, 100 and 2000 nm for the samples heated at 800, 100 and 1200 °C, respectively.

4. Conclusions

It was found that the observed trend of increasing X_{Nd} with increasing temperature of annealing of nanocrystallite ceramics is due to the increase of the grain size of nanocrystallites. The reason why the grain size affects the spectroscopic parameter is not clear at the moment. It is obvious that the grain size affects the luminescence spectrum due to thermalisation of the ${}^4\text{F}_{5/2}$ state from ${}^4\text{F}_{3/2}$. The thermalisation should affect the ${}^4\text{F}_{3/2}$ level emission in the same way, thus it should not change the relation between the bands resulting from emission from that level to different ${}^4\text{I}_J$ levels. Most probably, the thermalisation of the ground state states ${}^4\text{I}_J$ and the Stark levels within that states change the statistical distribution of electrons.

The method presented in this paper does not include cross relaxation processes responsible for concentration quenching in Nd^{3+} doped samples. The cross-relaxation reduces the total population of ${}^4\text{F}_{3/2}$ state but does not change the branching ratio distribution. Use of a low pumping power may eliminate the parasitical process considered.

The advantage of the presented method is a possibility of using fluorescence instead of absorption spectra. This simplifies the calculation method of the branching ratio eliminating necessity of the preparation of proper sample surfaces and making unnecessary knowledge of active ions concentration. Moreover, spectroscopic properties of non- or semi-transparent materials may now be easily assessed.

Acknowledgements

The YAG nanoceramics were synthesized by Dr Dariusz Hreniak (Institute of Low Temperature and Structure Research, Polish Academy of Sciences, Wrocław). The author appreciates discussions with Professor Renata Reinfeld and Professor Wieslaw Strek. The author is a Foundation for Polish Science scholarship holder.

References

- [1] MALYUKIN YU.V., MASALOV A.A., ZHMURIN P.N., Phys. Lett., A 316 (2003), 147.
- [2] LIU G.H., CHEN X.Y., ZHUANG H.Z., LI S., NIEDBALA R.S., J. Solid State Chem., 171 (2003), 123.
- [3] JUDD B.R., Phys. Rev., 127 (1962), 750.

- [4] OFELT G.S., J. Chem. Phys., 37 (1962), 511.
- [5] QUIMBY R.S., MINISCALCO W.J., J. Appl. Phys., 75, (1994), 613.
- [6] HRENIAK D., STREK W., J. Alloys Cpds., 341 (2002), 183.
- [7] KAMINSKII A.A., LI L., Phys. Stat. Sol. (a), 26 (1974), 593.
- [8] KAMINSKI A.A., *Crystalline lasers: Physical Processes and Operating Schemes*, CRC Press, Boca Raton, 1996.
- [9] LOMHEIM T.S., DESHAZER L.G., Opt. Commun., 24 (1978), 89.
- [10] CARNALL W.T., CROSSWHITE H., CROSSWHITE H.M., *Energy Level Structure and Transition Probabilities of the Trivalent Lanthanides in LaF₃*, Argonne, Illinois, 1977.
- [11] KRUPKE W.F., IEEE J. Quantum El., 7 (1971), 153.
- [12] KAMINSKII A.A., LI L., Phys. Stat. Sol. (a), 26 (1974), K21.
- [13] DEB K.K., BUSER R.G., MORRISON C.A., LEAVITT R.P., J. Opt. Soc. Am., 71 (1981), 1463.
- [14] KNOWLES D., CASSANHO A., JENSSEN H.P., [in:] M.K. Shand, H.P. Jenssen (Eds.), *Tunable Solid State Lasers*, OSA, Washington, D.C., 1989, p. 139.
- [15] KAMINSKII A.A., MIRONOV V.S., BAGAEV S.N., Kvantovaya Elektron. (Moscow), 21 (1994), 711.
- [16] ALLIK T.H., MORRISON C.A., GRUBER J.B., KOKTA M.R., Phys.Rev., B41 (1990), 21.

Received 17 April 2004

Revised 29 June 2004

Synthesis and luminescence properties of nanocrystalline $\text{BaTiO}_3:\text{Nd}^{3+}$ obtained by sol-gel methods

ROBERT PAZIK*, DARIUSZ HRENIAK, WIESŁAW STRĘK

Institute of Low Temperature and Structure Research, Polish Academy of Sciences,
P.O. Box 1410, 50-950 Wrocław 2, Poland

Neodymium-doped barium titanate (BaTiO_3) nanocrystalline powders were prepared by the sol-gel method. Structure and average grain sizes were analysed by X-ray powder diffraction (XRD) measurements. Grain sizes amount from 30 to 60 nm, depending on dopant concentration and sintering temperature. The luminescence properties of $\text{BaTiO}_3:\text{Nd}^{3+}$ were investigated as a function of the concentration of Nd^{3+} (0.5–2 mol %) and sintering temperature (700–1050 °C). The influence of Nd^{3+} concentration on the grain size and crystal structure of BaTiO_3 nanocrystallite powders was found and a weak hot emission from the ${}^4\text{F}_{5/2}$ level was observed for the nanopowders obtained.

Key words: *barium titanate; neodymium; sol-gel; luminescence; size effect*

1. Introduction

Barium titanate (BaTiO_3), a classical ferroelectric material belonging to a numerous group of perovskite materials, is characterized by a general formula ABO_3 . Depending on the valencies of the metal cations (A and B), perovskite materials are subdivided into two main groups, described by the formulas $\text{A}^{2+}\text{B}^{4+}\text{O}_3$ (e.g. BaTiO_3 , PbTiO_3) and $\text{A}^{3+}\text{B}^{3+}\text{O}_3$ (e.g. NdAlO_3 , LaAlO_3). In both groups the crystal structure is usually depicted in a pseudocubic form. It contains two cation sites in the crystal lattice: (A) large cations located in the corners, (B) small cations occupying the centre of the unit cell, and oxygen ions on the centres of the cell walls. Possible displacement in ion arrangement in the unit cell is directly responsible for characteristic properties of these materials [1, 2].

* Corresponding author, e-mail: R.Pazik@int.pan.wroc.pl.

Recent developments in nanotechnology create new and interesting challenges for researchers and opens broader fields of practical applications of nanomaterials. One of many methods for obtaining such materials [3–7] is the sol-gel technique [8]. The sol-gel method for obtaining nanocrystalline particles of BaTiO₃ is relatively simple and easy to carry out. Furthermore, this method has a few important advantages in comparison to the conventional solid state method (SSM) [9]. The sol-gel route is less expensive (temperatures lower than 1000 °C), enables a high concentration of dopant to be introduced, and assures a better control of reaction conditions such as pH or temperature.

Grain size of the nanocrystalline barium titanate strongly influences its structure and ferroelectric properties. Therefore, size effects in nanoparticles of BaTiO₃ have been the subject of many studies [10–17]. A hypothesis on a critical size above 50 nm for the existence of ferroelectric properties has been put forward by Frey and Payne [14]. Moreover, Uchino [15] and Saegusa [16] found the tetragonal phase, responsible for the ferroelectricity, disappear at grain sizes below 100 nm. In our previous studies, the stabilization and enhancement of the tetragonal structure with increasing europium ion concentration in BaTiO₃ has been reported. A strong size dependence of the luminescence properties of Eu³⁺ has been shown as well [8, 17].

In this work, we present results of preparation and characterization of Nd³⁺-doped BaTiO₃, obtained via the sol-gel method. The main aim of our work was to investigate luminescence properties (spectra, decay times) of BaTiO₃ nanocrystalline powders in terms of the size dependence effect, obtained at sintering temperatures in the range of 700–1200 °C and doped with neodymium ions of various concentrations. We have also studied the influence of grain size on the hot emission from the ⁴F_{5/2} level and the effect of doping with Nd³⁺ on the crystal structure of BaTiO₃ nanopowders.

2. Experimental

Details concerning the preparation of BaTiO₃ nanocrystallites have been described by us elsewhere [17]. Barium acetate, titanium butoxide and neodymium oxide were used as starting materials. Acetylacetone and acetic acid were selected as solvents for titanium butoxide and barium acetate, respectively. Neodymium chloride was obtained by reacting stoichiometric amounts of neodymium oxide with hydrochloric acid. Dissolved barium acetate was added dropwise to titanium butoxide solution while stirring. The obtained solutions were vigorously stirred at 50 °C for about 2 h. The neodymium salt was dissolved in a small amount of water and added slowly to the obtained transparent yellow sol with different molar ratios of Nd³⁺ to BaTiO₃. The sols obtained were heated at approximately 100 °C for 24 h to form barium titanate gels. The samples of crushed gels were heated above 700 °C to form nanocrystalline BaTiO₃ powders doped with Nd³⁺.

3. Results and discussion

3.1. XRD analysis

Samples of BaTiO_3 doped with Nd^{3+} ions of different concentrations and sintered at 700–1100 °C were characterized by X-ray diffraction. The XRD patterns of BaTiO_3 powders doped with Nd^{3+} ions of various concentrations are presented in Fig. 1. Peaks shown in the patterns are sharp and well defined, indicating that all samples are well crystallized. The patterns were compared to the reference standard cards for tetragonal and cubic BaTiO_3 [18, 19]. The average size of crystallites, estimated from the broadening of diffraction peak using the Scherrer equation [20], varies from 30 to 55 nm depending on sintering temperature and dopant concentration (Fig. 2).

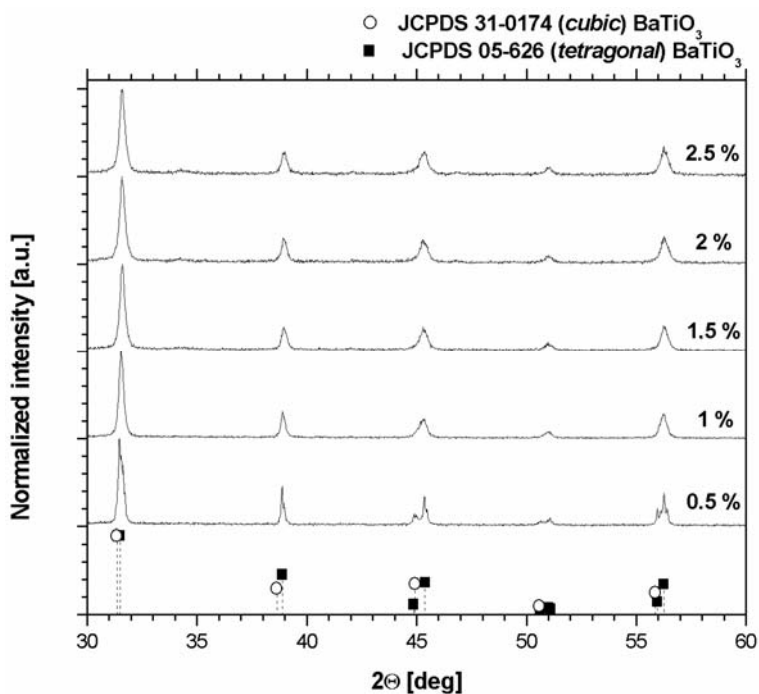


Fig. 1. XRD patterns of the BaTiO_3 powder samples doped with Nd^{3+} of various concentrations

An analysis of the XRD patterns for samples with different neodymium ion concentrations (0.5–2%) and heated at 1050 °C showed that all samples, except the one with 0.5% Nd, were in the cubic phase characteristic of paraelectric BaTiO_3 . Furthermore, we observed a dependence of the dopant concentration on the grain size, which has also been reported by Buscaglia [2] and Tsur [21]. It is well known that the dopant ionic radius is a main parameter determining the substitutions in the BaTiO_3

crystal lattice. Thus, Nd^{3+} ions (1.08 \AA) are mainly placed at Ba^{2+} sites (1.35 \AA) and not at Ti^{4+} ones (0.68 \AA), due to the size incompatibility. Increasing dopant concentration causes an overall shrinkage of the BaTiO_3 unit cell, changing lattice parameters and resulting in a change of the crystal structure.

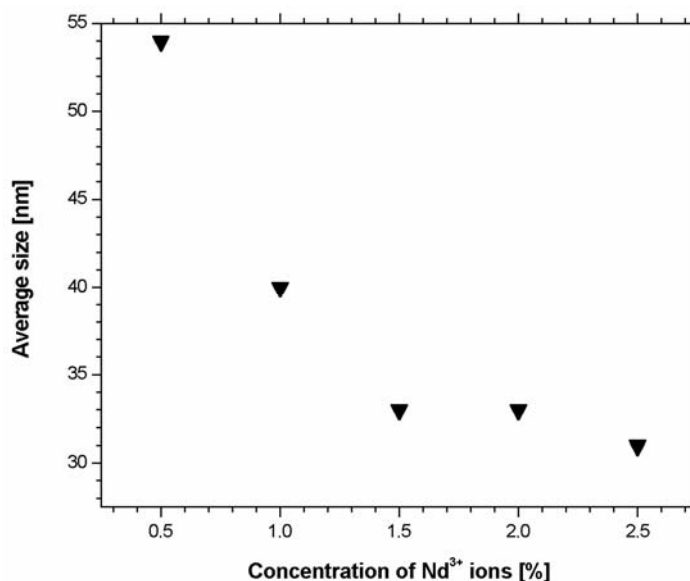


Fig. 2. Effect of dopant concentration on the average size of $\text{BaTiO}_3:\text{Nd}^{3+}$ crystallites

In nanosized grains, effects resulting from a progressive decrease of particle size are more pronounced. Many authors, when considering the size effect on the structure and ferroelectric properties of BaTiO_3 , emphasized importance of grain size, responsible for new phenomena occurring in nanostructured materials in comparison to their equivalents composed of larger crystallites [14, 22, 23]. Thus, increasing concentration of Nd^{3+} ions causes a decrease in grain sizes (from 54 nm for 0.5% of Nd^{3+} to 30 nm for 2.5%) up to a boundary value of dopant concentration (1.5% of Nd^{3+}). Above that value there is no further decrease of the grain size. Moreover, the shrinkage of the unit cell and decrease in a grain size causes additional changes in the crystal structure. An analysis of the diffraction peak around $2\theta \approx 45^\circ$ for the sample doped with 0.5% of Nd^{3+} showed its splitting into a doublet ascribed to 200 and 002 peaks, characteristic of the tetragonal phase of BaTiO_3 . Samples with the concentration of Nd^{3+} ions exceeding 1% are characterized by the paraelectric cubic crystal structure. This is quite different from our previous results. We have proved that the incorporation of Eu^{3+} ions into the barium titanate crystal causes a significant increase of the sample tetragonality [8]. Such behaviour is probably caused by the existence of europium of two different valencies in the crystal structure: larger Eu^{2+} ion will be placed at Ba^{2+} sites, whereas smaller Eu^{3+} enters Ti^{4+} or Ba^{2+} sites.

3.2. Emission spectra and discussion

The emission spectra of barium titanate nanocrystallites doped with neodymium ions at various concentrations (0.5–2 mol % vs. BaTiO₃) and heat-treated at temperatures in the range 700–1050 °C, were measured at room temperature. They are shown in Fig 3a. All spectra consist of characteristic bands, ascribed to the ${}^4F_{3/2} \rightarrow {}^4I_J$ ($J = 11/2, 9/2$) electronic transitions of Nd³⁺ ions, according to the established energetic model [24]. The band with a maximum at 876 nm corresponds to the ${}^4F_{3/2} \rightarrow {}^4I_{11/2}$ transition, and the one at 1064 nm to the ${}^4F_{3/2} \rightarrow {}^4I_{9/2}$ transition. Additionally, a weak emission corresponding to the (${}^4F_{5/2}, {}^2H_{9/2}$) \rightarrow ${}^4I_{9/2}$ transitions (Fig. 3b) was observed. The hot emission from ${}^4F_{5/2}$ and ${}^2H_{9/2}$ levels takes place during an excessive self-heating of samples due to the scattering of optical excitation energy in individual nanocrystals. This explains the increase of intensity under increasing excitation power [25]. Thus, higher-lying levels were populated at the cost of desired laser emission from the metastable ${}^4F_{3/2}$ level.

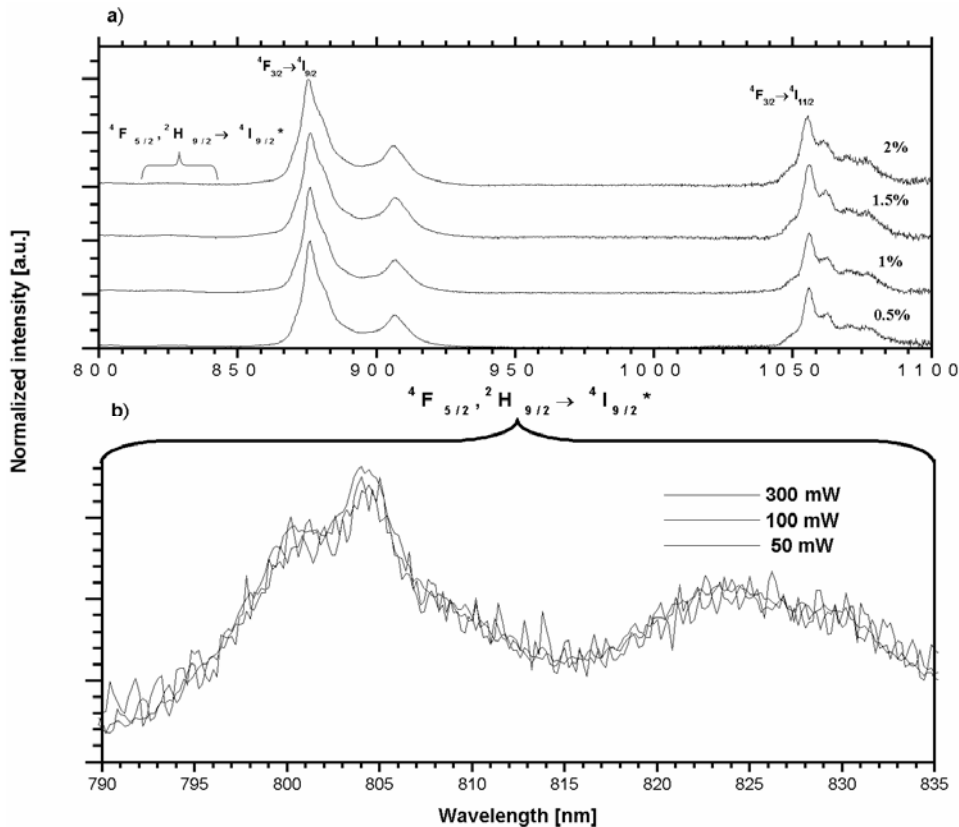


Fig. 3. Emission spectra of BaTiO₃:Nd³⁺: a) with different concentrations of Nd³⁺, b) hot emission from (${}^4F_{5/2}, {}^2H_{9/2}$) to the ${}^4I_{9/2}$ level

We performed measurements of power-dependent emission as a function of the average size of $\text{BaTiO}_3:\text{Nd}^{3+}$ grains. No increase of the hot-emission intensity with increasing excitation power was observed. This indicates that the particles of nanocrystallite BaTiO_3 warmed up only slightly. The aggregation of grains, facilitating escape of the excess heat from the sample, favourable luminescence properties and a weak hot emission make Nd^{3+} doped BaTiO_3 a promising material for use in thin layers.

4. Conclusion

BaTiO_3 nanocrystals were obtained via the sol-gel route. The structure and average size of BaTiO_3 nanocrystallites were determined. The average size ranged between 30 and 60 nm, depending on the dopant concentration and sintering temperature. The influence of dopant concentration on the grain size and crystal structure of BaTiO_3 was established. Crystallites in samples with low concentrations of Nd^{3+} ions are larger than those in highly doped samples (over 1% of Nd^{3+}). The former ones have the tetragonal ferroelectric crystal structure in contrast to the latter ones, crystallizing in the cubic paraelectric phase. Moreover, selecting a specific type of dopant enables nanocrystallite powders of BaTiO_3 with a desired crystal structure to be obtained. In this way, properties of the final product can be controlled (ferroelectric or paraelectric state). By controlling the dopant concentration, the sizes of nanocrystallites can be minimized. The luminescence properties of Nd^{3+} were investigated as a function of the thermal treatment, concentration and excitation power. Weak emission from the ${}^4\text{F}_{5/2} \rightarrow {}^4\text{I}_{9/2}$ has been observed due to a slight thermal self-heating of BaTiO_3 nanopowders.

References

- [1] SCHWARTZ R.W., *Chem. Mater.*, 9 (1997), 2325.
- [2] BUSCAGLIA M.T., BUSCAGLIA V., VIVIANI M., NANNI P., HANUSKOVA M., *J. Eur. Ceram. Soc.*, 20 (2000), 1997.
- [3] ANURADHA T.V., RANGANATHAN S., MIMANI T., PATIL K.C., *Scripta Mater.*, 44 (2001), 2237.
- [4] PECHINI M., US Patent No. 3,330,697 (1967).
- [5] HU M. Z.-C., KURIAN V., PAYZANT E.A., RAWN C.J., HUNT R.D., *Powder Tech.*, 110 (2000), 2.
- [6] HER Y.-S., LEE S.-H., MATIJEVIĆ E., *J. Mater. Res.*, 11 (1996), 156.
- [7] LI S., EASTMAN J.A., THOMPSON L.J., BJORMANDER C., FOSTER C.M., *Mater. Res. Soc. Symp. Proc.*, 457 (1997), 45.
- [8] STREK W., HRENIAK D., BOULON G., GUYOT Y., PAZIK R., *Optical Mater.*, 24 (2003), 15.
- [9] PARK Y., KIM C.I., Korean Patent No. 91-11699 (1991).
- [10] ZHANG M.-S., YU J., CHEN W., YIN Z., *Progress Cryst. Growth Charact. Mat.*, 40 (2000), 33.
- [11] SHIH W.-H., LU Q., *Ferroelectrics*, 154 (1994), 71.
- [12] SHIH W.Y., SHIH W.-H., AKSAY I.A., *Phys. Rev. B*, 50 (1994), 575.
- [13] MCNEAL M.P., JANG S.-J., NEWNHAM R.E., *J. Appl. Phys.*, 83 (1998), 3288.
- [14] FREY M.H., PAYNE D.A., *Phys. Rev. B*, 54 (1996), 3158.

- [15] UCHINO K., SDANAGA F., HIROSE T., J. Am. Ceram. Soc., 72 (1989), 1555.
- [16] SAEGUSA K, WENDELL E.R., BOWEN H.K, J. Am. Ceram. Soc., 76 (1993), 1505.
- [17] HRENIAK D, ŁUKOWIAK E., MARUSZEWSKI K., PAZIK R., STREK W., Mater. Sci., 20 (2002), 43.
- [18] *JCPDS Powder Diffraction file Card No. 05-526*, International Center for Diffraction Data, Newtown Square, PA, (1967).
- [19] *JCPDS Powder Diffraction file Card No. 31-0174*, International Center for Diffraction Data, Newtown Square, PA, (1967).
- [20] KLUG P., ALEXANDER L.E., X-ray Diffraction Procedure, New York, Wiley, 1954 Chap. 9.
- [21] TSUR Y., DUNBAR T.D., RANDALL C.A., J. Electroceram., 7 (2000), 25.
- [22] TAKEUCHI T., TABUCHI M., ADO K., HONJO K., NAKAMURA O., KAGEYAMA H., SUYAMA Y., OHTORI N., NAGASAWA M., J. Mater. Sci., 32 (1997), 4053.
- [23] CHO W.S., J. Phys. Chem. Solids, 59 (1998), 659.
- [24] CARNALL W.T., CROSSWHITE H., CROSSWHITE M., *Energy level structure and transition probabilities of the trivalent lanthanides in LaF₃*, Argonne, National Laboratory, Illinois, 1975.
- [25] HRENIAK D., STREK W., J. Alloys Comp., 341 (2002), 183.

Received 8 April 2004

Revised 16 July 2004

Optical properties of Eu(III) doped nanocrystalline films of TiO₂

AGNIESZKA HRENIAK^{1*}, MARCIN NYK², DARIUSZ HRENIAK³, WIESŁAW STRĘK³,
LESZEK KĘPIŃSKI³, JAN MISIEWICZ², KRZYSZTOF MARUSZEWSKI^{1,3}

¹Faculty of Mechanical Engineering, Institute of Materials Science and Applied Mechanics,
Wrocław University of Technology, Wybrzeże Wyspiańskiego 27, 50-370 Wrocław, Poland

²Institute of Physics, Wrocław University of Technology,
Wybrzeże Wyspiańskiego 27, 50-370 Wrocław, Poland

³Institute of Low Temperature and Structure Research, Polish Academy of Sciences,
P.O. Box 1410, 50-950 Wrocław 2, Poland

The synthesis of europium (III) doped nanocrystalline TiO₂ films is described. The morphology and structure of the films were determined by transmission electron microscopy (TEM) and the selected area of electron diffraction (SAED) method. The photoluminescence (PL), lifetimes and cathodoluminescence (CL), recorded at room temperature, are reported. It has been found that the cathodoluminescence characteristics are significantly different from the photoluminescence ones. It is concluded that different Eu³⁺ sites contribute to the optical behaviour of Eu³⁺:TiO₂ films.

1. Introduction

Thin films of luminescent materials have been intensively investigated due to their applications in FED [1, 2], organic and inorganic electroluminescent films [3–6], planar waveguides [7, 8] optical sensors [9] and lasers [10, 11]. These layered materials can be obtained by various methods, depending on the type of materials and future applications. Chemical vapour deposition (CVD) [12], ion and magnetron sputtering [13], and laser ablation [14] are examples of such methods. However, the most often used and relatively cheapest method of obtaining thin films is the sol-gel technique. The sol-gel process involves the formation of sols from precursors and the transformation of these sols first into wet gels and finally (after drying) to xerogels [4]. This technique enables high concentrations of well-dispersed solute molecules (a feature

*Corresponding author: hreniak@immt.pwr.wroc.pl.

typical of solutions) in rigid structures of xerogels to be obtained. Sol-gel films of different thickness are usually produced in two ways: by the dip-coating [5] or spin-coating [6] techniques. The main problems in the preparation of good quality sol-gel films are: the risk of cracking resulting from the shrinkage of gels during drying and the misfit thermal expansion coefficients between the substrate and layer [7]. One of the possible remedies for these problems is to adjust the sol viscosity which affects the layer thickness. It is well known that the risk of cracking during drying is smaller for thinner layers [8].

This work presents a preparation method, and structural and spectroscopic studies of TiO₂ sol-gel films doped with lanthanide ions, used as high-refractivity material for planar waveguide systems. The Eu³⁺ ions were chosen as emitting dopants due to their favourable luminescence properties in the visible region.

2. Experimental

2.1. Apparatus

Photoluminescence (PL) spectra were recorded using a Jobin-Yvon TRW 1000 spectrophotometer and a photomultiplier (Hamamatsu R928). In order to record the PL spectra, the samples were excited with the 532 nm line (2nd harmonic) of a Nd:YAG laser. A Lambda Physics excimer laser was used as the excitation source ($\lambda_{\text{exc}} = 308$ nm) for lifetime measurements. Emission lifetimes were measured with a Tektronics 1000 TDS 380 oscilloscope. The cathodoluminescence (CL) spectra were recorded with an Ocean Optics Spectrometer SD2000, with a resolution of 0.3 nm. The CL spectra were excited *in vacuo* ($<10^{-6}$ Torr) in the camera of a TESLA electron microscope operating at 60 and 90 kV, with the beam current in the range of 10–120 μA . Morphological and structural studies of thin layers of TiO₂ were performed with a transmission electron microscopy (TEM) Philips CM20 SuperTwin Microscope, operating at 200 kV and providing 0.25 nm resolution. Specimens for the TEM and for electron diffraction (SAED) studies were prepared by dissolving a quartz glass substrate of the obtained samples with HF acid, followed by ultrasonic agitation in methanol. A drop of the suspension was deposited onto a copper microscope grid covered with holey carbon film.

2.2. Preparation

The samples of nanocrystalline TiO₂ doped with europium and silver were prepared by the sol-gel technique. Titanium (IV) butoxide (TBOT, Ti[O(CH₂)₃CH₃]₄) was used as the titanium precursor and acetylacetonone (Acac, CH₃COCH₂COCH₃) as the chelating and stabilizing sol agent. The films were prepared by a sol-gel process involving four stages: (1) TBOT hydrolysis by stirring the system, TBOT:Acac

:H₂O:C₂H₅OH with molar ratios 1:4:1:27, at 50 °C; (2) addition of europium nitrate (Eu(NO₃)₃·6H₂O) to the obtained sol, with the molar ratio Eu/TBOT equal to 0.1; (3) obtaining thin films by deposition and spin-coating (3000 r.p.m) of the sols on silicon and quartz substrates, and (4) gelation of the samples followed immediately by heating at 500 °C for one hour.

3. Results and discussion

For the purpose of assessing the quality of the obtained Eu³⁺:TiO₂ films on Si substrates, morphological studies of the film surfaces were performed. The morphologies were examined with optical and transmission electron (TEM) microscopes. The undoped TiO₂ layers observed under optical magnification (not shown) showed a high homogeneity and a virtual lack of cracks. The TEM picture of nanocrystallites from an undoped film of TiO₂, obtained in a single deposition process, is presented in Fig. 1. Distinct TiO₂ nanocrystals with the sizes of about 15 nm can be seen in the micrographs. The structure of the obtained materials was investigated by the SAED method. All reflexes observed in electronograms (Fig. 2) correspond to the anatase structure of TiO₂ (Table 1).

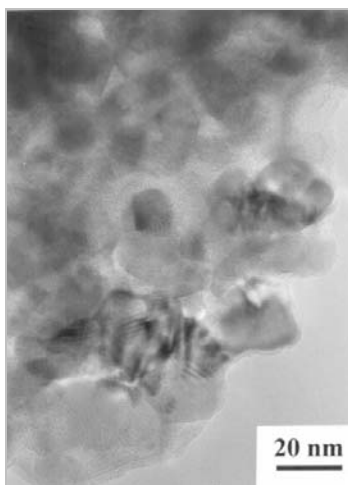


Fig. 1. TEM picture of TiO₂ nanocrystals

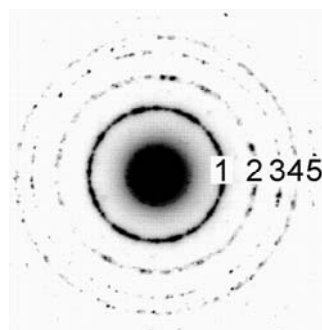


Fig. 2. SAED patterns typical of the anatase phase of TiO₂ samples

In order to determine the thickness of the layers by the optical method, analogous films were synthesized on quartz substrates. In this case, it is possible to estimate the thickness of the ultra-thin films via interference effects [9,10]. For this purpose, optical transmittance measurements of the films produced on quartz substrates were performed (see Fig. 3). The obtained transmittance values were introduced to the equations given by Aktulga et al. [15, 16]:

$$C(\lambda) = \frac{T^+(\lambda) - T^-(\lambda)}{2T^+(\lambda)T^-(\lambda)} \quad (1)$$

$$n_s(\lambda) = \frac{1 + \sqrt{1 + T_0^2(\lambda)}}{T_0(\lambda)} \quad (2)$$

$$n(\lambda) = \frac{1}{2} \left(\sqrt{8n_s C + (n_s + 1)^2} + \sqrt{8n_s C + (n_s - 1)^2} \right) \quad (3)$$

where λ is the wavelength of the incident light, T_0 is the transmittance of bare substrate, T^+ and T^- are experimentally traced envelope curves of the transmission spectrum and n_s is the refractive index of the substrate.

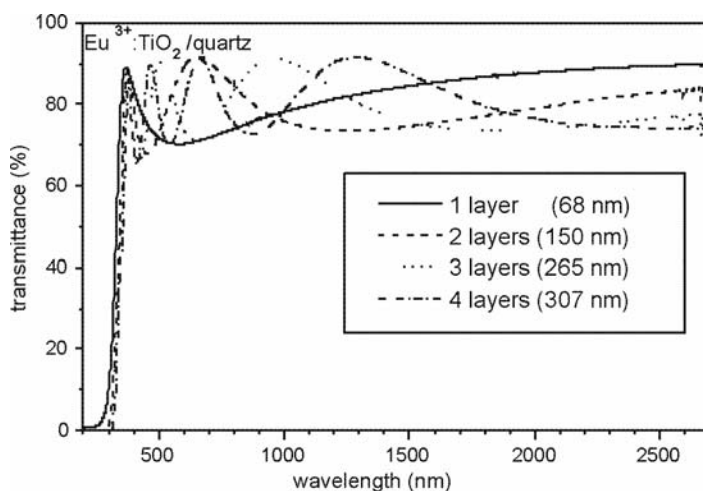


Fig. 3. Transmittance spectra of $\text{Eu}^{3+}:\text{TiO}_2$ films on quartz substrates

Table 1. Comparison of the interplanar distances obtained for the TiO_2 sample with the anatase data

No.	d [nm]	Anatase JCPD Nr. 21-1272		
		d (nm)	I	hkl
1	0.352	0.3520	100	101
		0.2431	10	103
2	0.238	0.2378	20	004
		0.2332	10	112
3	0.189	0.1892	35	200
4	0.169	0.1700	20	105
		0.1666	20	211
5	0.148	0.1493	4	213
		0.1481	14	204

The layer thickness d of the obtained samples can be determined from the following equation:

$$d = 4 \left(\frac{n(\lambda_i)}{\lambda_i} - \frac{n(\lambda_{i+1})}{\lambda_{i+1}} \right)^{-1} \quad (4)$$

where λ_i and λ_{i+1} are the wavelengths corresponding to two consecutive extrema in the transmittance spectrum.

Due to the lack of the necessary number of interference peaks in the transmittance spectra of the films obtained in one deposition process, the analyses of the thickness and refractive index were performed only for samples made with a minimum two deposition processes. The d values obtained for the investigated films are listed in Table 2. The accuracy of the method used was confirmed by FE-SEM images (Field Emission Scanning Electron Microscope, not shown), which were obtained for samples of the TiO₂ films.

Table 2. Thickness of doped TiO₂ thin films deposited on quartz substrates

Sample	Number of deposition processes	Thickness d (nm)	Refractive index n ($\lambda = 600$ nm)
Eu ³⁺ (10 %):TiO ₂	2	150	3.22
	3	265	3.24
	4	307	3.23

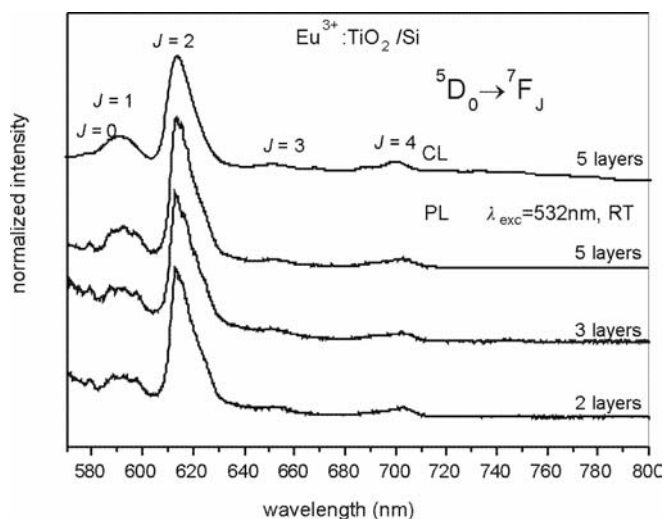


Fig. 4. The PL and CL spectra of samples of 10% Eu³⁺: TiO₂ on a silicon substrate after various numbers of deposition processes

As can be seen, the thickness of each subsequent layer decreases for successive deposition processes in the case of samples doped with Eu³⁺. The observed slight in-

crease in the refractive index n with the thickness of the films is due to the densification of films deposited earlier during the annealing of successive layers.

The photoluminescence (PL) spectra of TiO_2 films doped with Eu^{3+} ions were recorded at room temperature (Fig. 4). The spectra consist of characteristic of Eu^{3+} emission bands, which were attributed to the ${}^5\text{D}_0 \rightarrow {}^7\text{F}_{0,4}$ transitions. Assignments of the observed f-f transition are given in Figure 4. The luminescence spectra were characterized by inhomogeneously broadened bands characteristic of the Eu^{3+} multisite systems observed in glasses and solutions.

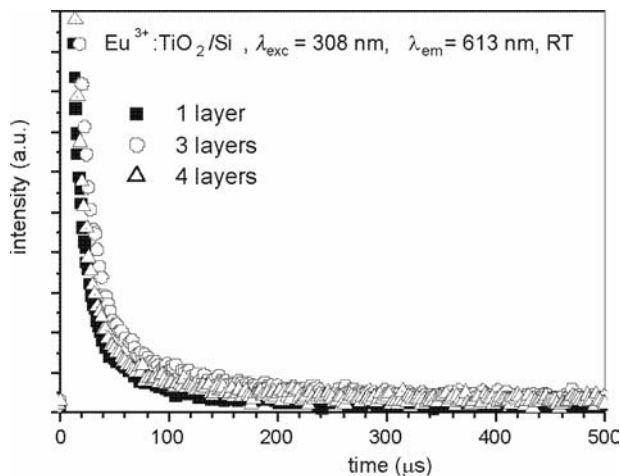


Fig. 5. Decay profiles of $\text{Eu}^{3+}:\text{TiO}_2$ samples measured at room temperature

The luminescence decay profiles of $\text{Eu}^{3+}:\text{TiO}_2$ thin films are shown in Fig. 5. They are highly nonexponential. This nonexponential decay of Eu^{3+} luminescence is associated with the energy transfer processes between Eu^{3+} ions occupying different sites. Luminescence lifetimes evaluated from the slower components of the decay curves (shown in Fig. 5 for the three selected samples – three layers of TiO_2 doped with Eu^{3+}) are listed in Table 3.

Table 3. Luminescence lifetimes of the ${}^5\text{D}_0 \rightarrow {}^7\text{F}_2$ transition measured for $\text{Eu}^{3+}(10\%):\text{TiO}_2$ samples on silicon substrates ($\lambda_{\text{em}} = 613 \text{ nm}$, $\lambda_{\text{exc}} = 308 \text{ nm}$, RT)

Number of deposition processes	Lifetime τ (μs)
1	93 ± 3
3	160 ± 4
4	130 ± 7

The estimated lifetimes are relatively short. An increase in the luminescence lifetimes for successive deposition processes was observed. It was probably due to the dehydration process occurring during the annealing. This process is more effective for longer heating times and is also manifested in the decrease of the thickness of each subsequently deposited layer. The influence of OH⁻ groups on the quenching of the luminescence transitions of Eu³⁺ entrapped in sol-gel derived materials has already been observed for other oxides [17, 18].

The results of CL measurements are also presented in Fig. 5. As can be seen, the CL characteristics differ significantly from the characteristics of the PL spectra. This difference is most probably due to a contribution of different Eu³⁺ sites, excited by the electron beam.

5. Conclusions

The synthesis of Eu³⁺:TiO₂ films of high optical quality is presented. Their structural and morphological properties have been determined. Photoluminescence spectra at room temperature and luminescence decay curves have been recorded. The luminescence displays inhomogeneously broadened bands characteristic of multisite Eu³⁺ structures. Its decay curves are nonexponential. Average luminescence lifetimes increase with the number of the deposition processes. A detailed analysis of the effect of film thickness on electronic relaxation mechanisms in Eu³⁺:TiO₂ needs further complementary research. The cathodoluminescence spectra of Eu³⁺:TiO₂ thin films have been recorded. They display different characteristics as compared to the photoluminescence spectra.

Acknowledgments

The authors are grateful to Dr. Mirosław Zawadzki for his assistance in the cathodoluminescence measurements and to Ms. Teresa Morawska-Kowal for the transmittance measurements. One of us (Dariusz Hreniak) is a holder of the scholarship of the Foundation for Polish Science (FNP).

References

- [1] CHO K.-J., RYU J.-T., LEE S.-Y., *Solid State Electron.*, 47 (2003), 633.
- [2] FRAN Y.-S., TSENG T.-Y., *Mater. Chem. Phys.*, 61 (1999), 166.
- [3] PAIK K.L., BAEK N.S., KIM H.K., LEE J.-H., LEE Y., *Opt. Mater.*, 21 (2003), 135.
- [4] WU X., LIU Y., ZHU D., *J. Mater. Chem.*, 11 (2001), 1327.
- [5] QIU Y., ZHANG D.Q., QIAO J., SHAO Y., *Synthetic Met.*, 110 (2000), 241.
- [6] ATHANASSOV Y., ROTZINGER F., PECHY P., GRAETZEL M., *J. Phys. Chem., B* 101 (1997), 2558.
- [7] ORIGNAC X., BARBIER D., DU X.M., ALMEIDA R.M., MCCARTHY O., YEATMAN E., *Opt. Mater.*, 12 (1999), 1.
- [8] NASSAR E.J., GONÇALVES R.R., FERRARI M., MESSADDEQ Y., RIBEIRO S.J.L., *J. Alloys Comp.*, 344 (2002), 221.
- [9] ZELLER P.N., VOIRIN G., KUNZ R.E., *Biosens. Bioelectron.*, 15 (2000), 591.

- [10] YANAGI H., HISHIKI T., TOBITANI T., OTOMO A., MASHIKO S., Chem. Phys. Lett., 292 (1998), 332.
- [11] TURNBULL G.A., ANDREW P., JORY M.J., BARNES W.L., SAMUEL I.D.W., Synthetic Met., 127 (2002), 45.
- [12] NISHIDA K., MORISAWA K., HIRAKI A., MURAISHI S., KATODA T., Appl. Surf. Sci., 159–160 (2000), 143.
- [13] OKIMURA K., Surf. Coat. Technol., 135 (2001), 286.
- [14] EUN D.S., LEE S.Y., Thin Solid Films, 357 (1999), 232.
- [15] DEMIRYONT H., SITE J.R., GEIB K.M., Appl. Opt., 24 (1985), 490.
- [16] OZER N., DEMIRYONT H., SIMMONS J.H., Appl. Opt., 30 (1991), 3661.
- [17] HRENIAK D., JASIORSKI M., MARUSZEWSKI K., KEPINSKI L., KRAJCYK L., MISIEWICZ J., STREK W., J. Non-Cryst. Solids, 298 (2002), 146.
- [18] WRZYSZCZ J., MISTA W., HRENIAK D., STREK W., ZAWADZKI M., GRABOWSKA H., J. Alloys Comp., 341 (2002), 358.

Received 28 April 2004

Revised 16 July 2004

Morphology, structural and absorption studies on gallium nitride powder

MARCIN NYK¹, WIEŚLAW STRĘK^{2*}, JANUSZ M. JABŁOŃSKI², JAN MISIEWICZ¹

¹Institute of Physics, Wrocław University of Technology,
Wybrzeże Wyspiańskiego 27, 50-370 Wrocław, Poland

²Institute of Low Temperature and Structure Research, Polish Academy of Sciences,
P.O. Box 1410, 50-950 Wrocław 2, Poland

A simple method of synthesis of nanocrystalline GaN powders is presented. The morphology and structure of the powders was characterized by XRD and TEM methods. It was observed that the sizes of single grains of gallium nitride depend on parameters of the technological process. Using the Sherrer's rule, the sizes of crystallites were determined to be in the range of 14–33 nm. It was found that *a* and *c* parameters of hexagonal gallium nitride slightly depend on the crystallite size. Changes of the absorption edge and Urbach energies are presented.

Key words: *GaN nanocrystallite; absorption; semiconductor*

1. Introduction

Gallium nitride and related compounds are important materials used in light-emitting devices and lasers operating in the UV spectral region [1, 2]. Recently, nanostructured GaN materials have attracted extensive interest because of their importance in the fundamental physical research but also due to emerging applications in optoelectronics and nanotechnology [3]. As members of the family of III–V group nitrides, AlN, GaN, InN and their alloys are wide-band-gap materials (6.2 eV for AlN, 3.4 eV for GaN and 1.9 for InN at room temperature), and can crystallize in both wurtzite and zinc-blende polytypes [4]. GaN crystallizes in either a thermodynamically stable wurtzite structure having hexagonal symmetry or a meta-stable zinc-blende structure with cubic symmetry [5]. Nitride semiconductors frequently contain large concentrations of impurities, introduced either intentionally or unintentionally. It is well known that the incorporation of impurities can affect the lattice parameters

* Corresponding author, e-mail: strek@int.pan.wroc.pl.

of semiconductor [6]. The latter depend on the following factors: (i) free-electron concentration via the deformation potential of a conduction-band minimum occupied by these electrons, (ii) concentration of dopants (or point defects) and the difference of ionic radii of the host and guest ions (size effect), (iii) strains (including those induced by lattice mismatch between a substrate and a layer), and (iv) thermal expansion change by free charges (if the measurements are performed at non-zero temperatures) [7]. The lattice parameters of gallium nitride were reported in a number of papers [8–10]. Song [8] performed the lattice constant refinement for bulk GaN single crystal and obtained the following values: $a = 3.1903(3) \text{ \AA}$, and $c = 5.1864(6) \text{ \AA}$. In Refs. [9, 10], the values: $a = 3.180 \text{ \AA}$, $c = 5.180 \text{ \AA}$ and $a = 3.186 \text{ \AA}$, $c = 5.174 \text{ \AA}$, respectively, were reported for GaN powder.

A considerable effort has been put in last years into studies of GaN semiconductor materials exhibiting blue emission: bulk crystals [11], thin films [12] and powders were investigated. In the last few years, the interest has been focused on the GaN nanostructures [13–15] and several methods of their fabrication were put forward. We have recently reported a sol-gel preparation of GaN nanocrystallites embedded in silica glass which demonstrated an intense yellow emission [16]. In the present paper, we report a simple method of the chemical synthesis of pure GaN nanopowders. Their X-ray diffraction patterns and physical properties were studied.

2. Experimental

2.1. Powder preparation and nitridation

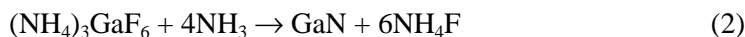
Three 0.5 g samples of Ga_2O_3 (99.999%) were used in our experiments. After their solubilization in hot concentrated nitric acid ($\sim 115 \text{ }^\circ\text{C}$), the solutions were evaporated to dryness. The obtained powders were carefully dried in an oven on gradually increasing the temperature from 70 to 200 $^\circ\text{C}$. Then the powders, put into alumina crucibles, were inserted into a quartz tube (24 mm ID) and calcined at 500 $^\circ\text{C}$ for 4 h in air flow ($100 \text{ cm}^3/\text{min}$) to convert $\text{Ga}(\text{NO}_3)_3$ into Ga_2O_3 . The crushed powder samples were placed at room temperature into a quartz tube in NH_3 flow ($120 \text{ cm}^3/\text{min}$), and after purging (20 min) the samples were heated ($10 \text{ }^\circ\text{C}/\text{min}$) to the required temperature, i.e., to 700 $^\circ\text{C}$ (sample A), 850 $^\circ\text{C}$ (sample B) and 1050 $^\circ\text{C}$ (sample C) and then were held at the target temperature for 3.5 h. NH_3 used for nitridation (from Messer, Poland, 99.85 vol.%) was additionally purified by passing it over a zeolite trap.

The reaction proceeds according to the scheme:



One of the gallium nitride samples was prepared according to a slightly modified procedure given in Ref. [18]. This so-called “fluoride method” allows us to obtain GaN nanopowder via the pyrolytic reaction of the ammonium hexafluorogallate, $(\text{NH}_4)_3\text{GaF}_6$ with flowing ammonia at 700 $^\circ\text{C}$.

The reaction proceeds according to the scheme:



2.2. Sample characterization

Overall phase compositions of the nanopowders were determined by X-ray powder diffraction with a Siemens D5000 diffractometer and $\text{CuK}_{\alpha 1}$ radiation, $\lambda = 0.15406$ nm. The microstructure of the samples was examined with a Philips CM20 SuperTwin transmission electron microscope (TEM), which provides a resolution of 0.25 nm at 200 kV.

Absorption spectra were recorded in the range of 1.5–4.5 eV at room temperature with a Cary–Varian 5 spectrophotometer.

3. Results and discussion

Figure 1 shows the XRD patterns of GaN powders. All patterns show the diffraction lines which could be ascribed to the formation of hexagonal gallium nitride with a wurtzite-type structure (JCPDS file No. 02-1078).

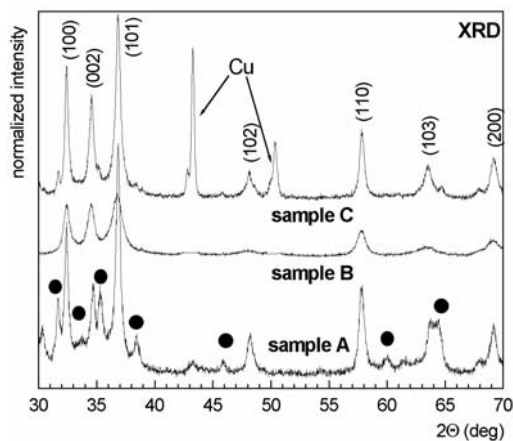


Fig. 1. XRD pattern of GaN nanocrystallite powders. For clarity, the peaks at $2\theta = 43.30$ and 50.43° due to the copper sample holder (sample B) have been deleted

For the sample A and, to a lower extent, for the sample C we observed additionally the peaks of crystalline gallium oxide (black dots) (JCPDS file No.11-0370) which at temperature of 700°C was not converted into gallium nitride. The diffraction peaks were broadened indicating that the GaN nanocrystals are very small. The average grain sizes were determined by means of the Scherrer formula [17], and are listed in Table 1, together with the lattice parameters for the hexagonal gallium nitride.

The analysis of TEM micrographs (Fig. 2) clearly indicates that the samples contain aggregated crystallites with the sizes of 20–50 nm (sample C) and 50–110 nm

(sample A), i.e. much larger than those evaluated from XRD (see Table 1). These discrepancies could be due to the fact that the use of the Scherrer formula allows us to determine an average size of the individual crystallites whereas the transmission electron microscopy in certain cases reflects the dimension of the whole agglomerated particle composed of a few nanocrystallites. For the samples nitrided at 850 °C (micrographs not shown here), the average GaN crystallite sizes were 20–100 nm. The spatial distribution of GaN nanocrystals in the samples appears to be rather uniform. The selected area electron diffraction (insets Fig. 2) could be indexed as a hexagonal GaN phase. The lattice plane spacings agree well with those for the hexagonal GaN phase: (100) 2.76Å, (002) 2.59Å and (101) 2.43Å.

Table 1. Lattice parameters of GaN powders

Composite	Crystal mean size ¹ $d \pm 0.1$ (nm)	Crystal structure	Position (2θ)	hkl	Lattice constant ² (Å)	
					$a \pm 0.001$	$c \pm 0.001$
GaN ³ (700°C) (sample A)	21.5	wurtzite	32.432	100	3.187	5.170
			34.661	002		
			36.863	101		
GaN (850°C) (sample B)	14.4	wurtzite	32.394	100	3.194	5.199
			34.484	002		
			36.720	101		
GaN (1050°C) (sample C)	33.1	wurtzite	32.381	100	3.191	5.190
			34.535	002		
			36.810	101		

¹Calculated using the Scherrer formula [17].

²Calculated using a set of power equation for hexagonal arrangements.

³Sample prepared by using the fluoride method [18].

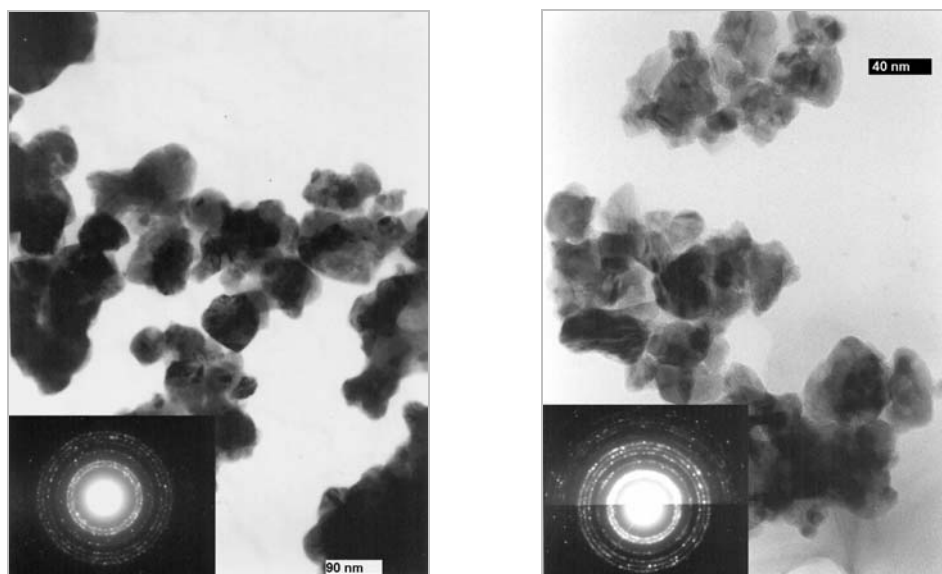


Fig. 2. TEM image and SAED pattern of a GaN nanoparticle nitrided at: a) 700 °C, b) 1050 °C

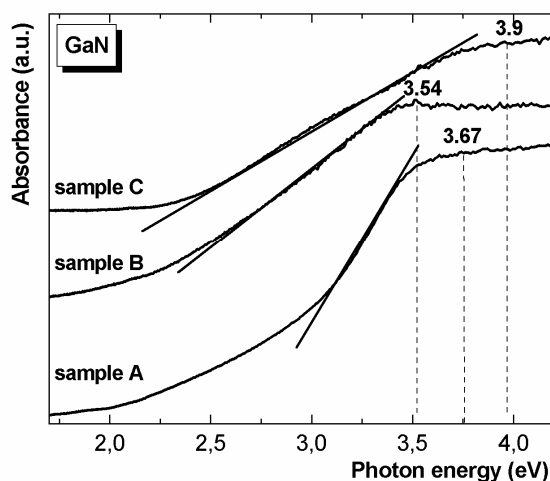


Fig. 3. Absorption coefficient as a function of energy for the sample A nitrided at 700 °C, sample B at 850 °C and sample C at 1050 °C

In Figure 3, the band gap absorption at 300 K, measured in the range of 1.5–4.5 eV, is shown for three samples differing in average sizes of GaN grains. We found that the energy of the absorption edge (E_g) depends on the annealing temperature and hence on the size of grains: $E_g = 3.67$ eV (sample A), $E_g = 3.54$ eV (sample B) and $E_g = 3.9$ eV (sample C) [19, 20]. The regions of the so-called Urbach spectral tail can be found in the spectra of the samples A, B and C. The absorbance (α) in this spectral region can be approximated by a linear function and, consequently, for $3.0 \text{ eV} < h\nu < 3.5 \text{ eV}$

$$\alpha(h\nu) \approx b + \frac{h\nu - E_g}{U} \quad (3)$$

where b is a constant, and U is the so-called Urbach energy.

In the low energy region the spectral dependence of the absorption coefficient is characterized by a small slope and hence, by an extremely large Urbach energy, $U = 0.7$ eV for sample A, $U = 1.4$ eV for sample B and $U = 2$ eV for sample C. This parameter was found to be dependent on the crystal size and annealing temperature. Jacobson et al. reported [21] for GaN films that the Urbach tails are combined of two linear functions characterized by two energies: $U_1 = 400\text{--}470$ meV and $U_2 = 10\text{--}20$ meV. We believe that the first part with a large Urbach energy U_1 is associated with the presence of a strongly disordered material.

3. Conclusions

GaN nanocrystalline powders have been prepared using a simple synthetic method, the so-called combustion method. The size of GaN particles was found to

depend on the nitridation temperature and ranged from 14 up to 33 nm as found by the Scherrer method. The sizes of agglomerated particles, however, estimated from TEM were found much larger, attaining 110 nm. The phase composition, morphology and absorption properties of GaN nanocrystalline powders have been also determined. Changes of the edge of absorption and Urbach energies are presented. The Urbach energy was found to increase with increasing temperature of nitridation.

Acknowledgements

The authors thank Dr M. Wołczyr for recording XRD patterns and L. Krajczyk M.Sc. for performing electron microscope experiments. M.N. thanks the Centre of Advanced Materials and Nanotechnology, Wrocław University of Technology for the scholarship.

References

- [1] ALDABERGENOVA S.B., OSVET A., FRANK G., STRUNK H.P., TAYLOR P.C., ANDREEV A.A., *J. Non-Cryst. Solids*, 299 (2002), 709.
- [2] LEE D.S., STECKL A.J., *Appl. Phys. Lett.*, 81 (2002), 2331.
- [3] HUI R., TAHERION S., WAN Y., *Appl. Phys. Lett.*, 82 (2003), 1326.
- [4] MURALI A.K., LEPPERT V.J., RISBUD S.H., *Mat. Sci. Eng.*, B76 (2000), 206.
- [5] KIM J.H., HOLLOWAY P.H., *Appl. Phys. Lett.*, 84 (2004), 711.
- [6] VAN DE WALLE C.G., *Phys. Rev.*, B68 (2003), 165209.
- [7] LESZCZYNSKI M., TEISSEYRE H., SUSKI T., GRZEGORY I., BOCKOWSKI M., JUN J., POROWSKI S., PAKULA K., BARANOWSKI J.M., FOXON C.T., CHENG T.S., *Appl. Phys. Lett.*, 69 (1996), 73.
- [8] SONG Y., *J. Cryst. Growth*, 247 (2003), 275.
- [9] KIM B.C., SUN K.T., PARK K.S., IM K.J., NOH T., SUNG M.Y., KIM S., NAHM S., CHOI Y.N., PARK S.S., *Appl. Phys. Lett.*, 80 (2002), 479.
- [10] SENTHIL KUMAR M., *Mat. Chem. Phys.*, 77 (2002), 341.
- [11] KAMLER G., ZACHARA J., PODSIADŁO S., ADAMOWICZ L., GĘBICKI W., *J. Cryst. Growth*, 212 (2000), 39.
- [12] SARDAR K., RAJU A.R., SUBBANNA G.N., *Sol. State Com.*, 125 (2003), 355.
- [13] KISAILUS D., CHOI J.H., LANGE F.F., *J. Cryst. Growth*, 249 (2003), 106.
- [14] JIAN J.K., CHEN X.L., HE M., WANG W.J., ZHANG X.N., SHEN F., *Chem. Phys. Lett.*, 368 (2003), 416.
- [15] PEARTON S.J., REN F., ZHANG A.P., LEE K.P., *Mat. Sci. Eng.*, R30 (2000), 55.
- [16] NYK M., JABŁOŃSKI J.M., STRĘK W., MISIEWICZ J., *Opt. Mat.*, 26 (2004), 133.
- [17] KLUG P., ALEXANDER L.E., *X-ray Diffraction Procedure*, Wiley, New York, 1954.
- [18] GARCIA R., HIRATA G.A., FARIAS M.H., MCKITTRICK J., *Mat. Sci. Eng.*, B90 (2002), 7.
- [19] BENTOUMI G., DENEUVILLE A., BEAUMONT B., GIBART P., *Mat. Sci. Eng.*, B50 (1997), 142.
- [20] AMBACHER O., RIGER W., ANSMANN P., ANGERER H., MOUSTAKAS T.D., STUTZMANN M., *Solid State Commun.*, 97 (1996), 365.
- [21] JACOBSON M.A., NELSON O.V., ROMANOVSKII S.O., HATZOPOULOS Z., *J. Cryst. Growth*, 230 (2001), 459.

Received 20 April 2004

Revised 28 July 2004

Relaxation processes in ZrO₂ at high pressures*

ILIA V. KORIONOV^{1**}, ANNA N. TREFILOVA¹, ALEXEY N. BABUSHKIN¹,
WITOLD ŁOJKOWSKI², AGNIESZKA OPALIŃSKA²

¹Department of Physics, Ural State University, Lenina 51, Ekaterinburg, Russia

²High Pressure Research Center, Polish Academy of Sciences,
ul. Sokołowska 29/37, 01-142 Warsaw, Poland

Relaxation processes in ZrO₂ have been studied at pressures in the range of 22–50 GPa by measurements of high-pressure electrical relaxation of resistance in time. Electrical relaxation in nanocrystalline praseodymium doped zirconia powders and in a bulk material sample of zirconia has been measured in the pressure range from 35.5 to 50 GPa. The time dependence of electric resistance is most precisely described by exponential function up to the pressure of 35.5–50 GPa. The time dependence of electric resistance is most precisely described by exponential function up to the pressure 44–45.5 GPa. After treatment the pressure higher than 45.5 GPa, the character of the relaxation changes and resistance increased with time. Relaxation processes have not been observed in ZrO₂ with 56 nm crystallite sizes.

Key words: *zirconium dioxide; electrical relaxation; pressure-induced phase transition; nanocrystalline sample*

1. Introduction

Zirconium dioxide is an important material with rather interesting mechanical, optical and electrical properties. The material is a major component of the best known fuel cell materials [1]. Previous studies have been devoted to investigation of the behaviour of pure ZrO₂ at a pressure of about 20 GPa, at room temperature [1]. This work shows that for pure ZrO₂ monoclinic-Ortho-I and Ortho-I-Ortho-II phase boundaries occur at about 4 GPa and 12 GPa, respectively. At high temperatures, pure ZrO₂ crystallizes in a cubic fluorite structure. On cooling, it undergoes a displacive transformation to a related structure of tetragonal fluorite and then, via a martensitic transition, to a monoclinic baddeleyite-type structure [2]. However, the behaviour of ZrO₂ at pressures exceeding 20 GPa and at high temperatures has not been extensively studied so far.

*The paper presented at the 5th High Pressure School on High Pressure Methods in Biotechnology and Materials Science, E-MRS Fall Meeting, Warsaw, 13–15 September, 2003.

**Corresponding author, e-mail: korionov-2002@yandex.ru.

In this paper, we report the results of a study on the electrical relaxation properties of samples of ZrO_2 with different sizes of crystallites in a pressure range between 35.5 and 50 GPa. The size of crystallites was changed from 10 to 500 nm.

2. Experiment

The dc conductivity measurements were carried out in a diamond anvil cell (DAC), with anvils of the “rounded cone-plane” type made of synthetic carbonado type diamonds [3]. Such anvils are good conductors, permitting measurements of the resistance of samples placed between them in the DAC. The procedure for determining the pressure reached in a DAC of the “rounded cone-plane” type has been described in [4, 5].

Measurements were made on powder samples of ZrO_2 with various crystallite sizes. Moreover, we also studied a bulk material sample of zirconia with Y_2O_3 content of 5 mol %. The crystallite sizes in the latter material were near 500 nm. Nanopowders of ZrO_2 contained 0.5 mol % of Pr. Their sizes ranged from 10 to 50 nm. The bulk material samples were synthesized by the Daiichi Daiichi Kigensou Company in Japan (Lot # NEY-5M LO524). Nanocrystalline praseodymium doped zirconia powders were produced using a microwave driven hydrothermal process under pressures up to 8 GPa [6]. These samples were synthesized at the High Pressure Research Centre of the Polish Academy of Sciences.

3. Experimental results and discussion

In Figure 1, the dependence of resistance on time for the sample with 10 nm crystallite size has a negative-going exponential mode for pressures below 45.5 GPa

$$R(t) = (R_{\max} - R_{\min})\exp(-t/\tau) + R_{\min} \quad (1)$$

A change in the type of relaxation is observed at a pressure of 45.5 GPa. Resistance increases with time. The latter corresponds to the process described by the equation

$$R(t) = (R_{\min} - R_{\max})\exp(-t/\tau) + R_{\max} \quad (2)$$

For the sample with 12 nm crystallite size (Fig. 2), the relaxation dependencies of the resistance are described by Equation (1) for all pressures. In the sample with 56 nm crystallite size, no relaxation processes were observed (the resistance did not depend on time). In the bulky sample, the relaxation processes are described by Equation (2) and observed only for pressures up to 44 GPa. The baric dependencies of the characteristic relaxation times (τ) for nanosamples with the crystallite sizes of 10 and 12 nanometers and for a polycrystalline sample are shown in Figure 3. As can be

seen from these graphs, the represented baric dependencies have their anomaly between 42 and 44 GPa. The latter leads us to suppose the presence of considerable changes in the electronic structure of ZrO_2 at this pressure.

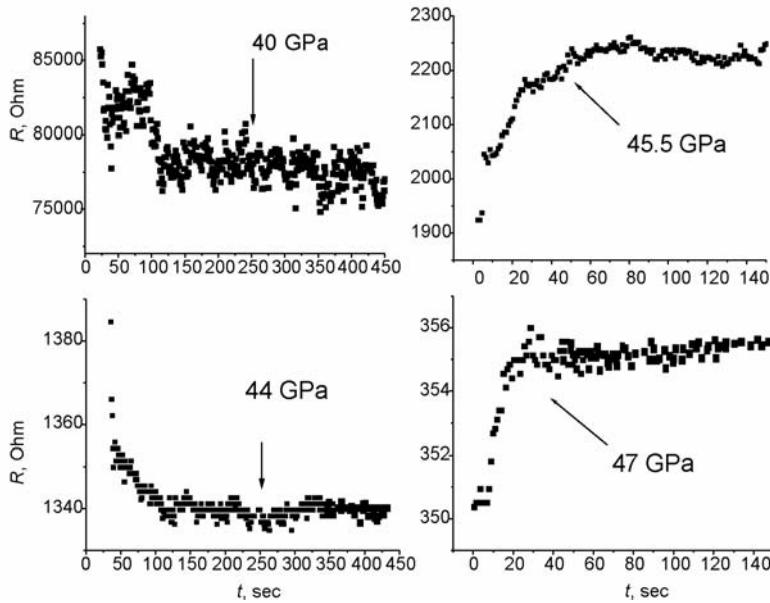


Fig. 1. The relaxation process in ZrO_2 containing 0.5% Pr with 10 nm crystallite size

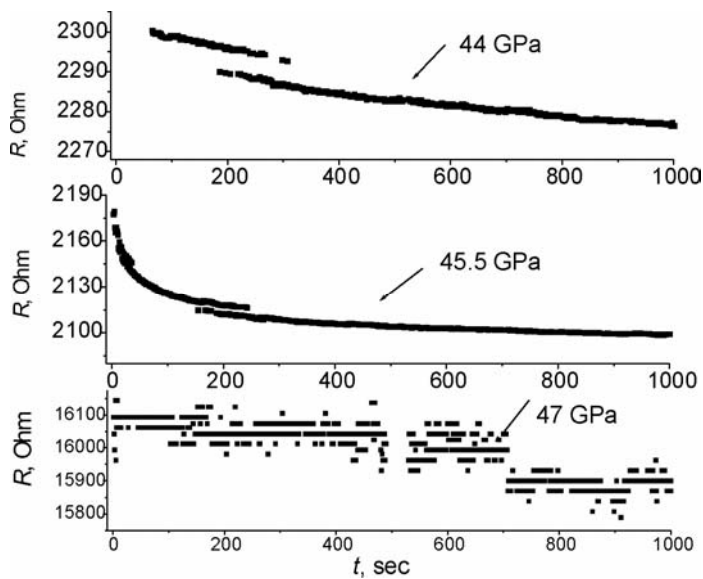


Fig. 2. The relaxation process in ZrO_2 containing 0.5% Pr with 12 nm crystallite size

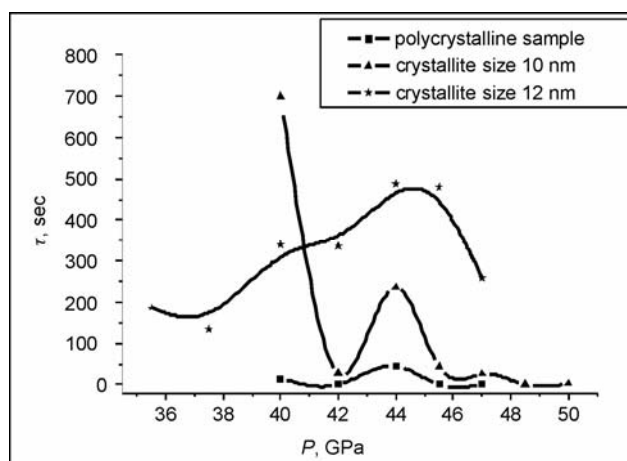


Fig. 3. The baric dependencies of the characteristic relaxation times (τ) (the error of τ does not exceed 5 sec)

Our results demonstrate that changes in the electronic spectrum may be connected with a structural phase transition in ZrO_2 . Furthermore, a substantial increase of the characteristic relaxation time under pressures up to 44 GPa can be associated with structure modifications at these pressures.

Acknowledgements

This research was partially financed by grants RBRF No. 01-03-96494 and BRHE No. EK-005-X1.

References

- [1] LEGER J.M., TOMASZEWSKI P.E., ATOUF A., PEREIRA A.S., Phys. Rev. B, 47 (1993), 14075.
- [2] OHTAKA O., FUKUI H., KUNISADA T., FUJISAWA T., FUNAKASHI T., UTSUMI W., IRIFUNE T., KURODA K., KIKEGAWA T. Phys. Rev. B, 63 (2001), 174108.
- [3] VERECHAGIN L.F., YAKOVLEV E.N., STEPANOV G.N., BIBAEV K.H., VINGRADOV B.V., JETF Lett., 16 (1972), 3.
- [4] BABUSHKIN A.N. High Pressure Res., 6 (1992), 349.
- [5] BABUSHKIN A.N., KANDRINA Y.A., KOBELEVA O.L., SCHKERIN S.N., VOLKOVA Y.Y. [in:] *Frontiers of High Pressure Research II: Application of High Pressure to Low-Dimensional Novel Electronic Materials*. H. D. Hochheimer, B. Kuchta, P. K. Dorhout, J. L. Yarger (Eds.), Kluwer Acad. Publ., Dordrecht, 2001, p. 131.
- [6] BONDIOLI F., FERRARI A.M., BRACCINI S., LEONELLI C., PELLACANI G.C., OPALIŃSKA A., CHUDOBA T., GRZANKA E., PALOSZ B., ŁOJKOWSKI W., *Book of Abstracts*, E-MRS 2003 Fall Meeting, Warsaw University of Technology, Warsaw, Poland (2003), p. 190.

Received 18 February 2004

Revised 30 July 2004

Effect of double substituted *m*-barium hexaferrites on microwave absorption properties

ROBERTO DA COSTA LIMA^{1,2*}, MAGALI SILVEIRA PINHO^{1,3}, MARIA LUISA GREGORI¹,
REGINA CÉLIA REIS NUNES³, TSUNEHARU OGASAWARA²

¹Instituto de Pesquisas da Marinha, Rio de Janeiro, RJ, Brazil

²Engenharia Metalúrgica da Universidade Federal do Rio de Janeiro, Rio de Janeiro, RJ, Brazil

³Instituto de Macromoléculas (IMA) da Universidade Federal do Rio de Janeiro, Rio de Janeiro, RJ, Brazil

The complex permeability (μ_r^*) and permittivity (ϵ_r^*) of radar absorbing materials (RAMs) play a key role in determining the reflection and attenuation properties of incident microwaves. Their real (μ' and ϵ') and imaginary (μ'' and ϵ'') components and relationship with microwave absorbing properties have been investigated in the frequency range 8–16 GHz for doped M-type barium hexaferrites in polychloroprene (CR) matrices. Individual and simultaneous substitutions of Fe^{3+} ions by Co^{2+} , Ti^{4+} , and Mn^{3+} , and of Ba^{2+} ions by La^{3+} and Na^+ make possible the use of these materials as RAMs, due to frequency dependence of μ_r^* of hexaferrite, responsible for the location of its natural resonance. A double substitution of Ba^{2+} and Fe^{3+} (LaNaCoTiMn-BaHF) resulted in the best microwave absorption (99.9%) at the frequency of 15 GHz.

Key words: *microwave absorbing materials; doped ferrites; composites; waveguide*

1. Introduction

The reduction of military platform radar cross-sections has been a major challenge since the second world war. Possible solutions for reducing the radar signatures of targets include the design of objects with small cross sections or the use of radar absorbing materials (RAMs) for covering the metallic surface. In this way, microwave absorbers have been widely used to prevent or minimize electromagnetic reflections from large structures such as aircraft, ships and tanks, and also to cover walls of anechoic chambers [1–4].

* Corresponding author, e-mail: r.c.lima@uol.com.br.

The main problem in designing a magnetic absorber is related to the choice of the material, preferentially with control over some magnetic and dielectric properties, such as permeability (μ), permittivity (ϵ) and the dissipation factor ($\tan\delta$) [5]. The use of hexaferrites as RAMs has been widely cited in literature during the last two decades. The choice of polychloroprene (CR) as the material for the elastomeric matrix was due to its favourable properties, including excellent resistance to ageing, sea water and flame retardant behaviour, which allows using it for naval applications [6–8].

A basic formula of hexagonal ferrites is $\text{MeFe}_{12}\text{O}_{19}$, where Me is a divalent metal such as Ba or Sr. The substitution of Fe^{3+} ions by Co^{2+} , Ti^{4+} , and Mn^{3+} makes possible the use of these materials as RAMs in the frequency range from 8 to 16 GHz. In the same way, individual or simultaneous substitution of Ba^{2+} ions by La^{3+} and Na^{+} can also change the magnetic behaviour of these materials, allowing their application as RAMs at various frequencies [3, 4].

2. Experimental

Synthesis and characterization of ferrimagnetic materials. In this work, M-type barium hexaferrites of the basic composition $\text{BaFe}_{12}\text{O}_{19}$ (BaHF) were synthesized by the mixing oxide route. In order to obtain the composition $\text{BaFe}_{10.2}\text{Co}_{0.85}\text{Ti}_{0.85}\text{Mn}_{0.1}\text{O}_{19}$, referred to as CoTiMn-BaHF, Fe^{3+} ions were partially replaced by Co^{2+} , Ti^{4+} and Mn^{3+} ions. In the same way, Ba^{2+} was substituted by La^{3+} and Na^{+} , resulting in the composition $\text{Ba}_{0.8}\text{La}_{0.10}\text{Na}_{0.10}\text{Fe}_{12.0}\text{O}_{19}$ (LaNa-BaHF). The composition $\text{Ba}_{0.8}\text{La}_{0.10}\text{Na}_{0.10}\text{Co}_{0.85}\text{Ti}_{0.85}\text{Mn}_{0.1}\text{Fe}_{10.2}\text{O}_{19}$ (LaNa CoTiMn-BaHF), resulting from the simultaneous substitution of Fe^{3+} and Ba^{2+} , was also prepared. Raw materials used for obtaining the stoichiometric mixtures, with 99.9% purity, were cobalt oxide (CoO), barium carbonate (BaCO_3), iron oxide (Fe_2O_3), sodium carbonate (Na_2CO_3), lanthanum hydroxide ($\text{La}(\text{OH})_3$), manganese oxide (Mn_2O_3), and titanium oxide (TiO_2) [6, 8–10].

A small amount of $\text{La}(\text{OH})_3$ present in barium hexaferrite is known to form an anisotropic magnetoplumbite structure with optimum ferromagnetic properties [10].

Mixing was carried out in a ball mill for 24 h, using Y-TZP as the milling media. After mixing, the slurry was dried at 100 °C. All samples were calcined in air at 1200 °C for 2 h, except LaNaCoTiMn-BaHF, which was calcined for 2½ h.

The powders obtained were characterized by X-ray Diffraction (XRD, Bruker-AXS D5005), Scanning Electron Microscopy (SEM, Leica S440), and Vibration Sample Magnetometry (VSM 4500, EG & G Princeton Applied Research) [8].

Preparation of composites with polychloroprene by bulk process. The composite specimens for measuring microwave absorber properties were prepared by mixing, molding and curing mixtures of barium hexaferrite powders with polychloroprene (CR, neoprene W of Du Pont, density 1.21 g/cm³) and the additives of vulcanization. This resulted in a barium hexaferrite:polychloroprene concentration of 80:20 by weight. The processing was carried out in a Berstorff mill at room temperature, with velocities of 22 and 25 rpm

(back and forward). Vulcanized samples $4.00 \times 4.00 \times 0.15 \text{ cm}^3$ in size were obtained by compression molding in a hydraulic press at $150 \text{ }^\circ\text{C}$ and 6.7 MPa . The curing times were determined from the data obtained with a Monsanto Rheometer TM100 [8].

Measurement system for transmission/reflection. Properties of the microwave absorber were evaluated in the frequency range of 8–16 GHz using the Transmission/Reflection method (T/R) [11], after tightly inserting the vulcanized samples into a rectangular waveguide. Using the data obtained from each of the measured samples (ϵ' , ϵ'' , μ' and μ''), expected values of the microwave reflectivity level were determined by measuring variations of the reflection loss (dB) versus frequency (GHz) using an HP 8510 network analyzer system [8, 12].

In microwave absorption measurements a rectangular waveguide was used as the transmission/reflection medium. The waveguide sample holder ($22.86 \times 10.16 \text{ mm}^2$) was fabricated by cutting the flange from an X-band standard waveguide 8 mm in length. The measurement calibration procedure adopted typical waveguide standards: a $\lambda_{\text{gm}}/4$ off-set (“line”), a short circuit (“reflect”), and a “thru” measurement (where λ_{gm} is the guided wavelength at the geometric mean frequency for the X-band). In order to avoid undesirable resonances during the measurements, the thickness of the samples was limited to 1.0–2.0 mm.

3. Results

Figure 1 shows the hysteresis curves for doped (LaNa-BaHF, CoTiMn-BaHF, LaNaCoTiMn-BaHF) and undoped (BaHF) barium hexaferrites.

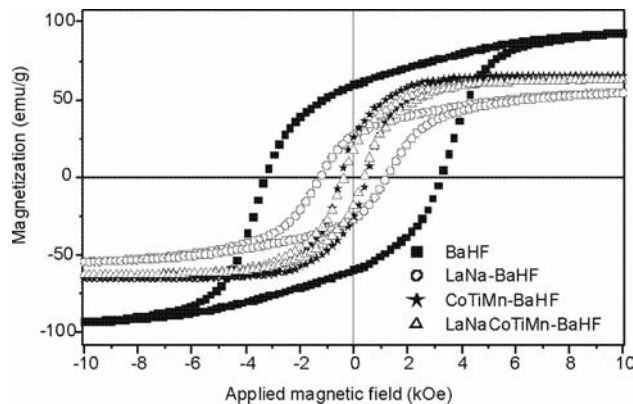


Fig. 1. Hysteresis curves for doped and undoped barium hexaferrites

As can be seen, the doped hexaferrites in comparison to the undoped ones show a reduction in the coercive field (H_c). A high value of H_c for undoped hexaferrite (3.26 kOe), in addition to its high anisotropy ($1350 \times 10^3 \text{ A}\cdot\text{m}^{-1}$), places this material among magnetically hard ones. On the other hand, small values of H_c for CoTiMn-BaHF (0.50

kOe), LaNa-BaHF (1.18 kOe), and LaNaCoTiMn-BaHF (0.40 kOe), in addition to smaller values of their anisotropy, classify these materials as magnetically soft. Consequently, the addition of dopants is responsible for the reduction of the magnetic hardness and magnetization of barium hexaferrites. Among the doped barium hexaferrites, La-NaBaHF shows the highest magnetic hardness.

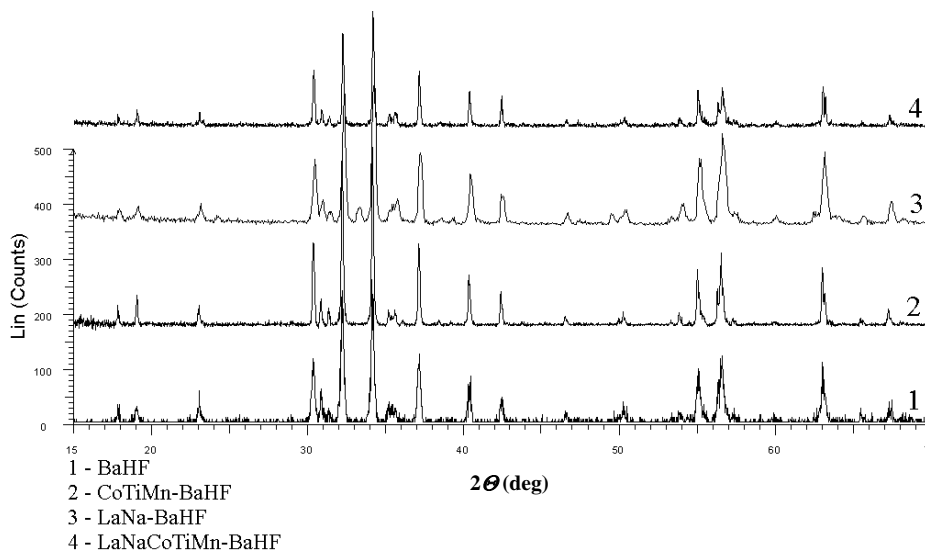


Fig. 2. X-Ray diffraction curves for doped and undoped barium hexaferrites

Figure 2 shows X-ray diffraction curves for the doped and undoped hexaferrites, in agreement with those given in JCPDS Card No. 43-0002, confirming the magnetoplumbite structure for these materials. The peaks for the doped barium hexaferrites appear at the same positions as the ones for the undoped hexaferrite, but with different intensities. According to JCPDS Card No. 33-0664, hematite (Fe_2O_3) is shown to be present besides the hexaferrite phase for the LaNa-BaHF composition, although lanthanum orthoferrite is reported in literature to be the second phase [13]. The presence of this second phase can be attributed to differences in the sizes of Ba^{2+} , Na^+ , and La^{3+} ions. In LaNa-BaHF, two cations of Ba^{2+} (1.34 Å) are substituted by one La^{3+} (1.05 Å) and one Na^+ (0.97 Å). In this way, the introduction of La^{3+} and Na^+ changes the interatomic distances and super-exchange interactions, which results in precipitation of hematite or lanthanum orthoferrite as the second phase.

The presence of hematite as the second phase in the formation of LaNaBaHF can be responsible for the largest reduction in magnetization.

SEM micrographs of the doped ferrites are shown in Figure 3. The presence of the second phase (hematite) in the form of small particles is observed only in Figure 3b, for the LaNa-BaHF composition, which is in accordance with X-Ray results. The presence of larger hexagonal particles, visible in Figure 3c, can result from longer calcination times.

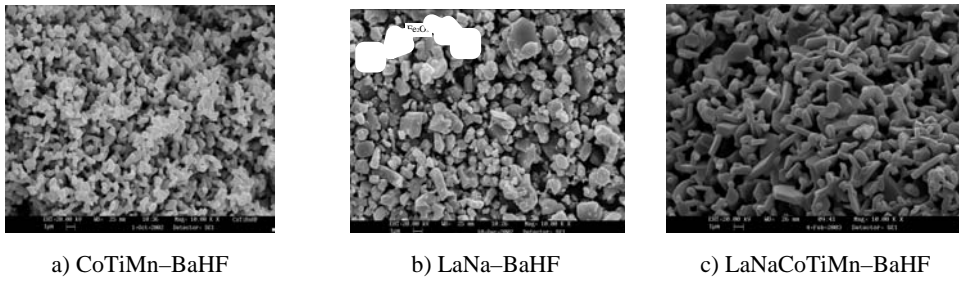


Fig. 3. SEM images of doped barium hexaferrites

The frequency dependencies of real and imaginary parts of the complex permittivity (ϵ' and ϵ'') and complex permeability (μ' and μ'') for barium hexaferrite:polychloroprene composites are shown in Figures 4 and 5.

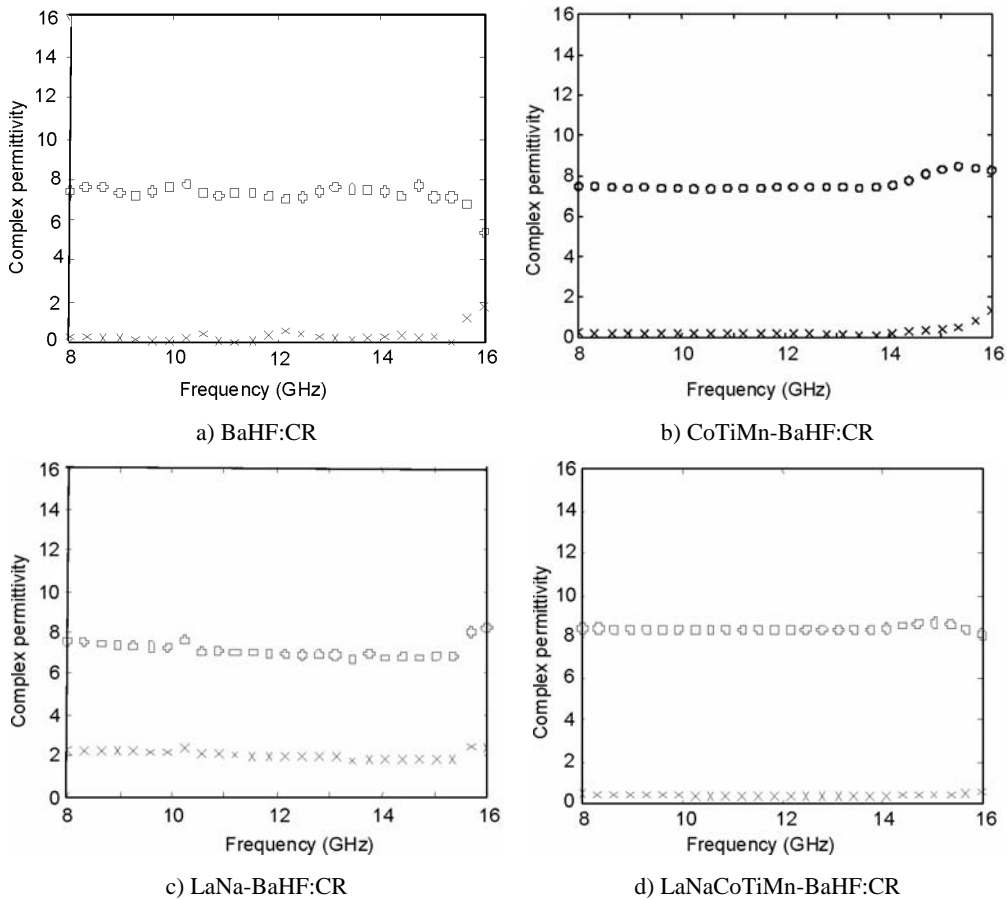


Fig. 4. Dispersion of the real (ϵ' , O) and imaginary parts (ϵ'' , X) of the complex permittivity of barium hexaferrite:polychloroprene composites

The permeability of hexaferrite:polymer composites depends on the composition of the hexaferrite, the nature of the polymer, and the operation frequency [14].

Dielectric properties of polycrystalline hexaferrite:polychloroprene composites result from the heterogeneous structure of hexaferrites, which may contain low-conductivity grains separated by higher-resistivity grain boundaries as proposed by Koops [15].

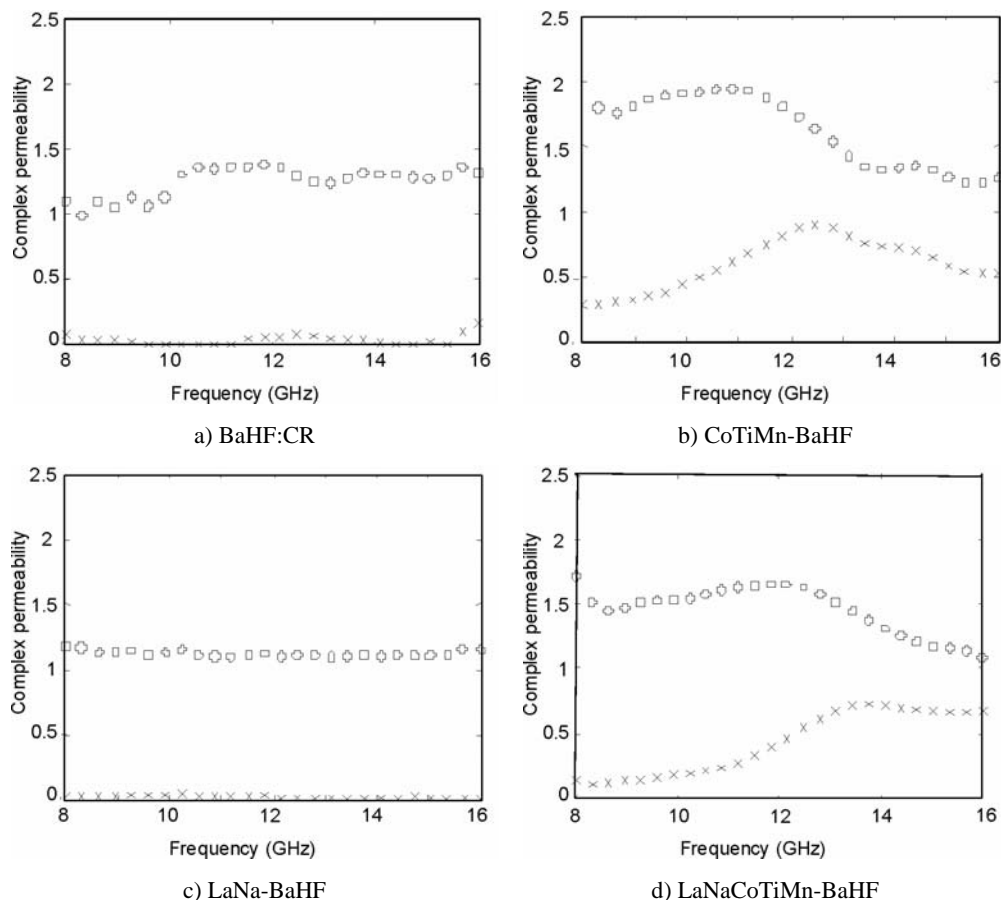


Fig. 5. Dispersion of real (μ' , 0) and imaginary parts (μ'' , X) of the complex permeability of doped barium hexaferrite:polychloroprene composites

As seen in Figure 5, addition of dopants results in changes in magnetic resonance as compared to the composite BaHF:CR (Fig. 5a), which is illustrated by variations in the values of μ' and μ'' .

Reflection losses of doped and undoped hexaferrites are shown in Figure 6. Ferrites absorb microwaves at different frequencies due to various interactive loss mechanisms, mainly related to magnetization. The greatest microwave absorption for doped barium hexaferrite:polychloroprene composites can be attributed to the reduc-

tion of H_c and increase in permeability values as compared to BaHF:CR which does not absorb in the analyzed frequency range (it absorbs at 45 GHz). The composite

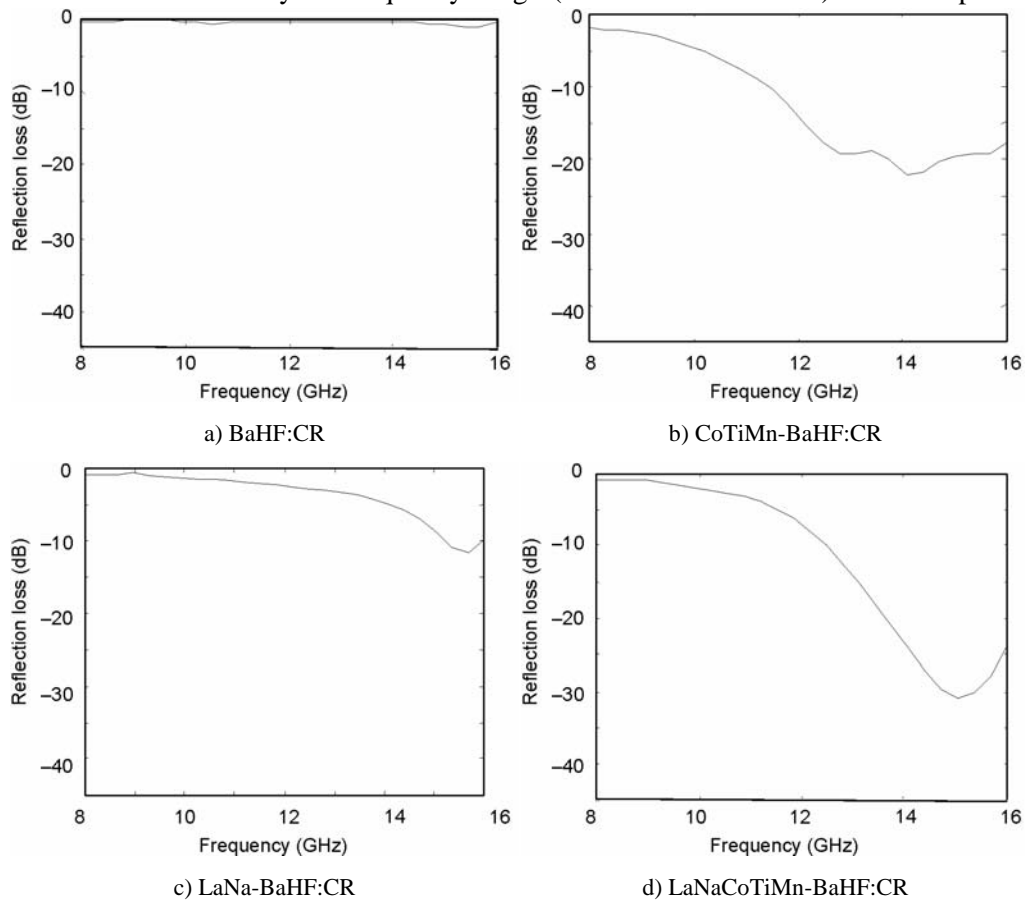


Fig. 6. Reflection loss (dB) of doped barium hexaferrite:polychloroprene composites, thickness 1.5 mm

LaNa-BaHF:CR shows the poorest microwave absorption, which can be attributed to the presence of hematite. The presence of this second phase may be responsible for the disappearance of magnetic resonance and for the increase in the values of ϵ'' (Fig. 4c). The CoTiMn-BaHF:CR composite (80:20) exhibits a reflection loss smaller than -10 dB in the frequency range of 12–16 GHz, whereas the LaNaCoTiMn BaHF:CR composite exhibits the highest microwave absorption (99.9 %) at 15 GHz.

4. Conclusions

Addition of dopants resulted in a reduction in the coercive field and magnetization of barium hexaferrites. Different composites of doped barium hexaferrites:polychlo-

roprene obtained from the substitution of Fe^{3+} and Ba^{2+} can be prepared to be used as microwave absorbers in the frequency range of 8–16 GHz, according to the natural ferrimagnetic resonance illustrated by variations in μ' and μ'' .

Dual substitution of Ba^{2+} and Fe^{3+} , which occurs in the composite 80:20 of LaNaCo-TiMnBaHF:CR, produces a better RAM at 15 GHz, as compared to individual substitutions, with the reflection loss of -30 dB (microwave absorption of about 99.9 %).

References

- [1] CHO H.S., KIM S.S., IEEE Trans. Magn., 35 (1999), 3151.
- [2] MATSUMOTO M., MIYATA Y., J. Appl. Phys., 79 (1996), 5486.
- [3] LI Y., LIU R., ZHANG Z., XIONG C., Mat. Chem. Phys., 64 (2000), 256.
- [4] LIMA R.C., PINHO M.S., GREGORI M.L., NUNES R.C.R., OGASAWARA T., *Effect of different dopants on the microwave properties of M-doped barium hexaferrites*, 8th Conference and Exhibition of the European Ceramic Society, Istanbul, Turkey, 2003.
- [5] ZHANG H., ZHICHAO L., XI Y., Mat. Sci. Eng., B 96 (2002), 289.
- [6] GRÜNBERGER W., SPRINGMANN B., BRUSBERG M., SCHMIDT M., JAHNKE R., J. Magn. Magn. Mat., 101 (1991), 173.
- [7] PINHO M.S., GREGORI M.L., NUNES R.C.R., SOARES B.G., Eur. Polymer J., 38 (2002), 2321.
- [8] PINHO M.S., PhD. Thesis, *Radar Absorbing Materials in Polychloroprene Matrices*, IMA-UFRJ, Rio de Janeiro, Brasil, 2002.
- [9] NEDKOV I., PETKOV A., KARPOV V., IEEE Trans. Magn., 26 (1990), 1483.
- [10] YAMAMOTI H., KAWAGUCHI T., NAGAKURA M., IEEE Trans. Magn., 15 (1979), 1141.
- [11] BAKER-JARVIS J., JANEZIC M.D., GROSVENOR J.H., GEYER R.G., NIST Technical Note, 1355-R (1993), 4.
- [12] GUPTA S.C., AGRAWAL N., J. IETE, 39 (1993), 197.
- [13] SUÁREZ N., SÁNCHEZ J.L., DIAZ S., CUETO A., LÓPEZ G., OÑATE J., *Magnetism, Magnetic Materials and their Applications*, Section III (Part 2), La Habana, Cuba, 1991, pp. 21–29.
- [14] SINGH P., BABBAR V.K., RAZDAN A., SRIVASTAVA S.L., PURI R.K., Mat. Sci. Eng. B, Solid State Mat. Adv. Techn., 67 (1999), 132.
- [15] KOOPS C.G., Phys. Rev., 83 (1951), 121.

Received 16 June 2004

Revised 30 July 2004

Bimetallic complexes with macrocyclic ligands. Variation of magnetic exchange interactions in some heteronuclear thiocyanato-bridged compounds

ALINA TOMKIEWICZ, JULIA KŁAK, JERZY MROZIŃSKI*

Faculty of Chemistry, University of Wrocław, F. Joliot-Curie 14, 50-383 Wrocław, Poland

A series of heterobinuclear, thiocyanato-bridged complexes of macrocyclic ligands of copper(II) and nickel(II) have been characterized by variable-temperature magnetic susceptibility (1.72–300 K). The complexes have the following composition: $(\text{CuL}_1)_3[\text{Fe}(\text{NCS})_6]_2 \cdot 3\text{H}_2\text{O}$ (**1**), $(\text{CuL}_1)[\text{Ni}(\text{NCS})_6] \cdot 2\text{H}_2\text{O}$ (**2**), $(\text{CuL}_1)[\text{Co}(\text{NCS})_4] \cdot 3\text{H}_2\text{O}$ (**3**), where L_1 is 5,12-dimethyl-[14]-1,4,8,11-tetraazacyclotetradeca-4,11-diene and $(\text{NiL}_2)_3[\text{Fe}(\text{NCS})_6]_2 \cdot 2\text{H}_2\text{O}$ (**4**), $(\text{NiL}_2)[\text{Co}(\text{NCS})_4] \cdot 3\text{H}_2\text{O}$ (**5**), $(\text{NiL}_2)_2[\text{Cr}(\text{NCS})_6] \text{ClO}_4$ (**6**), where L_2 is 5,7,12,14-tetramethyl-[14]-1,4,8,11-tetraazacyclotetradeca-4,11-diene. The results indicate that all of them behave as weakly interacting magnets.

Key words: *bimetallic complexes; copper (II); nickel (II); macrocyclic complex*

1. Introduction

The search for new materials exhibiting useful magnetic and magneto-optical properties is one of the main goals of molecular magnetism studies [1]. To design molecular systems with a desired magnetic behaviour, it is necessary to use a novel compound which contains several kinds of metallic ions, organic ligands and novel bridging networks.

The strategies derived from understanding the underlying phenomena play an important role in the syntheses of such compounds. For example, the spin transition phenomena which occur in some transition metal complexes is a spectacular example of molecular bistability [2].

In molecular magnetism, two kinds of molecular magnetisms of isolated molecules and assemblies of molecules can be specified. These molecules may contain one or more

*Corresponding author, e-mail: jmroz@wchuwr.chem.uni.wroc.pl.

magnetic centres. They can also be built from molecular precursors, specially chosen to achieve a 3D covalent bonding network between spin bearing species [3].

One of the simplest and most convenient molecular building blocks is found in the hexacyanometallate family $[B(CN)_6]^{n-}$. When $[B(CN)_6]^{n-}$ reacts with labile $[A(H_2O)_6]$ assembling ions (A and B are metallic ions), tridimensional systems result, which are analogues of the Prussian blue family.

The literature covering an analogous system, in which the thiocyanate group plays the role of a bridging ligand, is much more scarce [4]. Due to its ambident character, the thiocyanate group can serve as a bridging ligand, similarly to the cyanide group. There are a few heterometallic compounds of the type $[CuL]_3[Cr(NCS)_6]_2 \cdot nH_2O$ (L = 2,2-bipyridine, $n = 0$; L = *o*-phenanthroline, $n = 1$; L = diethylenetriamine, $n = 1$) [5]; $[CuL_4]_3[Cr(NCS)_6]_2 \cdot nH_2O$; (L = imidazole, $n = 2$ [6]; $[Cu(en)_2Mn(NCS)_4(H_2O)_2]_n$ (en = ethylenediamine) [7].

The number of such investigations has increased recently, due to the introduction of appropriate ligands of the macrocyclic type [8].

Francese et al. [4] were the first who used a simple macrocyclic copper(II) complex $Cu(cyclam)^{2+}$ to obtain a heterometallic system bridged by a thiocyanate group. Square-planar tetraazamacrocyclic complexes of Cu^{II} and Ni^{II} with two free coordination places at the metal atom can play the role of "building blocks" in this case [9]. There is a good access to the metal ion when there are no substituents in the macrocyclic ring. The situation changes with the size and character of the substituents which may form a steric hindrance and prevent any coordination to the metal ion.

In this paper, we present results concerning systems containing unsaturated substituted complexes of copper(II) (Fig. 1) and nickel(II) (Fig. 2) and simple ions such as $[Ni(NCS)_6]^{4-}$, $[Co(NCS)_4]^{2-}$, $[Fe(NCS)_6]^{3-}$, and $[Cr(NCS)_6]^{3-}$.

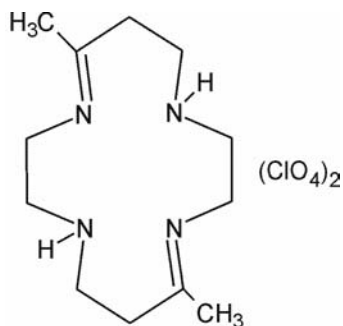


Fig. 1. Schematic view of 5,12-dimethyl-1,4,8,11-tetraazacyclotetradeca-4,11-diene diperchlorate (L_1)

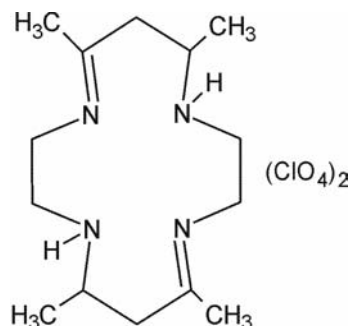


Fig. 2. Schematic view of 5,7,12,14-tetramethyl-1,4,8,11-tetraazacyclotetradeca-4,11-diene diperchlorate (L_2)

It was interesting to verify whether the configuration of the nitrogen donor atoms and the kind of metal ions influences the crystalline structure or magnetic properties of the complexes.

2. Experimental

2.1. Materials. All chemicals were of reagent grade and were used as commercially obtained. $[\text{CuL}_1](\text{ClO}_4)_2$ [10], $[\text{NiL}_2](\text{ClO}_4)_2$ [11], $[(\text{C}_4\text{H}_9)_4\text{N}]_2[\text{Co}(\text{NCS})_4]$ [12], $[(\text{C}_4\text{H}_9)_4\text{N}]_3[\text{Ni}(\text{NCS})_6]$, $[(\text{C}_4\text{H}_9)_4\text{N}]_3[\text{Cr}(\text{NCS})_6]$ and $[(\text{C}_4\text{H}_9)_4\text{N}]_3[\text{Fe}(\text{NCS})_6]$ [12–14] were prepared following the methods described in literature.

Synthesis of complexes: The complexes, $(\text{CuL}_1)_3[\text{Fe}(\text{NCS})_6]_2 \cdot 3\text{H}_2\text{O}$ (**1**), $(\text{CuL}_1)[\text{Ni}(\text{NCS})_6] \cdot 2\text{H}_2\text{O}$ (**2**), $(\text{CuL}_1)[\text{Co}(\text{NCS})_4] \cdot 3\text{H}_2\text{O}$ (**3**), $(\text{NiL}_2)_3[\text{Fe}(\text{NCS})_6]_2 \cdot 2\text{H}_2\text{O}$ (**4**), $(\text{NiL}_2)[\text{Co}(\text{NCS})_4] \cdot 3\text{H}_2\text{O}$ (**5**), and $(\text{NiL}_2)_2[\text{Cr}(\text{NCS})_6]\text{ClO}_4$ (**6**), were prepared by the methods described below.

The complexes **2**, **3**, and **5** were obtained by adding 10 ml of CH_3CN solution containing 0.3 mmol of $[(\text{C}_4\text{H}_9)_4\text{N}]_2[\text{M}(\text{NCS})_6]$ to 20 ml of CH_3CN solution containing 0.3 mmol of the appropriate ligand ($[\text{CuL}_1](\text{ClO}_4)_2$ or $[\text{NiL}_2](\text{ClO}_4)_2$) at room temperature. The solutions were stirred continuously. The resulting precipitate was filtered off, washed with CH_3CN and $\text{C}_2\text{H}_5\text{OH}$ solutions, and dried over P_2O_5 .

Elemental analysis calculated for $\text{C}_{18}\text{H}_{34}\text{N}_8\text{S}_4\text{NiCo}$ (656.43) (**5**): C, 32.93; H, 5.23; N, 17.07; S, 19.54%. Found: C, 31.25; H, 4.84; N, 16.41; S, 18.97%.

Elemental analysis calculated for $\text{C}_{16}\text{H}_{30}\text{N}_8\text{S}_4\text{CuCo}$ (633.21) (**3**): C, 30.35; H, 4.78; N, 17.70; S, 19.45%. Found: C, 31.73; H, 4.13; N, 17.72; S, 19.02%.

Elemental analysis calculated for $\text{C}_{18}\text{H}_{28}\text{N}_{10}\text{S}_6\text{CuNi}$ (731.13) (**2**): C, 29.57; H, 3.87; N, 19.16; S, 19.11%. Found: C, 29.39; H, 4.31; N, 18.12; S, 19.01%.

The compounds **1**, **4**, and **6** were obtained by adding 15 ml of CH_3CN solution containing 0.5 mmol of $[(\text{C}_4\text{H}_9)_4\text{N}]_3[\text{M}(\text{NCS})_6]$ to 25 ml of CH_3CN solution containing 0.3 mmol of the appropriate ligand ($[\text{CuL}_1](\text{ClO}_4)_2$ or $[\text{NiL}_2](\text{ClO}_4)_2$) at room temperature. The solutions were stirred continuously. The resulting precipitate was filtered off, washed with CH_3CN and $\text{C}_2\text{H}_5\text{OH}$ solutions, and dried over P_2O_5 .

Elemental analysis calculated for $\text{C}_{48}\text{H}_{78}\text{N}_{24}\text{S}_{12}\text{Cu}_3\text{Fe}_2$ (1726.44) (**1**): C, 33.39; H, 4.55; N, 19.47; S, 21.50%. Found: C, 32.44; H, 3.95; N, 18.77; S, 20.21%.

Elemental analysis calculated for $\text{C}_{54}\text{H}_{88}\text{N}_{24}\text{S}_{12}\text{Ni}_3\text{Fe}_2$ (1778.02) (**4**): C, 36.48; H, 4.87; N, 18.91; S, 21.64%. Found: C, 36.28; H, 4.80; N, 18.32; S, 20.21%.

Elemental analysis calculated for $\text{C}_{34}\text{H}_{28}\text{N}_{14}\text{S}_6\text{Ni}_2\text{Cr}$ (1122.11) (**6**): C, 40.89; H, 5.03; N, 17.47; S, 17.14%. Found: C, 41.63; H, 5.34; N, 16.71; S, 17.25%.

Physical techniques. Magnetic measurements in the temperature range of 1.7–300 K were performed using a Quantum Design SQUID-based MPMSXL-5-type magnetometer. The SQUID magnetometer was calibrated with a palladium rod sample (Materials Research Corporation, of the purity 99.9985%). Measurement samples of the compounds under study were made at the magnetic field of 0.5 T. Corrections are based on subtracting the sample holder signal and contribution from χ_D estimated from the Pascal constants [15].

The FIR spectra were recorded in Nujol mulls ($500\text{--}100\text{ cm}^{-1}$), and the MIR spectra in KBr pellets ($4000\text{--}500\text{ cm}^{-1}$), with a Brucker IFS 113V Spectrophotometer.

3. Results and discussion

A major task in understanding magnetic exchange interactions is to sort out various effects of molecular and electronic structure on coupling parameters. Our approach has been to control the molecular structures to an extent as great as possible and to simultaneously vary electronic properties of the paramagnetic centres.

Initially, we reported the magnetic exchange interactions for complexes **1**, **2**, and **3** which contain the same symmetric macrocyclic ligands with different metal ions.

The magnetic properties of complex **1** as temperature dependencies of χ_M and $\chi_M T$ (χ_M being the molar magnetic susceptibility) are shown in Figure 3.

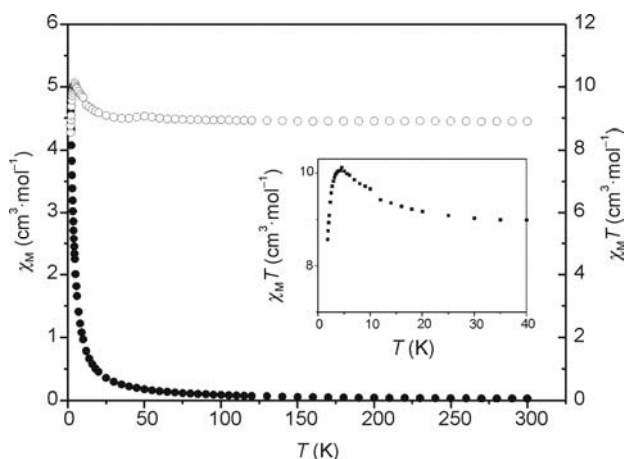


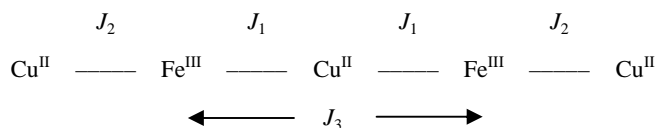
Fig. 3. Temperature dependence of the magnetic susceptibility χ_M (full symbols) and $\chi_M T$ (empty symbols) for the compound $(\text{CuL}_1)_3[\text{Fe}(\text{NCS})_6]_2 \cdot 3\text{H}_2\text{O}$ (**1**).

The inset shows the low temperature region of $\chi_M T$ vs. T

At room temperature, $\chi_M T$ for this complex is $8.95 \text{ cm}^3 \cdot \text{mol}^{-1} \cdot \text{K}$ ($\mu_{\text{eff}} = 8.47 \text{ B.M.}$). Such a value corresponds to that calculated for two high-spin Fe^{III} ions and three Cu^{II} ions which are antiferromagnetically coupled. The values of the constants C and Θ , determined from the relation $1/\chi_M$ vs. T over the 300–100 K temperature range, are equal to $8.93 \text{ cm}^3 \cdot \text{mol}^{-1} \cdot \text{K}$ and 0.40 K , respectively. The $\chi_M T$ value remains nearly constant at a wide range of temperatures, and increases upon cooling below 50 K. It reaches a maximum at 4.5 K, with $\chi_M T = 10.1 \text{ cm}^3 \cdot \text{mol}^{-1} \cdot \text{K}$ ($\mu_{\text{eff}} = 9.00 \text{ B.M.}$), and finally decreases rapidly for temperatures below 4.5 K.

The presence of a maximum in the $\chi_M T$ curve is indicative of ferromagnetic coupling between unpaired electrons at Fe^{III} magnetic centres. From the magnetic point of view, this compound will thus be considered as a linear pentamer. The variation of susceptibility with temperature for $[\text{Cu}^{\text{II}}\text{Fe}^{\text{III}}\text{Cu}^{\text{II}}\text{Fe}^{\text{III}}\text{Cu}^{\text{II}}]$ should be calculated using the formula for χ_M with five linearly coupled spins. Two of these spins – J_1 , J_2 – represent the exchange interactions between adjacent iron and copper ions, and the spin J_3

describes the interaction between the iron nuclei within the pentamer complex, shown pictorially as follows:



Based on our previous paper [16] and the well known crystal structure of $(\text{NiL})_3[\text{Fe}(\text{NCS})_6]_2$, where $L = 5,6,12,13\text{-Me}_4\text{-[14]-4,11\text{-dieneN}_4$, we suggest that the exchange interaction between Cu^{II} and Fe^{III} ions is transmitted by the thiocyanate groups. The environment of the Fe^{III} ion is octahedral, while the thiocyanate groups are nearly linear. Each Fe^{III} ion is bound to two copper(II) ions. The thiocyanate groups coordinate to the copper(II) ions by their sulphur atom. A proposed schematic view of complex **1** is presented in Figure 4.

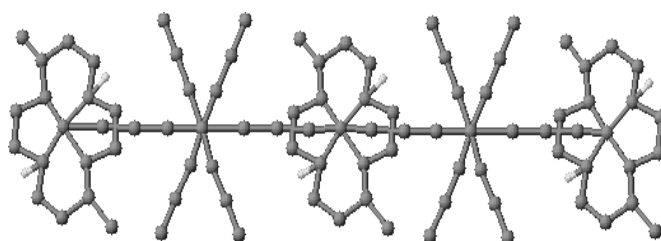


Fig. 4. A schematic view of $(\text{CuL}_1)_3[\text{Fe}(\text{NCS})_6]_2 \cdot 3\text{H}_2\text{O}$ (**1**)

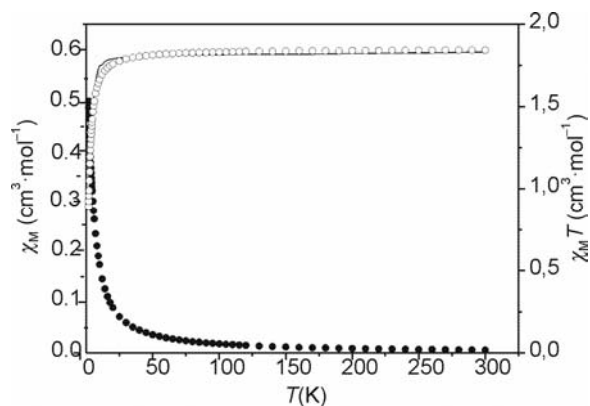


Fig. 5. Temperature dependence of magnetic susceptibility χ_M (full symbols) and $\chi_M T$ (empty symbols) for the compound $(\text{CuL}_1)[\text{Ni}(\text{NCS})_6] \cdot 2\text{H}_2\text{O}$ (**2**).

The solid line represents the least squares fit or the theoretical Eq. (1) to the experimental data

The magnetic susceptibility data for complex **2** are shown in Fig. 5. An antiferromagnetic exchange interaction is present as indicated by the fact that the value of $\chi_M T$

decreases very slowly in a wide range of temperatures and rapidly decreases below 30 K. When there is no magnetic exchange interaction in Cu^{II}-Ni^{II} binuclear compounds, the paramagnetic susceptibilities of the two different metal centres add up to the paramagnetic susceptibility of the binuclear complex. Consequently, the expected spin only value of μ_{eff} for the Cu^{II}-Ni^{II} compound, in absence of an exchange interaction, would be 3.83 B.M.

An antiferromagnetic exchange interaction in the Cu^{II}-Ni^{II} binuclear complex leads to an $S = 1/2$ ground state with an $S = 3/2$ excited state. The observed value of μ_{eff} per binuclear complex is 3.83 B.M. at 300 K which indicates that most of the molecules are in the $S = 3/2$ state. Below ca. 30 K there is a more pronounced decrease of μ_{eff} with decreasing temperature, which most likely reflects antiferromagnetic interactions and zero field effects for the Ni^{II} ion.

The data for compound **2** were initially fit to the susceptibility expression (Eq. (1)) derived from the simple spin Hamiltonian

$$\hat{H} = -2J\hat{S}_1\hat{S}_2$$

$$\chi_M = \frac{N\beta^2}{4kT} \left[\frac{g_{1/2}^2 + 10g_{3/2}^2 \exp(3J/kT)}{1 + 2\exp(3J/kT)} \right] \quad (1)$$

$$g_{1/2} = \frac{4g_{\text{Ni}} - g_{\text{Cu}}}{3}; \quad g_{3/2} = \frac{2g_{\text{Ni}} + g_{\text{Cu}}}{3}$$

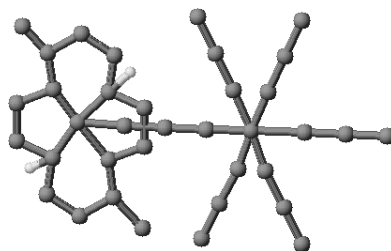


Fig. 6. A schematic view of (CuL₁)[Ni(NCS)₆]·2H₂O (**2**)

A least squares fit of Eq. (1) to the data gave $J = -1.87 \text{ cm}^{-1}$, $g_{\text{Cu}} = 2.20$, and $g_{\text{Ni}} = 2.36$ ($R = 3.07 \times 10^{-4}$). A small and negative value of the exchange parameter confirms weak antiferromagnetic interaction in complex **2** transmitted by the thiocyanato group (Fig. 6).

The $\chi_M T$ plots for complex **3** are shown in Figure 7. At room temperature, $\chi_M T$ is $2.96 \text{ cm}^3 \cdot \text{mol}^{-1} \cdot \text{K}$ (4.87 B.M.), which is slightly larger than expected for copper(II) ($S = 1/2$) and cobalt(II) ($S = 3/2$) ions. The value of $\chi_M T$ is independent of temperature in the range of 50–300 K, but gradually decreases at lower temperatures. The $1/\chi_M$ vs. T plots in the range of 15–300 K obey the Curie–Weiss law with small and negative Weiss constant: $\Theta = -0.34 \text{ K}$ and $C = 2.95 \text{ cm}^3 \cdot \text{mol}^{-1}$.

The interaction of cobalt(II) with copper(II) gives rise to low-lying spin triplet and spin quintet states, separated by $2J$. The decrease of $\chi_M T$ upon cooling would be expected for high-spin Co^{II} , which interacts antiferromagnetically with Cu^{II} ions through the thiocyanato bridge.

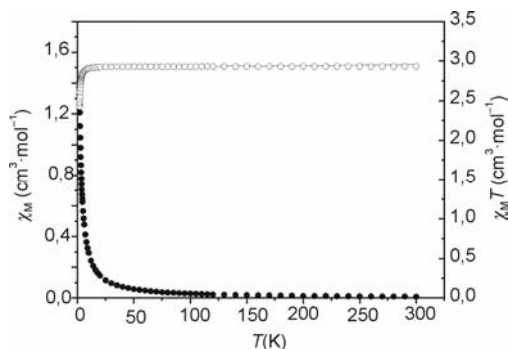


Fig. 7. Temperature dependence of magnetic susceptibility χ_M (full symbols) and $\chi_M T$ (empty symbols) for the compound $(\text{CuL}_1)[\text{Co}(\text{NCS})_4] \cdot 3\text{H}_2\text{O}$ (**3**). The solid line represents the least squares fit of the theoretical equations (2)–(4) to the experimental data

The attenuation of μ_{eff} as the temperature of the sample approaches 1.80 K is most pronounced for the complex **3** which agrees with the expectation that the Co^{II} ion would exhibit the greatest zero-field splitting. The data for compound **3** were fit to Equations (2)–(4) using the least squares method:

$$\chi_{\parallel} = \frac{2N\beta^2}{kT} \left[\frac{g_1^2 \exp(-D/kT) + 5g_2^2 \exp(2J/kT)}{1 + 2\exp(-D/kT) + 5(2J/kT)} \right] \quad (2)$$

$$\chi = 2N\beta^2 \frac{\frac{g_1^2}{D} [1 - \exp(-D/kT)] + \frac{5g_2^2}{kT} \exp(2J/kT)}{1 + 2\exp(-D/kT) + 5\exp(2J/kT)} \quad (3)$$

$$g_1 = \frac{5g_{\text{Co}} - g_{\text{Cu}}}{4}, \quad g_2 = \frac{3g_{\text{Co}} + g_{\text{Cu}}}{4}$$

$$D_1 = \frac{3D_{\text{Co}}}{2} - \frac{D_{\text{CuCo}}}{4}$$

$$\chi_{\text{av}} = 13\chi_{\parallel} + 23\chi_{\perp} \quad (4)$$

The best fit gave $g_{\text{Cu}} = 2.20$, $g_{\text{Co}} = 2.30$, $J = -0.9 \text{ cm}^{-1}$, and $D = 2.5 \text{ cm}^{-1}$ ($R = 8.88 \times 10^{-5}$), as indicated by the solid curve in Fig 7. A small and negative value of

the exchange parameter suggests a very weak antiferromagnetic interaction between Cu^{II} and Co^{II} ions. A relatively large value of g for this $\text{Cu}^{\text{II}}\text{-Co}^{\text{II}}$ complex is somewhat in line with the average value of g quoted for square-pyramidal complexes.

Our previous crystallographic results concerned similar compounds, namely $(\text{CuL})[\text{Co}(\text{NCS})_4]$, with $\text{L} = \text{N-rac-(5,12-Me}_2\text{-7,14-Et}_2\text{-[14]-4,11-dieneN}_4)$ [17]. Those results allow us to suggest that the asymmetric unit of the complex **3** consists of an $[\text{Co}(\text{NCS})_4]^{2-}$ anion and a $\text{N-rac}[\text{CuL}_1]^{2+}$ cation, bridged by a thiocyanate ligand. One of the Cu^{II} ion coordination sites is blocked by the axial methyl group. Therefore, it forms the distorted square-pyramidal structure of the complex **3**, with four equatorial nitrogen atoms of macrocyclic ligand and one sulfur atom from the thiocyanato bridging group in an axial position. The coordination geometry around the Co ion is distorted tetrahedrally. The cobalt(II) centre possesses one bridging and three non-bridging thiocyanate ligands. The proposed schematic structure of the complex **3** is presented in Fig. 8.

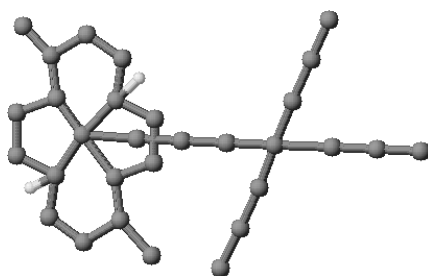


Fig. 8. A schematic view of $(\text{CuL}_1)[\text{Co}(\text{NCS})_4]\cdot 3\text{H}_2\text{O}$ (**3**)

The series of heterobinuclear complexes, containing the same symmetric macrocyclic ligand with different metal ions, were characterized by variable-temperature magnetic susceptibility. The trend observed in this series of complexes is a change of magnetic interactions due to the number of unpaired metal ion electrons. This suggests the occurrence of both ferro (F) and antiferromagnetic (AF) interactions in the examined compounds with heterometallic cores. We assumed that the F interaction is stronger than the AF interaction in complex **1**, in contrast to compounds **2** and **3**.

The second series of the compounds contained the metal within the ligand with more substituents. We attempted to verify whether the configuration at the nitrogen atoms influence the magnetic properties.

The magnetic properties of complexes **4**, **5**, and **6** are illustrated in Figure 9.

The values of $\chi_M T$ at room temperature are $8.54 \text{ cm}^3 \cdot \text{mol}^{-1} \cdot \text{K}$ (8.27 B.M.) for complex **4**, $1.65 \text{ cm}^3 \cdot \text{mol}^{-1} \cdot \text{K}$ (3.64 B.M.) for complex **5**, and $1.64 \text{ cm}^3 \cdot \text{mol}^{-1} \cdot \text{K}$ (3.62 B.M.) for complex **6**, all of which are expected for paramagnetic ions. The $\chi_M T$ versus T values remain nearly constant for all compounds in a wide range of temperatures and rapidly decrease at the lowest temperatures. A slight decrease in $\chi_M T$ may be due to either the effect of zero-field splitting parameters for the metal ions or/and intermolecular ex-

change interactions between paramagnetic centres. The constants C and Θ were determined from the relation $1/\chi_M$ vs. T over the temperature range of 300–100 K. The results are presented in Table 1.

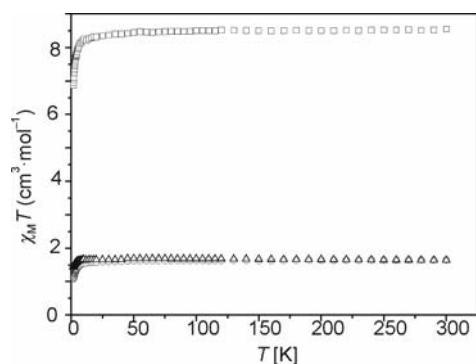


Fig. 9. Temperature dependence of $\chi_M T$ for: (□) $(\text{NiL}_2)_3[\text{Fe}(\text{NCS})_6]_2 \cdot 2\text{H}_2\text{O}$ (**4**); (○) $(\text{NiL}_2)[\text{Co}(\text{NCS})_4] \cdot 3\text{H}_2\text{O}$ (**5**); (Δ) $(\text{NiL}_2)_2[\text{Cr}(\text{NCS})_6]\text{ClO}_4$ (**6**)

A small negative value of Θ shows weak antiferromagnetic exchange interactions between each pair of metal ions.

Table 1. Curie constant, Weiss constant and magnetic moment of the investigated compounds

Compound	Curie constant C [$\text{cm}^3 \cdot \text{K} \cdot \text{mol}^{-1}$]	Weiss constant θ [K]	Magnetic moment at 300 K [M.B.]
$(\text{NiL}_2)_3[\text{Fe}(\text{NCS})_6]_2 \cdot 2\text{H}_2\text{O}$ (4)	8.547	-0.66	8.27
$(\text{NiL}_2)[\text{Co}(\text{NCS})_4] \cdot 3\text{H}_2\text{O}$ (5)	1.662	-1.89	3.64
$(\text{NiL}_2)_2[\text{Cr}(\text{NCS})_6]\text{ClO}_4$ (6)	1.619	-1.90	3.62

For a system consisting of three Ni^{II} ions ($S = 3 \times 1$) and two Fe^{III} ions ($S = 2 \times 5/2$) (**4**), the calculated value of magnetic moment at room temperature suggests that two terminal Ni^{II} ions are diamagnetic [16], which is a configuration in which the low-spin electronic configuration for this ion occurs. From the magnetic point of view, this compound will thus be considered as a linear FeNiFe core.

In the case of the two latter compounds (**5**, **6**), the magnetic moment at room temperature confirms the diamagnetic character of the Ni^{II} ions. The magnetism of this compound should originate from the Co^{II} (**5**) and Cr^{III} (**6**) ions only. A decrease in $\chi_M T$ for both compounds will be thus caused by antiferromagnetic interaction between Co^{II} (**5**) and Cr^{III} (**6**) ions in the crystal lattice and by the zero-field splitting factor.

The compounds obtained in series 1 and 2 display an analogous composition, suggesting structural similarity. However, the results obtained from magnetic studies contradict this suggestion.

This fact is undoubtedly linked to a change in the number of methyl substituents in the macrocyclic ligands L_1 and L_2 and to a change in the N-configuration of six-membered chelating ring. An increase in the number of substituents results in a bigger steric hindrance during the coordination of the thiocyanate group to nickel(II) or copper(II) ions and caused by a different packing in the crystal lattice and a different mutual arrangement of the magnetic centres.

Although the crystal structures of the examined compounds have not been fully elucidated, some essential conclusions result from the IR spectra.

For the compound $(NiL_2)[Co(NCS)_4] \cdot 3H_2O$ (**5**), a single sharp band was observed in the $4000\text{--}500\text{ cm}^{-1}$ spectrum, situated at 2056 cm^{-1} and originating from the stretching vibration $\nu(CN)$. No band is observed in the spectrum of this compound above 2100 cm^{-1} . This suggests the presence of a non-bridging thiocyanato ligand and appearance of electrostatic interactions between the macrocyclic cation $[NiL_2]^{2+}$ and anion $[Co(NCS)_6]^{2-}$ in the complex (**5**).

The infrared spectra of the complexes $(CuL_1)_3[Fe(NCS)_6]_2 \cdot 3H_2O$ (**1**) (2062 cm^{-1} and 2154 cm^{-1}), $(CuL_1)[Ni(NCS)_6] \cdot 2H_2O$ (**2**) (2078 cm^{-1} and 2121 cm^{-1}), $(CuL_1)[Co(NCS)_4] \cdot 3H_2O$ (**3**) (2059 cm^{-1} and 2074 cm^{-1}), $(NiL_2)_3[Fe(NCS)_6]_2 \cdot 2H_2O$ (**4**) (2046 cm^{-1} and 2093 cm^{-1}), and $(NiL_2)_2[Cr(NCS)_6] ClO_4$ (**6**) (2076 cm^{-1} and 2121 cm^{-1}) exhibit two bands near 2000 cm^{-1} corresponding to the $\nu_1(NCS)$ stretching mode. Additionally, bands above 2100 cm^{-1} are observed in the spectra of all the compounds, indicating the presence of a bridging thiocyanate group. This feature results from a combination of three effects: (a) the presence of a bridging thiocyanate ligand, (b) the presence of a non-bridging thiocyanate ligand, (c) the distorted environments of the metals cobalt (II), iron (III), chromium (III), nickel (II), and copper (II).

Acknowledgements

This work was financially supported by the Polish State Committee for Scientific Research, Grant No. 4 T09A 115 23.

References

- [1] FERLAY S., MALLAH T., OUAHÉS R., VEILLET P., VERDAGUER M., *Nature*, 378 (1995), 701.
- [2] KAHN O., *Molecular Magnetism*, VCH, New York, 1993.
- [3] MALLAH T., FERLAY S., AUBERGER C., HÉLARY C., L' HERMITE F., OUAHÉS R., VAISSERMANN J., VERDAQUER M., VEILLET P., *Mol. Crys. Liq. Cryst.*, 273 (1995), 141.
- [4] FRANCESE G., FERLAY S., SCHMALLE H.W., DECURTINS S., *New J. Chem.*, 180 (1999), 267.
- [5] SMÉKAL Z., BŘEZINA F., ŠINDELÁŘ Z., KLIČKA R., NÁDVORNIK M., *Transition Met. Chem.*, 22 (1997), 299.
- [6] DOBRZAŃSKA L., WRZESZCZ G., GRODZICKI A., ROZPŁOCH F., *Polish J. Chem.*, 14 (2000), 199.
- [7] KOU H.Z., LIAO D.Z., CHENG P., JIANG Z.H., YAN S.P., WANG G.L., YAO X.K., WANG H.G., *Can. J. Chem.*, 76 (1998), 1102.
- [8] FABBRIZZI L., FORLINI F., PEROTTI A., SEGHI B., *Inorg. Chem.*, 23 (1984), 807.
- [9] MROZIŃSKI J., KOLIŃSKI R.A., *Chem. Zvesti*, 35 (1981), 785.
- [10] JEŻOWSKA-TRZEBIATOWSKA B., KOLIŃSKI R., KORYBUT-DASZKIEWICZ B., MROZIŃSKI J., WOJCIECHOWSKI W., *Bull. Acad. Polon. Sci., Ser. Sci. Chim.*, 17 (1969), 7.

- [11] JEŻOWSKA-TRZEBIATOWSKA B., KOLIŃSKI R., KORYBUT-DASZKIEWICZ B., MROZIŃSKI J., WOJCIECHOWSKI W., Bull. Acad. Polon. Sci., Ser. Sci. Chim., 17 (1969), 14.
- [12] SABATINI A., BERTINI I., Inorg. Chem, 4 (1965), 959.
- [13] FORSTER D., GOODGAME D.M.L., J. Chem. Soc. (1965), 268.
- [14] HAY R.W., PIPLANI D.P., JERAGH B., J. Chem. Soc. Dalton Trans., 1951 (1977)
- [15] BRISCOE H.V.A., ROBINSON P.L., RUDGE A.J., J. Chem. Soc., 3219 (1931)
- [16] SKORUPA A., KORYBUT-DASZKIEWICZ B., MROZIŃSKI J., Inorg. Chem. Acta, 336 (2002), 65.
- [17] SKORUPA A., KORYBUT-DASZKIEWICZ B., MROZIŃSKI J., Inorg. Chem. Acta, 324 (2002), 286.

Received 15 July 2004

Revised 2 August 2004

Investigations of the surface morphology of Al₂O₃ layers by atomic force microscopy

WŁADYSŁAW SKONECZNY^{1*}, JAN JURUSIK², ANDRZEJ BURIAN³

¹Chair of Materials Science, University of Silesia, ul Śnieżna 2, 41-200 Sosnowiec, Poland

²Centre of Polymer Chemistry, Polish Academy of Sciences,
ul. M. Skłodowskiej-Curie 34, 41-819 Zabrze, Poland

³Institute of Physics, University of Silesia, ul. Uniwersytecka 4, 40-007 Katowice, Poland

Amorphous alumina coating films, prepared on aluminium substrates by oxidation by the electrolytic method in ternary electrolytes, have been characterised by atomic force microscopy. The surface roughness and growth structure of the obtained Al₂O₃ films are related to the experimental conditions: temperature, current density, and deposition time. They are also related to the preparation method of the aluminium substrate surface. The columnar growth revealed by atomic force microscopy, with shape and size of columns depending on temperature and current density, has been confirmed by scanning electron microscopy.

Key words: *alumina coating films; atomic force microscopy (AFM); scanning electron microscopy; X-ray diffraction; tribological properties*

1. Introduction

Although properties of Al₂O₃ seem to be well known, alumina has been extensively studied both in the bulk and thin film forms [1] because of its possible applications. These are ranging from microelectronics, optical applications, and wear-resistant coatings to decorative purposes on massive aluminium. Thin films of alumina can be prepared by various deposition methods, e.g., evaporation [2, 3], sputtering [4], binary reaction sequence chemistry [5], and also by direct anodic oxidation of aluminium surfaces [6, 7]. An interesting feature of the thin films, both crystalline and amorphous, is that they often exhibit pronounced internal growth structure [8], which evolves during the growth (deposition) process and projects onto the film surface,

*Corresponding author, e-mail: skoneczn@us.edu.pl.

giving rise to film surface topography and roughness. It is also well known that such structural features affect physical properties of thin films [8]. Therefore, properties of produced films can be controlled by an appropriate selection of the preparation method and conditions, e.g., chemical composition of the electrolyte and other parameters such as temperature and current density in the case of an anodizing preparation process. Tribological properties of alumina coatings used as the sliding connections are of great interest in practice. Thin oxide films, formed on the aluminium substrate by direct contact with oxygen, are inapplicable due to unsatisfactory mechanical properties [9]. A special surface treatment with electrolytes is therefore necessary to improve these properties, allowing the Al_2O_3 films to be extensively used in various industries: anti-corrosive protection, protective and decorative coatings, primer layers; elements of clutches, transmission gears, shears, and guides; elements of automatic equipment and hydraulic controllers; raceways of rolling bearings in pairs; pistons of engines and cylinder bearing surfaces in compressors [1].

Oxide films obtained by carefully performed anodic oxidation of aluminium exhibit a significant adhesion which makes the separation of the layer from the substrate practically impossible. They also exhibit high porosity resulting in the ability to absorb considerable quantities of lubricants, and in a great hardness ensuring a high wearability. A thin sliding film of polytetrafluoroethylene-graphite can be easily obtained on a coating prepared in such a way, which is important in terms of the friction properties of these connecting elements [1].

In this paper, studies of the surface morphology of alumina coating films by atomic force microscopy (AFM) are described. The obtained results are related to those obtained by X-ray diffraction (XRD) and scanning electron microscopy (SEM).

2. Experimental details and characterization of the films

Hard anodic treatment in water solutions of sulphuric and oxalic acids is usually used to produce thin Al_2O_3 layers. Anodising in H_2SO_4 solution is performed at the electrolyte temperature of 264–281 K, with concentration up to 20%, and anodic current density of 1 A/dm^2 . In the case of $(\text{COOH})_2$ solution, the anodising parameters are: temperature 275–279 K, concentration up to 5%, anodic current density 1–3 A/dm^2 . A great amount of heat is released in the oxide coating during oxidation from the exothermic chemical reaction of aluminium oxide formation and from the electric current. This heat has to be removed very quickly from the surface of the anodised object, otherwise the coating overheats. As a result of the overheating, tribological properties of the alumina layer are degraded and the coating becomes wear unresistant. This is a serious disadvantage of hard anodic treatment, complicating the formation of alumina coating films. This disadvantage can be overcome by appropriate changes in the chemical composition of the electrolyte.

In the present work a method of hard anodic treatment at higher temperatures has been developed [1, 9]. It does not require cooling, the heat being used to control the

quality of the surface oxide layer and its properties. By anodizing at the appropriate amount of electrolyte, related to the surface area, oxidation without additional carrying away the heat is possible. According to the method proposed here, the oxidation was carried out in a ternary water electrolyte of sulphuric, adipic and oxalic acids (SAO). The temperature of the electrolyte during oxidation was in the range of 293–313 K, whereas the anodic current density was in the range of 2–4 A/dm^2 . Under these conditions the oxidation process can be started at room temperature.

A TopoMetrix Explorer Atomic Force Microscope was used in the contact mode to study the morphology and roughness of thin films. Atomic force microscopy (AFM) images were obtained using a commercially available Si_3N_4 V-shape cantilever (force constant – 0.032 N/m) with a tip radius < 50 nm (Topometrix SFM probe model 1520-00). Forces of a couple of nN are used in contact mode AFM. There are two imaging methods in the contact mode AFM. The most common method of obtaining contact mode AFM images is the constant force method. In this method, the correction voltage for z -piezo restoring the cantilever to its original deflection is used as the z -data for imaging the sample surface topography (constant force or topography image). In the variable force method, the photo-sensor output (from deflection of the cantilever) is used as the z -data for obtaining a constant height (variable deflection) image.

The results of surface topography presented here were obtained in the “constant force” mode. Practically, however, the load force varies during surface scanning and the cantilever deflection photo-sensor output “error signal” was used to acquire error signal image simultaneously with topographical imaging. The AFM topographic images shown in this paper were neither filtered nor corrected.

In order to test the crystallinity of the obtained Al_2O_3 films, X-ray diffraction measurements were made with a Siemens DS 2000 powder diffractometer, using Ni filtered $\text{Cu}_{\text{K}\alpha}$ radiation and a scintillation counter. The X-ray diffraction patterns were recorded in a 2θ angular range from 5 to 80 deg in a symmetrical reflection mode. The structures of cross-sections of Al_2O_3 films were also studied by Scanning Electron Microscopy (SEM) using a Philips XL30 type instrument.

3. Results and discussion

The X-ray diffraction patterns of three selected samples: A2, A3 and A4 are shown in Fig. 1. Films A3 and A4 were fabricated at higher temperatures (303 and 313 K) and higher current densities (3 and 4 A/dm^2), while film A2 was deposited at 293 K and 2 A/dm^2 . The sharp diffraction peaks can be identified as originating from the Al substrate. The diffraction patterns of deposited Al_2O_3 consist of very broad peaks, typical of amorphous materials. The peaks, observed at about 10° for films A3 and A4, are sharper than those in the range of 12 – 24° , but more spread than the crystalline Al peaks. No such peak is observed in the A2 sample. This suggests that a fine-

grained crystalline phase is formed at higher temperatures and higher current densities. The occurrence of different crystalline aluminium oxide phases in alumina films obtained by anodizing has been previously reported [10]. The positions of the first diffraction peaks revealed for films A3 and A4 are close to that reported in the ASTM 31-0026 card for a disperse alumina gel. No additional information about this structure is reported in the ASTM data base. To learn more about the local structure of Al_2O_3 films obtained by anodizing, more detailed wide-angle X-ray scattering studies on free-standing samples are necessary.

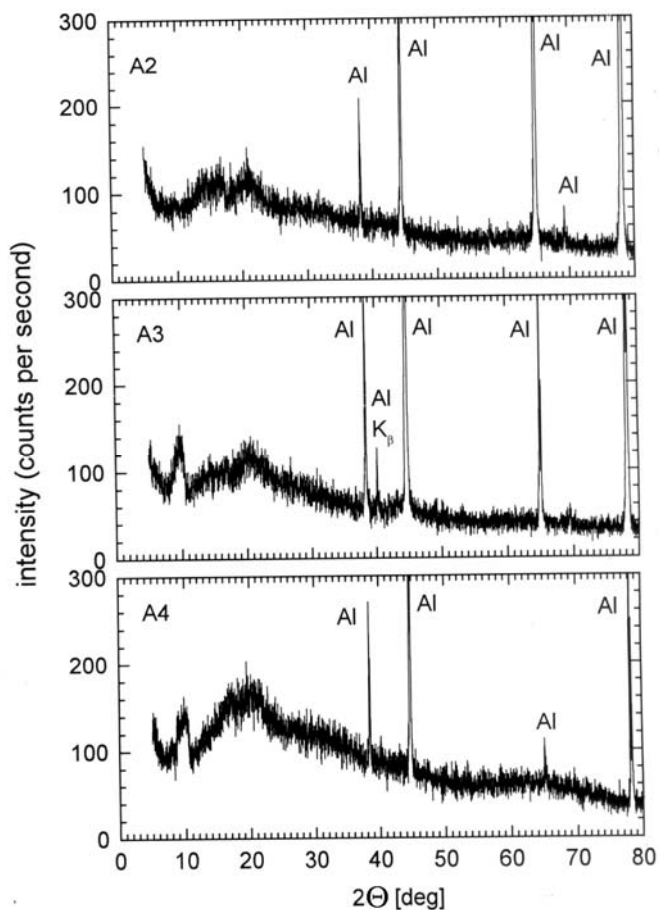


Fig. 1. X-ray diffraction patterns of the A2, A3 and A4 alumina films

Figures 2–6 show contact mode AFM error signal (a) and 3D topographic images of ($5000 \times 5000 \text{ nm}^2$ area) b) obtained for the alumina films surface. The error signal images, although containing no true height information, can give an additional, complementary information about film surface appearance and may resemble the micrographs observed in SEM or TEM images of replicated sample surfaces.

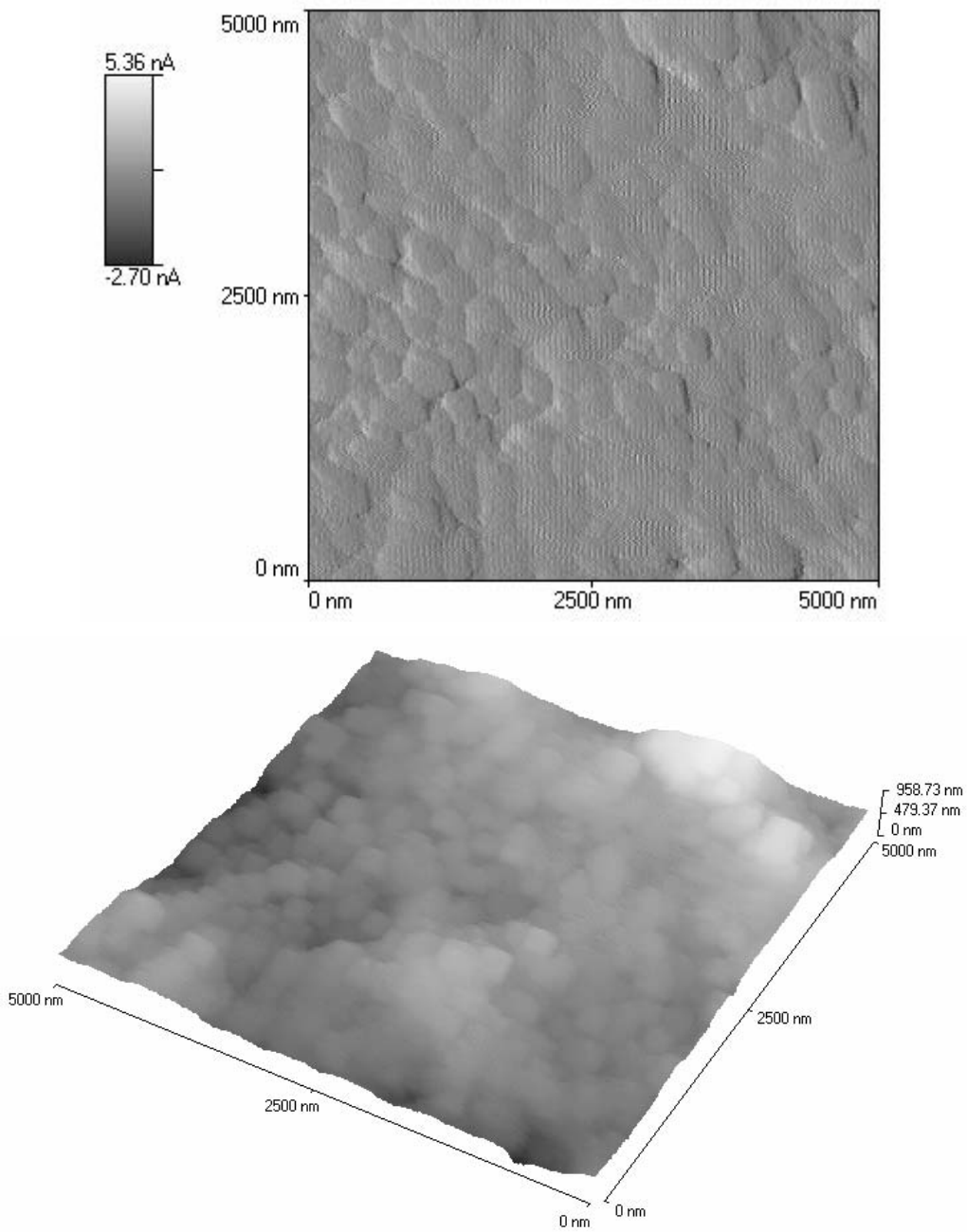


Fig. 2. Simultaneously acquired AFM contact mode: a) error signal, b) 3D-topography images of the A2 alumina film obtained at anodizing temperature $T = 293$ K, anodizing current density $I = 2$ A/dm², and anodizing time $t = 60$ min

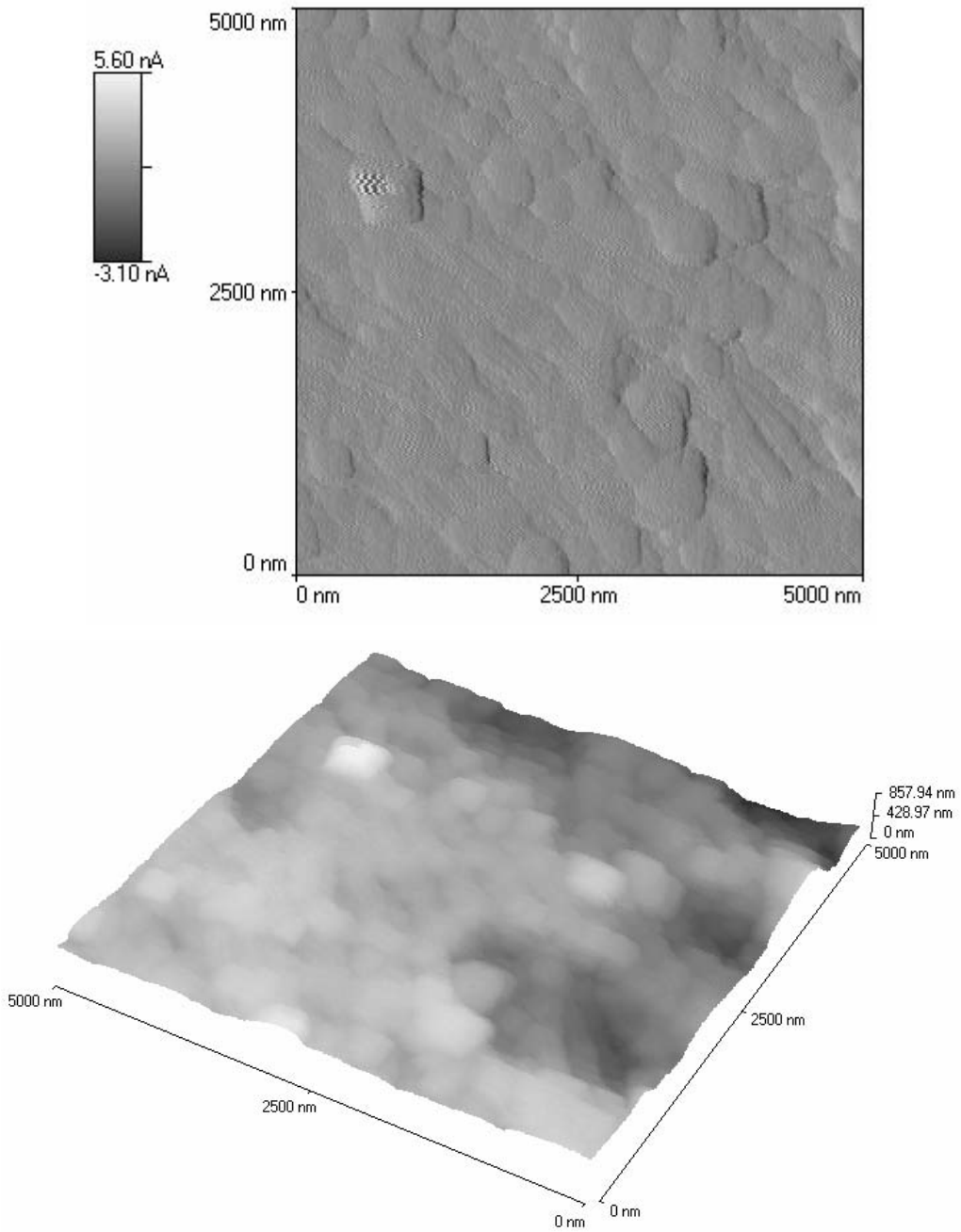


Fig. 3. Simultaneously acquired AFM contact: a) error signal, b) 3D-topography images of the A23 alumina film obtained at anodizing temperature $T = 293$ K, anodizing current density $I = 3$ A/dm², and anodizing time $t = 40$ min

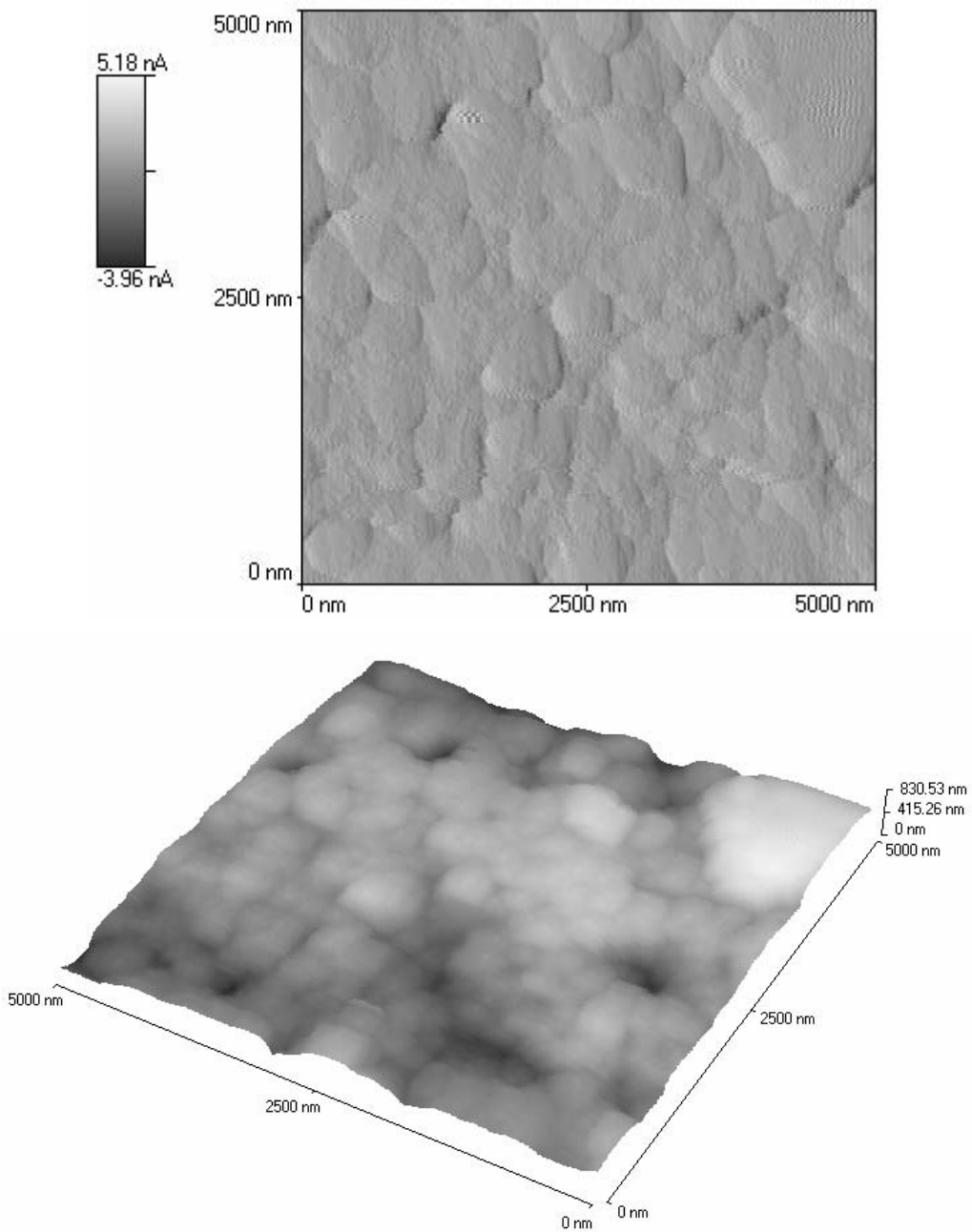


Fig. 4. Simultaneously acquired AFM contact mode (a) error signal, b) 3D-topography images of the A32 alumina film obtained at anodizing temperature $T = 303$ K, anodizing current density $I = 2$ A/dm², and anodizing time $t = 80$ min

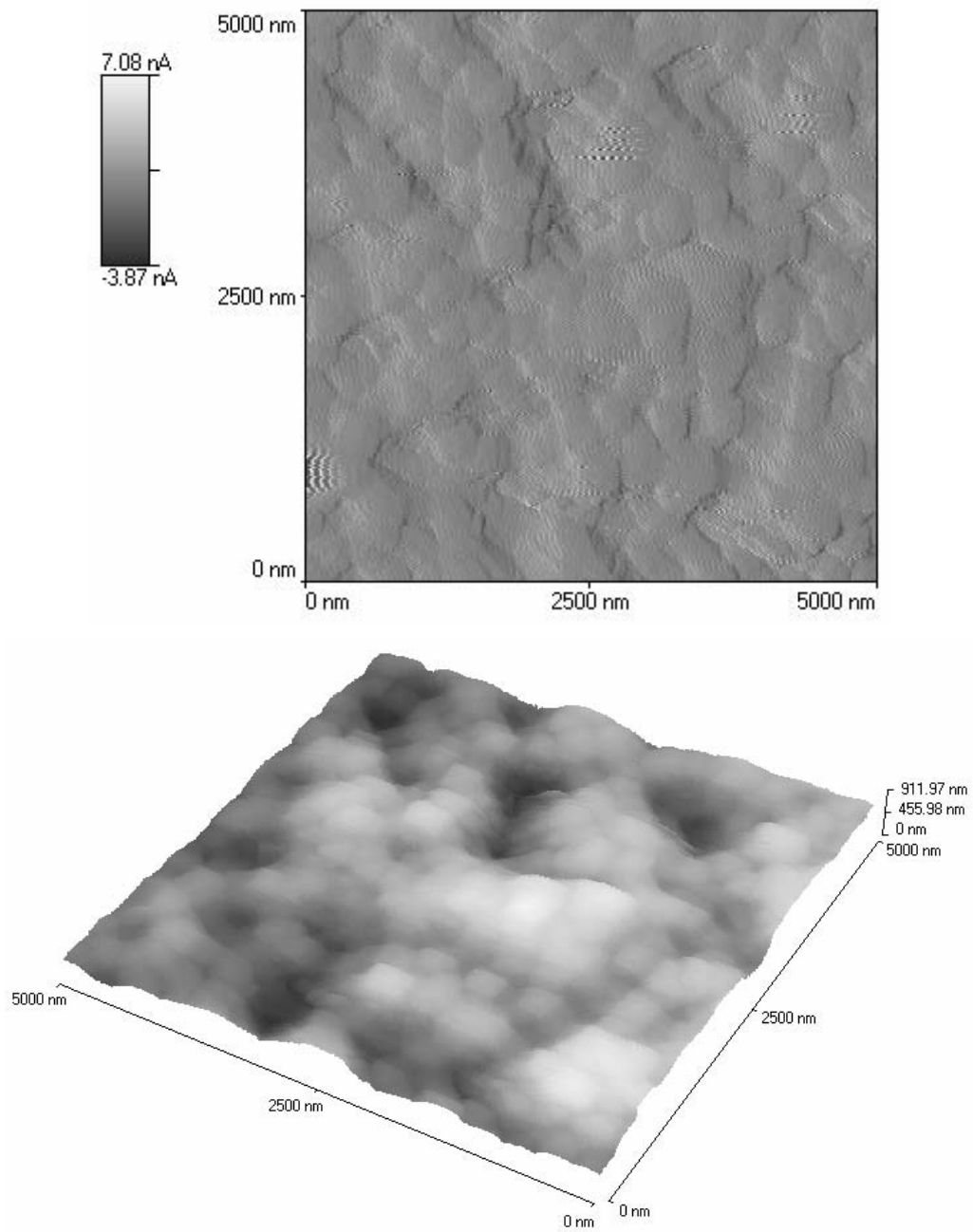


Fig. 5. Simultaneously acquired AFM contact mode (a) error signal, b) 3D-topography images of the A3 alumina film obtained at anodizing temperature $T = 303$ K, anodizing current density $I = 3$ A/dm², and anodizing time $t = 60$ min

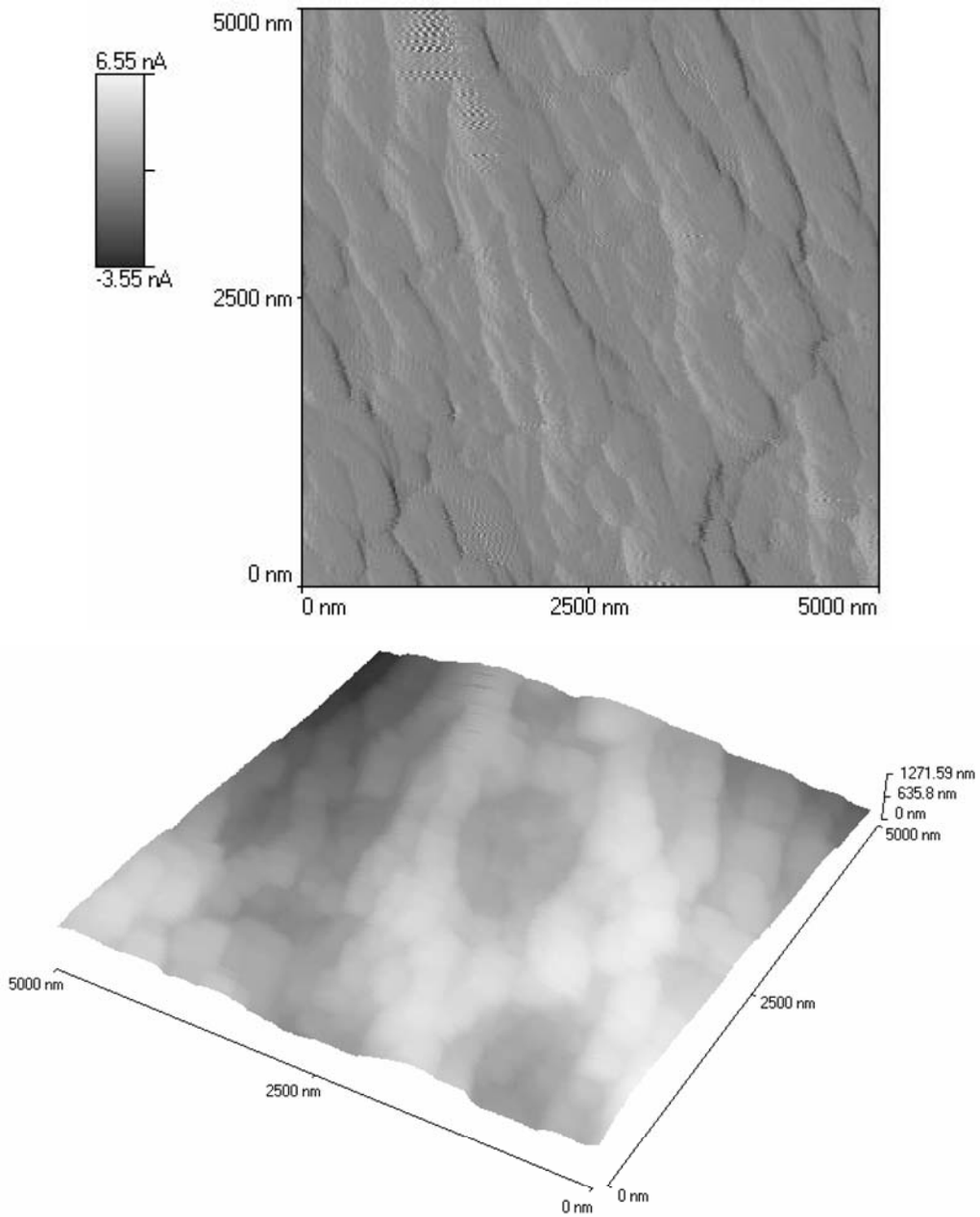


Fig. 6. Simultaneously acquired AFM contact mode (a) error signal, b) 3D-topography images of the A4 alumina film obtained at anodizing temperature $T = 313$ K, anodizing current density $I = 4$ A/dm², and anodizing time $t = 60$ min

Table 1 shows a summary of the parameters of the anodising process and the AFM parameters, characterising the surface roughness for several alumina films and also for the parent Al substrate. Surface roughness has been evaluated from topography images using microscope software. The shape of the tip was not taken into account. Surface roughness parameters, known and commonly used, are the average surface roughness R_a and surface root mean square rms. An additional parameter, however, the relative surface area R_{SA} , defined as the ratio of the surface described in 3-dimensional space by the AFM to the 2-dimensional scan range, can give better insight into surface roughness. AFM results for the films obtained at an electrolyte temperature ~ 293 K are shown in Figs. 2 and 3. These films were prepared at 2 A/dm^2 and 3 A/dm^2 current densities and their thickness were $\sim 25 \text{ }\mu\text{m}$ and $\sim 29 \text{ }\mu\text{m}$, respectively. The images of the alumina films obtained at an electrolyte temperature of 303 K and anodising current densities of 2 A/dm^2 and 3 A/dm^2 are shown in Fig. 4 and 5, respectively.

Table 1. Summary of the anodizing process parameters and AFM results for several alumina films and for the Al substrate¹

Sample	T (K)	I (A/dm ²)	d (μm)	t (min)	R_{SA}	rms (nm)	R_a (nm)
A2	293	2	25	60	1.296	190.52	144.74
A23	293	3	29	40	1.251	174.37	142.45
A32	303	2	33	80	1.331	293.20	197.12
A3	303	3	44	60	1.428	233.71	178.91
A4	313	4	67	60	1.765	480.52	390.43
Al					1.434	658.42	555.44

¹ T – anodizing electrolyte temperature, I – anodizing current density, d – obtained alumina film thickness, t – anodizing time, R_{SA} – relative surface area, rms – surface root-mean-square, R_a – average surface roughness (roughness parameters – without any flattening).

Presented in Figure 6 is the AFM surface topography of the alumina film prepared at the current density of 4 A/dm^2 and at the highest temperature in these experiments, 313 K. It differs considerably from the remaining samples. The line scans across of the AFM topography images for the alumina film and the initial Al substrate are shown in Figures. 7 and 8.

Film thickness increases when both the anodizing current density and temperature are raised. The results presented in AFM images clearly show that alumina films prepared at 293 K and 303 K reveal quite different surface topographies. The surface topographies of the films shown in Figs. 2 and 3, obtained at 293 K, exhibit not very flat and uniform surfaces with many holes (depressions), ranging from one to several columns in diameter. On the other hand, the surface of the films prepared at 303 K (Figs. 4 and 5) are more uniform, with the diameter of holes (or pores) of the order of one column (or smaller). The columnar sizes are estimated to be in the range $0.4\text{--}1 \text{ }\mu\text{m}$ and were more nonuniform in the films obtained at 293 K.

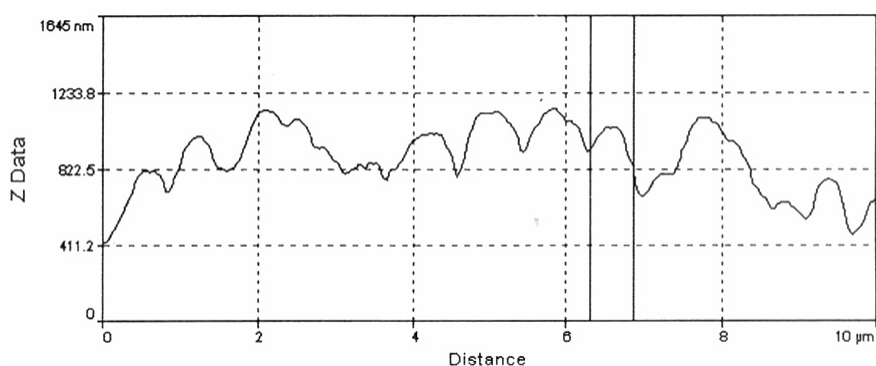


Fig. 7. Line scan across the AFM topography image for the A4 alumina film

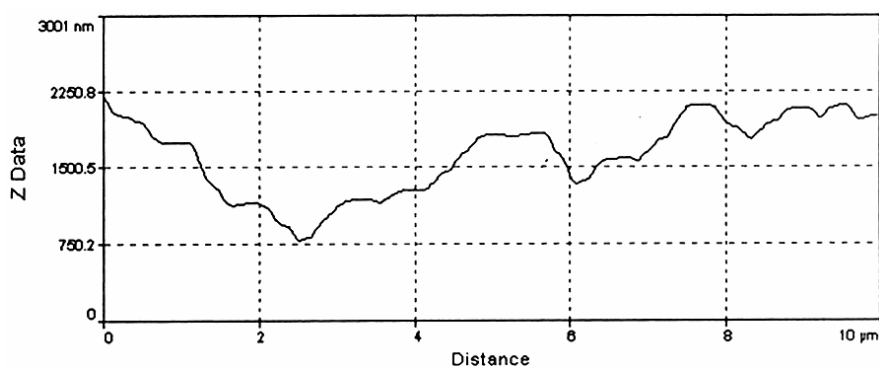


Fig. 8. Line scan across the AFM topography image for the Al substrate

The first results show that the experimental conditions (temperature and current density) are crucial for the final state of the fabricated coatings and especially for the aluminium substrate surface preparation. Prior to anodising, it is essential to clean the surface of dirt, grease oil and, in particular, any skin formed during rolling, drawing or pressing. Anodizing seems to be the growth process which itself can strongly affect the initial roughness of the substrate due to the chemical action of the electrolyte. From AFM images shown in the present paper, one can conclude that the large initial roughness of the aluminium substrates has been slightly cured during the growth of the alumina films in the anodizing process. In all cases, the topography of the alumina films resembles the rough topography of the initial Al substrate, although the roughness parameters, e.g. R_{SA} , for films prepared at 293 K and 303 K are lower than the roughness parameters for the initial Al surface. For films obtained at 303 K, however, these parameters are closer to R_{SA} and for film anodized at 313 K they exceed it.

The anodized alumina thin films exhibit a very distinct columnar growth structure, as can be shown in the SEM images of the film cross-sections. Examples of SEM images of the alumina film cross-sections are shown in Fig. 9, for the A2, A3 and A4 samples, where the columnar growth structure is clearly visible.

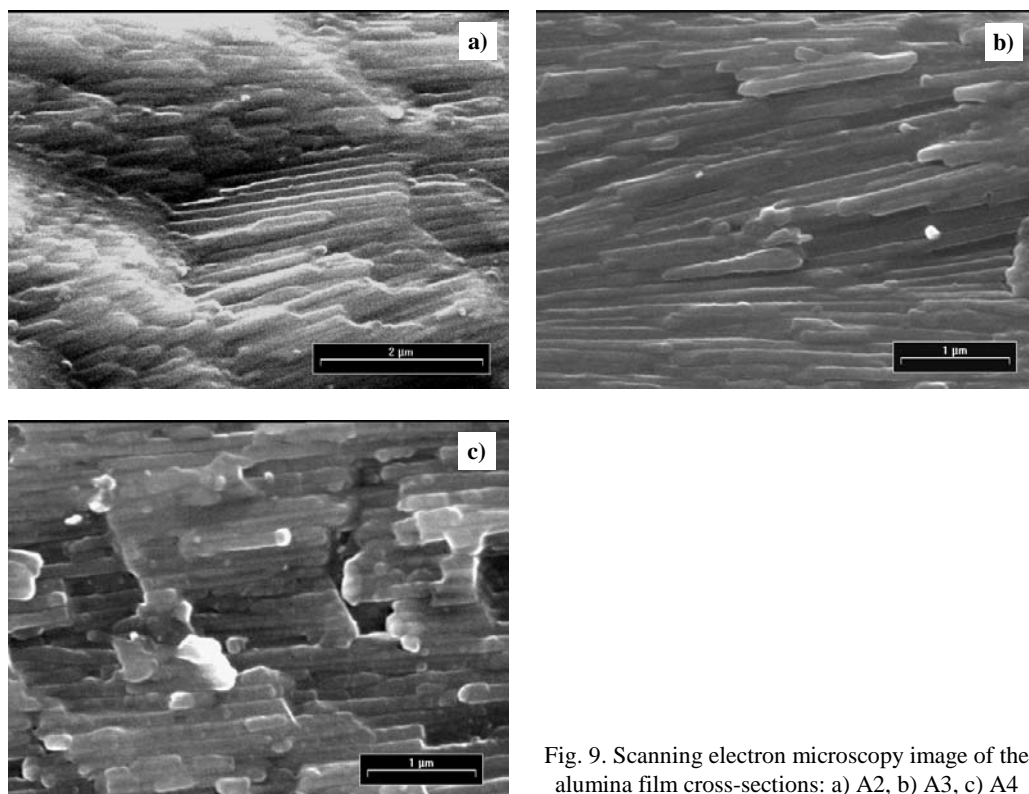


Fig. 9. Scanning electron microscopy image of the alumina film cross-sections: a) A2, b) A3, c) A4

This columnar structure can also be revealed on the alumina film surface as the dome-shaped ends of the columns projecting over the surface and can be imaged by AFM. The presented images show that the AFM technique is a very useful tool for studying thin film morphology, providing information that is equivalent to that obtained by SEM. However, as can be seen in the AFM topography images, especially for the films shown in Figs. 2 and 3, the observed columnar structure may be dominated by the large film surface irregularities mentioned above. Surface topography resembles some initial Al surfaces and the surface roughness R_{SA} is larger than that of the initial Al substrate. It was observed that error signal imaging can give more details and the surface structure can be seen in areas that appear to be deep dark valleys in the topographic images. In general, alumina film surface topography and roughness can be attributed to the internal film growth structure, initial aluminium substrate irregularities, and to the specific anodizing process itself.

It is known that data obtained directly from AFM images overestimates lateral dimensions, because the obtained image is a combination of the tip and sample interactions. The tip broadening effect, even if it is not immediately obvious in images, is present in all AFM images. If the probe tip is larger than the surface features, then surface roughness measurements will appear smaller than they should be. In this pa-

per, however, the obtained images are acceptable. They contain most of the features of the alumina films surface structure confirmed by the SEM.

The structure of Al_2O_3 oxide layers deposited on aluminium alloys stimulates the application of these layers in machine construction. Special properties of the deposited oxide coatings (e.g., morphology and an increase of the surface area due to micro- and macropores) give a wear and tear resistance guarantee for the upper layer and indicate their preferential use in sliding matchings. The main application of such an oxide layer is cylinder bearing surfaces in non-lubricated air-compressors. In this case, the oxide layer matches with rings made of a material containing polytetrafluoroethylene (PTFE), with a graphite filler in the amount of 15wt. % (TG15-type material). In the period of sliding mating of the oxide layer and TG15-type material the sliding film appears on a surface of the oxide layer in consequence of a frictional transfer of material. The creation of such a sliding film provides very good conditions for the mating of such a matching (friction coefficient $\mu = 0.08$).

The influence of the anodizing process parameters for the application of such an oxide layer in cylinder bearing surfaces in non-lubricated air-compressors was presented in [1] and [9].

4. Conclusions

A method of hard anodic treatment at elevated temperatures has been developed, which does not require an additional cooling. The heat produced during treatment is used to control oxide coating properties. The AFM contact technique was used to study the morphology and roughness of the alumina coating films produced by electrolytic deposition. An X-ray diffraction test has shown that the prepared films are generally amorphous. A small precipitation of a fine-grained crystalline phase, similar to the dispersive alumina gel, has been observed for films obtained at higher temperatures and higher current densities.

Columnar growth of the films has been revealed by the AFM technique and supported by SEM. Differences in surface roughness and in the size and shape of the columns have been clearly observed in the AFM error signal and 3-dimensional topography images. Those differences can be related to the parameters of the anodizing process. Oxide coatings appropriate for application were obtained under carefully selected deposition conditions, which ahead preparation of the films special properties of the deposited oxide coatings (like e.g. structure, with the large surface area due to the micro- and macropores created during the electrolytic process. The following parameters have proved to be optimal for the production of alumina coatings: a current density of 3 A/dm^2 and temperature of 303 K. An increase of the rate of deposition of oxide coating can be achieved by raising the current density to 4 A/dm^2 , but then the temperature should also be raised to 313 K [1, 9].

The properties of the films obtained in this way, such as structure, morphology, and an increase in surface area due to the presence of micro- and macropores on the surface during cooperation, are suitable for the creation of sliding plastic films with TG15 protecting oxide coatings from wear. Films of increased porosity are of great interest from the point of view of their potential applications as sliding joints.

Acknowledgements

The authors thank Dr. Joanna Kapusta (Department of Solid State Physics, University of Silesia) for performing the X-ray diffraction measurements and for her help in the use of the ASTM data base.

References

- [1] SKONECZNY W., TOKARZ A., *Wear*, 169 (1993), 209.
- [2] VANFLETEREN J., VAN CALSTER A., *Thin Solid Films*, 139 (1986), 89.
- [3] BUNSHAH R.F., SCHRAMM R.J., *Thin Solid Films*, 40 (1977), 211.
- [4] VUORISTO P., MANTYLA T., KETTUNEN P., *Thin Solid Films*, 204 (1991), 297.
- [5] OTT A.W., KLAUS J.W., JOHNSON J.M., GEORGE S.M., *Thin Solid Films*, 292 (1997), 135.
- [6] STARK I., STORDEUR M., SYROWATKA F., *Thin Solid Films*, 266 (1993), 185.
- [7] PATEL R.D., TAKWALE M.G., NAGAR V.K., BHIDE V.G., *Thin Solid Films*, 115 (1984), 169.
- [8] THORNTON J.A., *Annu. Rev. Mater. Sci.*, 7 (1977), 239.
- [9] SKONECZNY W., KACAŁA Z., *Exploitation Problems of Machines*, 3 (1994), 443.
- [10] ROSENBLUM B., *Tribo-Stimulated Emission From Oxide Covered Metal Surfaces*, University Microfilms International, Ann Arbor, MI, USA, 1976.

Received 15 July 2004

Revised 2 August 2004